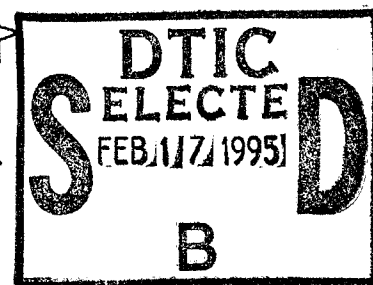


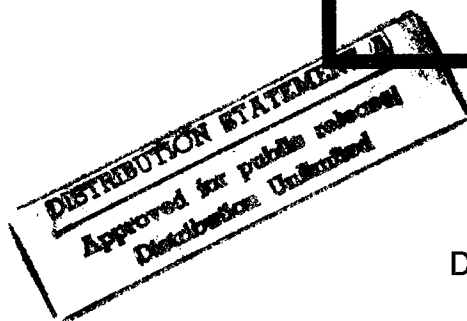
REPORT DOCUMENTATION PAGE			Form Approved OMB No. 0704-0188	
Public reporting burden for this collection of information is estimated to average 1 hour per response, including the time for reviewing instructions, searching existing data sources, gathering and maintaining the data needed, and completing and reviewing the collection of information. Send comments regarding this burden estimate or any other aspect of this collection of information, including suggestions for reducing this burden, to Washington Headquarters Services, Directorate for Information Operations and Reports, 1215 Jefferson Davis Highway, Suite 1204 Arlington, VA 22202-4302, and to the Office of Management and Budget, Paperwork Reduction Project (0704-0188), Washington, DC 20503.				
1. AGENCY USE ONLY (Leave blank)		2. REPORT DATE		3. REPORT TYPE AND DATES COVERED
4. TITLE AND SUBTITLE AN EXPERIMENTAL STUDY OF PLANAR HETEROGENEOUS SUPERSONIC CONFINED JETS				5. FUNDING NUMBERS
6. AUTHOR(S) Frederick J. Tanis Jr. Ph.D., Captain, USAFR				
7. PERFORMING ORGANIZATION NAME(S) AND ADDRESS(ES) Air Force Institute of Technology School of Engineering 2950 P Street Wright-Patterson AFB OH., 45433-7765				8. PERFORMING ORGANIZATION REPORT NUMBER AFIT/DS/AA/94-6
9. SPONSORING/MONITORING AGENCY NAME(S) AND ADDRESS(ES) Wright Laboratory Aero-Propulsion and Power Directorate (WL/PO) Wright-Patterson AFB OH., 45433-7765 Dr. Edward T. Curran, Sponsor				10. SPONSORING/MONITORING AGENCY REPORT NUMBER
11. SUPPLEMENTARY NOTES Dissertation Adviser: Dr. William C. Elrod, Professor of Aeronautical Engineering				
12a. DISTRIBUTION AVAILABILITY STATEMENT Approved for public release; distribution unlimited			12b. DISTRIBUTION CODE	
13. ABSTRACT (Maximum 200 words) <p>The effects of varying the exit pressure of a supersonic helium jet exhausting coaxially with two parallel supersonic air streams into a constant area duct were investigated. The method used to evaluate the mass entrainment rate was to measure helium molar concentration profiles and mass flux across the duct using a binary gas probe then calculate the mass entrainment into the helium jet. In order to conduct this study a novel binary gas probe was developed which allowed helium concentration and mass flux data to be obtained during continuous traverses across the supersonic flowfield.</p> <p>High exit pressure ratio (EPR) led to improved overall mixing compared to the baseline case with an EPR near unity. The high EPR caused low mass entrainment along the jet shear layers due to high convective Mach numbers and velocity ratios, but the high EPR caused oblique shocks to form which reflected off the duct walls and intersected with the helium jet several times causing significant mass entrainment due to numerous shock-shear layer interactions (SSLIs). A correlation between the vorticity generated during a SSLI and the mass entrainment into the jet was developed.</p>				
14. SUBJECT TERMS Supersonic Mixing, Shock-Shear Layer Interaction, Heterogeneous Jets, Planar Jets, Exit Pressure Ratio, Mass Entrainment Rate, Binary Gas Probe				15. NUMBER OF PAGES 181
				16. PRICE CODE
17. SECURITY CLASSIFICATION OF REPORT UNCLASSIFIED	18. SECURITY CLASSIFICATION OF THIS PAGE UNCLASSIFIED	19. SECURITY CLASSIFICATION OF ABSTRACT UNCLASSIFIED	20. LIMITATION OF ABSTRACT UNLIMITED	



**AN EXPERIMENTAL STUDY OF
PLANAR HETEROGENEOUS
SUPERSONIC CONFINED JETS**

DISSERTATION

**Frederick J. Tanis Jr, B.S., M.S.
Captain, USAFR**



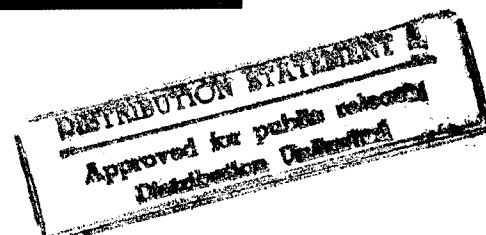
19950206 096

DEPARTMENT OF THE AIR FORCE

AIR UNIVERSITY

AIR FORCE INSTITUTE OF TECHNOLOGY

Wright-Patterson Air Force Base, Ohio



AFIT/DS/AA/94-6

AN EXPERIMENTAL STUDY OF
PLANAR HETEROGENEOUS
SUPERSONIC CONFINED JETS

DISSERTATION

Frederick J. Tanis Jr, B.S., M.S.
Captain, USAFR

Approved for public release; distribution unlimited

100% QUALITY INSPECTED 4

AN EXPERIMENTAL STUDY OF PLANAR HETEROGENEOUS
SUPERSONIC CONFINED JETS

DISSERTATION

Presented to the Faculty of the School of Engineering

of the Air Force Institute of Technology

Air University

In Partial Fulfillment of the

Requirements for the Degree of

Doctor of Philosophy

Frederick J. Tanis Jr, B.S., M.S.

Captain, USAFR

December 1994

Approved for public release; distribution unlimited

Accession For	
NTIS GRA&I	<input checked="checked" type="checkbox"/>
DTIC TAB	<input type="checkbox"/>
Unannounced	<input type="checkbox"/>
Justification	
By	
Distribution/	
Availability Codes	
Dist	Avail and/or Special
A-1	

AN EXPERIMENTAL STUDY OF PLANAR HETEROGENEOUS
SUPERSONIC CONFINED JETS

Frederick J. Tanis Jr., B.S., M.S

Captain, USAFR

Approved:

William C. Elrod 29 Nov 94
William C. Elrod, Chariman

Milton E. Franke 29 Nov 94
Milton E. Franke

William F. Bailey 29 Nov 94
William F. Bailey

Paul I. King 29 Nov 94
Paul I. King, Deans Rep

Accepted:

Robert A. Calico, Jr.
Robert A. Calico, Jr.
Dean, Graduate School of Engineering

Preface

The purpose of this investigation was to investigate the effects of fuel injector exit pressure and the interaction of shocks on fuel-air mixing. The experiments for this study were conducted at the AFIT blowdown gas dynamic facility in the School of Engineering at Wright-Patterson AFB Ohio. The topic of this study was suggested by Dr. Edward T. Curran, Director of the Wright Laboratory's Aero-Propulsion and Power Directorate, Wright-Patterson AFB, who is interested in the application/relation of these effects to supersonic combustion. In addition to suggesting the topic Dr. Curran provided invaluable information that helped shape my research and for that help I am greatly indebted.

I would like to express my sincere thanks to my principal advisor Dr. William C. Elrod for help in setting up the experimental facility and his advice on how to proceed during the course of my study. I would also like to thank Dr. Milton E. Franke and Dr. William F. Bailey, who were on my research committee and provided valuable feedback on my progress.

I also wish to thank the staff at the AFIT machine shop for their expert craftsmanship in constructing the various parts of my experimental facility. Special thanks to John Brohas who performed most of the machine work on the facility. Thanks also to Nick Yardich and his technicians who guided the assembly and calibration of my instrumentation system. I am specially indebted to Mr. Tony Brigalli formerly of the Flight Dynamics Laboratory's Hypersonic Test Facility who taught me the fine art of constructing hot wire sensors.

Finally, the biggest thanks go to my wife Melinda, and children Elizabeth and Erick who provided never ending support and motivation even during the darkest hours of the ordeal.

Frederick J. Tanis Jr.

Table of Contents

Preface	iii
List of Figures	ix
List of Tables	xii
List of Symbols	xiii
Abstract	xvii
I. Introduction	1
I.1. Background	4
I.1.1. Free Jets and Shear Layers	4
I.1.2. Confined Jets and Shear Layers	10
I.1.3. Shock - Shear Layer Interactions	12
I.2. Objective and Scope	13
I.2.1. Objective	13
I.2.2. Scope	14
II. Theory	16
II.1. Exit Pressure Ratio (EPR)	18
II.1.1. Case I: $EPR = 1$	18
II.1.2. Case II: $EPR < 1$	20
II.1.3. Case III: $EPR > 1$	23
II.2. Shock - Shear Layer Interactions	23
II.3. Entrainment and Growth Rates	28
II.3.1. Entrainment Rate	28

II.3.2. Growth Rate	30
II.4. Modeling	31
III. Experimental Apparatus	33
III.1. Blowdown Gasdynamic Facility	33
III.1.1. Air and Vacuum Supply	33
III.1.2. Helium Supply	35
III.1.3. Traversing Mechanism	35
III.1.4. Test Section.....	36
III.2. Instrumentation and Data Acquisition	38
III.2.1. Pressure Measurements.....	39
III.2.2. Data Acquisition System.....	41
III.2.3. Schlieren Camera System.....	42
III.2.4. Test Procedures	42
III.3. Facility Performance	44
IV. Binary Gas Concentration Probe.....	47
IV.1. Background.....	47
IV.2. Theory	49
IV.3. Probe Design.....	52
IV.4. Calibration of Concentration Probe.....	55
IV.5. Data Reduction	59
V. Flowfield Results.....	62
V.1. Mixing Duct Flowfield	62

V.1.1. Exit Pressure Ratio 0.89.....	63
V.1.2. Exit Pressure Ratio 1.49.....	69
V.1.3. Exit Pressure Ratio 3.50.....	79
V.2. Centerline Decay.....	93
V.3. Jet Growth Rates.....	99
V.4. Summary	104
VI. Mass Entrainment Results	106
VI.1. Calculations of Mass Flux and Mass Entrainment Data	106
VI.2. Mass Entrainment.....	110
VI.2.1. Mass Entrainment Rates for EPR 0.89	116
VI.2.2. Mass Entrainment Rates for EPR 1.49	117
VI.2.3. Mass Entrainment Rates for EPR 3.50	118
VI.3. Shock-Shear Layer Interactions.....	120
VI.4. Mixing Enhancement Due to Instability Modes.....	127
VI.5. Mixing Enhancement Due to Exit Pressure Ratio (EPR)	127
VI.6. Summary.....	128
VII. Proposed Model.....	131
VII.1. Basic Model.....	131
VII.2. Application of Model to EPR 3.50	136
VII.3. Additional Applications of Model.....	140
VIII. Conclusions and Recommendations	142
VIII.1. Conclusions	142

VIII.2. Recommendations.....	144
Bibliography.....	147
Appendix A: Transport Properties of a Gas Mixture	153
Appendix B: Calculation of Theoretical Turning and Shock Angles	155
Appendix C: Method Used to Determine Relative SSLI Vorticity	158
VITA.....	162

List of Figures

Figure I-1: Applications of supersonic mixing	2
Figure I-2: Schematic of confined and free jets	5
Figure I-3: Transformation to convective reference frame	8
Figure II-1: Experimental flow model	17
Figure II-2: Case I Theoretical Model.....	19
Figure II-3: Case II Theoretical Model	21
Figure II-4: Case III Theoretical Model	24
Figure II-5: Shock-shear layer interaction model.....	26
Figure III-1: Schematic of AFIT blowdown facility.....	34
Figure III-2: Test section layout	37
Figure III-3: Location of side wall static pressure ports	40
Figure III-4: Schematic of schlieren system.....	43
Figure III-5: Shocks within air nozzles	46
Figure IV-1: Schematic of concentration probe.....	53
Figure IV-2: Example concentration probe calibration curve.....	58
Figure IV-3: Repeatability of concentration probe	60
Figure V-1: Schlieren photographs of $EPR\ 0.89$	64
Figure V-2: Large structures within shear layer.....	66
Figure V-3: Concentration plots for $EPR\ 0.89$	67
Figure V-4: Side wall static pressure for $EPR\ 0.89$	70
Figure V-5: Schlieren photographs of $EPR\ 1.49$	71

Figure V-6: Concentration plots for EPR 1.49	72
Figure V-7: EPR 1.49 shear layer and shock angles	73
Figure V-8: Side wall static pressure for EPR 1.49	75
Figure V-9: Schlieren photographs of EPR 3.50	81
Figure V-10: EPR 3.50 shear layer and shock angles	82
Figure V-11: Concentration plots for EPR 3.50	83
Figure V-12: Simple wave model of EPR 3.50.....	85
Figure V-13: Side wall static pressure for EPR 3.50	87
Figure V-14: Jet centerline helium mass fraction versus X/H	94
Figure V-15: Mass concentration parameter versus X/H	96
Figure V-16: Mass concentration parameter versus X/L_{pc}	98
Figure V-17: Potential core length versus EPR.....	100
Figure V-18: Jet width versus X/H	101
Figure V-19: Density ratio versus X/H	103
Figure VI-1: Ratio of integrated to injected helium mass versus X/H	109
Figure VI-2: Mass flow within jet versus X/H , all EPRs.....	111
Figure VI-3: Mass flow within jet versus X/H for EPR 0.89	112
Figure VI-4: Mass flow within jet versus X/H for EPR 1.49	113
Figure VI-5: Mass flow within jet versus X/H for EPR 3.50	114
Figure VI-6: $(C_1)_{SSLI}$ versus vorticity generated by SSLI.....	123
Figure VI-7: Entrainment rate error Vs. vorticity.....	126
Figure VI-8: Duct mixing ratio versus X/H	129

Figure VII-1: Inviscid flowfield analysis of EPR 3.50..... 137

Figure VII-2: Mass flow within jet; model versus experiment..... 139

Figure VII-3: Applications of enhanced mixing due to SSLIs..... 141

Figure B-1: Flow turning angle definitions 156

Figure C-1: Method of determining angle between density and pressure gradients..... 159

List of Tables

Table I-1: Test Conditions	14, 63
Table V-1: Fully Mixed concentrations	95
Table V-2: Center line decay rate exponents	97
Table VI-1: Entrainment Rates for EPR 1.49	117
Table VI-2: Entrainment Rates for EPR 3.50	119
Table VI-3: Entrainment rates for SSLIs	121
Table VI-4: Entrainment rate errors for EPR 3.50	125

List of Symbols

SYMBOL	NAME	UNITS
ABBREVIATIONS		
ABM	Antiballistic Missile	N/A
A/D	Analog to Digital	N/A
AFIT	Air Force Institute of Technology	N/A
ASAT	Antisatellite	N/A
NASP	National Aerospace Plane	N/A
ND	Non-Dimensional	N/A
PC	Personal Computer	N/A
P-M	Prandtl-Meyer	N/A
SCRAMJET	Supersonic Combustion Ramjet	N/A
SSL	Shock Shear Layer	N/A
SSLI	Shock Shear Layer Interaction	N/A
ROMAN SYMBOLS		
a	Speed of Sound	ft/s
A^*	Area where $M=1$ in a Nozzle (Throat Area)	ft ²
A_{hw}	Cross sectional area at location of the hot wire sensor.	ft ²
A_{ref}	Reference Area (Eq. IV-8)	ft ²
C_1	Proportional constant used by Schetz	ND
\bar{C}	Helium concentration parameter	ND
C_{FM}	Fully mixed concentration of helium	ND
C_p	Specific heat at constant pressure	$\frac{\text{ft} - \text{lbf}}{\text{lbm} - ^\circ\text{R}}$
C_v	Specific heat at constant volume	$\frac{\text{ft} - \text{lbf}}{\text{lbm} - ^\circ\text{R}}$

D_{in}	Inlet diameter of the concentration probe	in
D_o	Outside diameter of the concentration probe	in
D^*	Diameter of sonic orifice within the concentration probe	in
d_w	Diameter of hot wire sensor	in
EPR	Exit pressure Ratio	ND
ER	Entrainment Ratio	ND
H	Jet exit height	in
h	Convective heat transfer coefficient	$\frac{\text{lbf}}{\text{s} \cdot \text{ft} \cdot ^\circ\text{R}}$
k	Thermal conductivity	$\frac{\text{lbf}}{\text{s} \cdot ^\circ\text{R}}$
L_{PC}	Length of helium potential core	in
M	Mach Number	ND
m	Molecular Weight	$\frac{\text{lbm}}{\text{lbmole}}$
\dot{m}	Mass flow rate	$\frac{\text{lbm}}{\text{s}}$
M^+	Bogdonoff's Characteristic Mach number (Eq. I-3)	ND
M_{ch}	Characteristic Mach number	ND
nr, np	Exponents for Reynolds and Prandtl numbers (Eq. IV-7)	ND
Nu	Nusselt number	ND
P	Static pressure	$\frac{\text{lbf}}{\text{in}^2}$
P_0	Total pressure	$\frac{\text{lbf}}{\text{in}^2}$
Pr	Prandtl number	ND
\dot{Q}	Heat transfer rate	$\frac{\text{lbf} \cdot \text{ft}}{\text{s}}$
$Q(X)$	Total mass within the jet	lbm

Q_0	Initial mass within the jet	lbm
\hat{R}	Universal gas constant	$\frac{\text{ft} - \text{lbf}}{\text{lbmole} - ^\circ\text{R}}$
R_m	Gas constant of helium and air mixture	$\frac{\text{ft} - \text{lbf}}{\text{lbm} - ^\circ\text{R}}$
r	Velocity ratio U_1/U_2	ND
R_w, R_b	Electrical resistance: hot wire sensor, bridge	ohms
s	Density ratio ρ_2/ρ_1	ND
t	Time	s
T_f	Film temperature	$^\circ\text{F}$
T_0	Total temperature	$^\circ\text{F}$
U	Velocity	ft/s
V_w	Voltage across hot wire bridge	V
X	Axial distance	in
X_{He}	Molar fraction of helium	ND
Y	Height (perpendicular distance)	in

GREEK SYMBOLS

δ	Shear layer thickness	in
δ	Shock thickness in Appendix C	in
∇P	Pressure gradient	$\frac{\text{lbf/in}^2}{\text{in}}$
$\nabla \rho$	Density gradient	$\frac{\text{lbm/ft}^3}{\text{in}}$
ϵ	Empirical constant (Eq. II-3)	ND
γ	Ratio of specific heats	ND

λ	Momentum ratio $(\rho V)_{\text{He}}/(\rho V)_{\text{air}}$	ND
ρ	Density	lbm/ft ³
μ	Viscosity	$\frac{\text{lb-f-s}}{\text{ft}^2}$
ζ	Vorticity	1/s ²

SUPERSCRIPTS

*	Based on conditions at mach one
---	---------------------------------

SUBSCRIPTS

1	Relates to the high speed stream
1-C	Relates to the difference in velocity between the high speed stream and the convective velocity
2	Relates to the low speed stream
A	Relates to the air stream
C	Relates to the convective speed of the large structures within the shear layer or jet.
C-2	Relates to the difference in velocity between the low speed stream and the convective velocity
H	Relates to the helium stream
J	Relates to the helium jet
m	Pertaining to the gas mixture of helium and air
mass	Based on mass fraction
x	Conditions upstream of a shock

Abstract

The effects of varying the exit pressure of a supersonic helium jet exhausting coaxially with two parallel supersonic air streams into a constant area duct were investigated. A relationship for the effect the exit pressure ratio between the helium jet and the air streams had on the mass entrainment rate of air into the helium jet was established. The method used to evaluate the mass entrainment rate was to measure helium molar concentration profiles across the duct using a binary gas probe then calculate the mass entrainment into the helium jet.

High EPR led to improved overall mixing compared to the baseline case with an EPR near unity. The high EPR caused low mass entrainment along the jet shear layers due to high convective Mach numbers and velocity ratios, but the high EPR also caused oblique shocks to form which reflected off the duct walls and intersected with the jet several times causing significant mass entrainment due to numerous SSLIs. The end result was a higher percentage of the available air mixing with the helium for the geometry tested.

During this investigation two new parameters were developed to analyze confined jets. The first parameter was developed to correlate centerline jet decay rates of confined jets and free jets allowing free jet data to be applied to confined jets. The second parameter developed in this study is the duct mixing ratio (DMR) which was developed to quantify the degree of mass entrainment within a confined duct. Plotting the DMR for the

three cases tested indicated that high exit pressure ratios led to a more fully mixed concentration as compared to low exit pressure ratios.

In order to conduct this study a novel binary gas probe was developed which allowed concentration data to be obtained during continuous traverses across the supersonic flowfield. Unlike previous probes which required a known total pressure and/or temperature profile this probe did not require any prior knowledge of the flowfield. The probe also is capable of measuring mass fluxes across the flowfield which permits determination of mass entrainment rates into the helium jet.

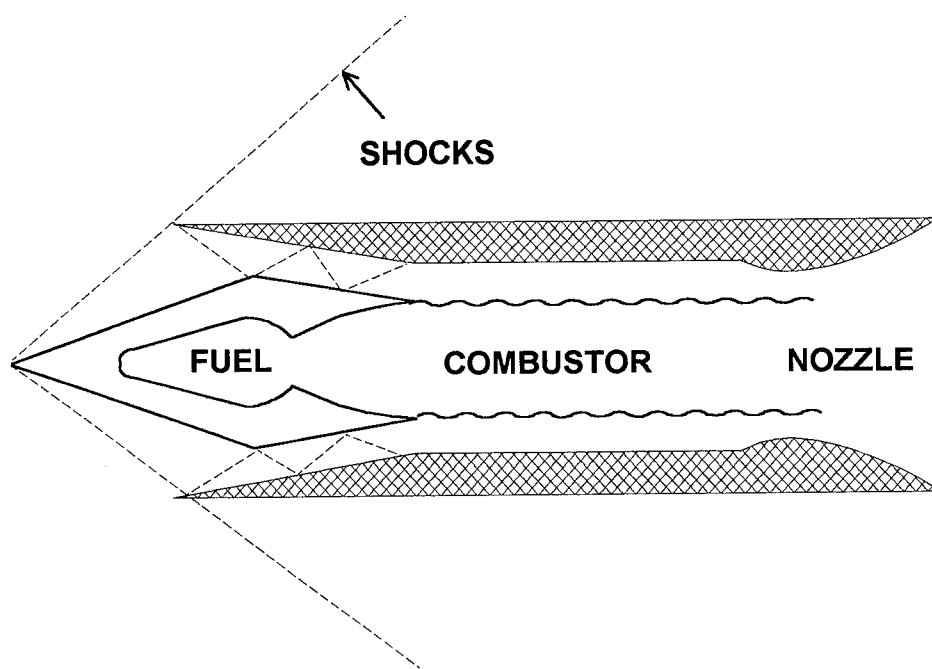
AN EXPERIMENTAL STUDY OF PLANAR HETEROGENEOUS SUPERSONIC CONFINED JETS

I. Introduction

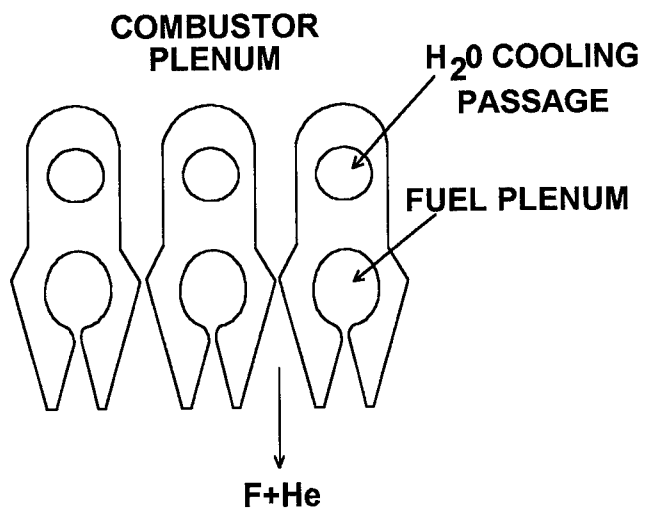
Information on the mixing of confined parallel supersonic gas jets is required for the design of supersonic combustion ramjet (SCRAMJET) engines for hypersonic flight vehicles, as well as for the design of chemical lasers. SCRAMJET and chemical laser developments are being actively pursued in the United States and overseas today. The U.S. has the National Aerospace Plane (NASP) under development which specifies a SCRAMJET for its primary propulsion system, because of the SCRAMJET's high efficiency as compared to ramjets and chemical rockets for atmospheric flight speeds between Mach 5 and 20 (1:1, 2:3, 3:3, 4:3)¹. The chemical laser is being considered for integration into an aircraft for use in destroying short range ballistic missiles as part of the Ballistic Missile Defense Initiative.

The supersonic turbulent mixing of gases in the SCRAMJET takes place within the combustor between the hydrogen fuel and the air, that has been decelerated from hypersonic flight speed to moderate supersonic/ hypersonic speeds (Mach 3-6) by a series of oblique shocks in the engine's inlet. Fuel is injected into the supersonic air stream where it mixes and reacts with the air before being accelerated through the exit nozzle (Fig. I-1a). The fuel must be mixed with the air very quickly, with a minimum of total

¹Numbers in parenthesis indicate reference from the bibliography. The particular page numbers being referenced are after the colon. If there are no page numbers cited then the entire document is referenced.



a) Supersonic combustion ramjets



b) Supersonic chemical lasers

Figure I-1: Applications of supersonic mixing

pressure loss, in order to keep the combustor length short and the overall efficiency high (5:1-2, 6:6, 7:50, 8:33). Axial injection provides low total pressure losses as well as contributing to the thrust of the engine but fails to achieve optimum mixing in a reasonable distance because the cross-stream diffusion velocity is low compared to the supersonic axial flow velocity (1:12, 8:35, 9:12). In cross stream injection the mixing is very good but the jets cause normal and curved shocks to form at the injection location which results in high total pressure losses. Normal injection also does not contribute to the thrust of the engine .

In the chemical laser the reactants are injected alternately through supersonic nozzles (Fig. I-1b). The reactants must mix and react at supersonic velocities within the optical cavity to bring about lasing (10:276-295). In the chemical laser the mixing must be accomplished in such a way that the turbulence levels are uniform across the optical cavity in order to minimize changes in the index of refraction which lead to poor beam quality. In both the SCRAMJET and the chemical laser the mixing must take place in as short a distance as possible with a minimum of total pressure loss in order to maximize the efficiency of the device and minimize the weight and volume which are critical when integrating the engine or the laser into an aircraft design.

A recent review article (11:1-15) has indicated that there is little experimental or theoretical information on the mixing of parallel planar supersonic jets, particularly heterogeneous jets. In addition, very little information exists about both the effects of nonideal expansion of supersonic jets on mixing and the effects of shocks intersecting the jet's shear layers on mixing. The effects of shocks and nonideal expansion on mixing are

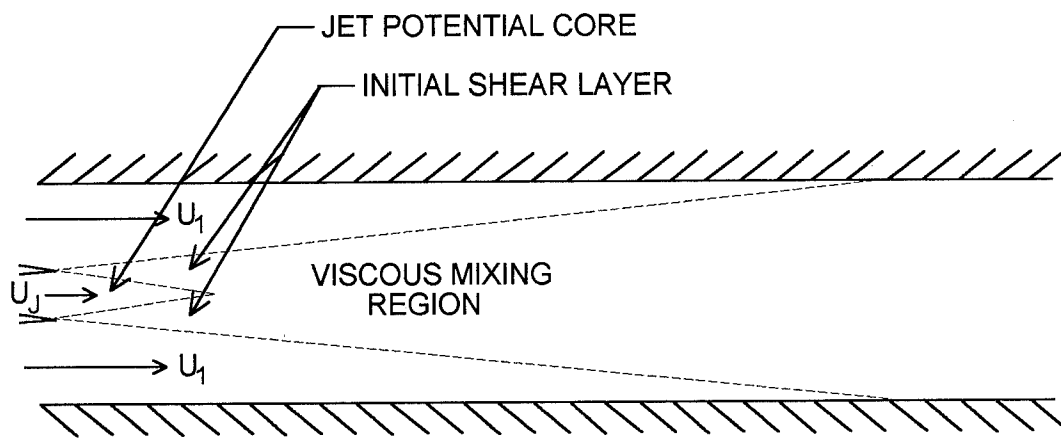
very important because in a SCRAMJET shocks will be present from the inlet operation and the fuel injection process. The fuel injector's exit pressure will not necessarily match the inlet air pressure, especially for a fixed fuel injector geometry (12). The unmatched fuel injector exit pressure, particularly when the fuel is underexpanded, may be desirable because it would destabilize the shear layer between the fuel and air streams thereby enhancing mixing in the combustor. This study investigates the mixing of heterogeneous parallel supersonic jets with emphasis on the effects of mismatched fuel injector exit pressure and shock-shear layer interactions (SSLIs) on entrainment within a confined duct.

I.1. Background

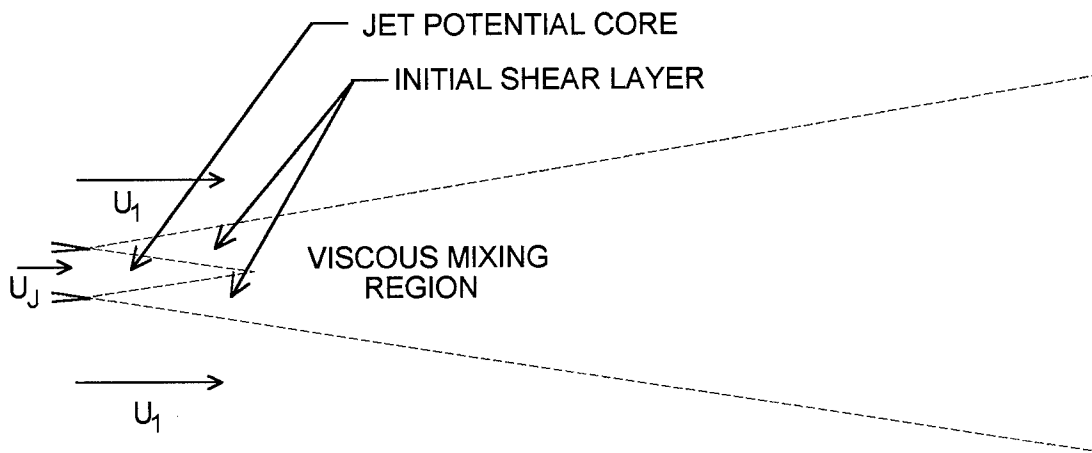
The existing experimental data on parallel supersonic planar jet mixing as it occurs in a SCRAMJET combustor are limited (11:1). Most of the studies on co-flowing supersonic jets are axisymmetric configurations (13, 14, 15) or deal with ejector performance (16, 17) and not with mixing per se. Recently there has been some research on the mixing of planar supersonic jets but it is still limited (18, 19). There is a fair amount of information on the mixing in supersonic shear layers, both homogeneous and heterogeneous, which can be applied to the mixing of supersonic jets (20-32). A review of the literature from three areas pertinent to this investigation, free jets and shear layers, confined jets and shear layers, and shock-shear layer interactions follows.

I.1.1. Free Jets and Shear Layers

The structure of free and confined jets are shown in Figure I-2 where U_1 is the freestream velocity and U_j is the jet velocity. The primary difference between free and



a) Confined jet



b) Free jet

Figure I-2: Schematic of confined and free jets

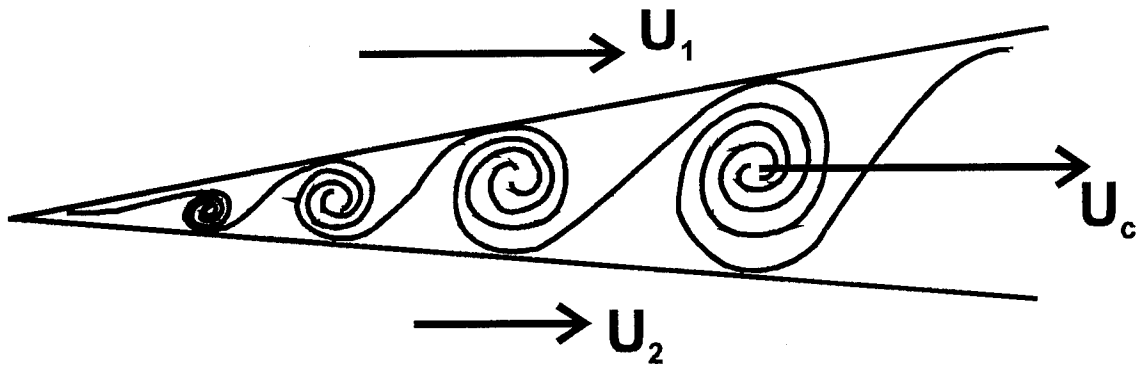
confined jet mixing is that the free jet mixes until the properties of the jet are essentially those of the freestream, whereas the confined jet mixes with the freestream until an equilibrium mixture is reached. The difference is caused by the freestream that bounds the free jet having infinite amount of fluid while the freestream that bounds the confined jet contains a finite amount of fluid. In addition to the difference in mixing, the axial pressure gradient of a free jet is zero while the axial pressure gradient in the confined jet is nonzero due to boundary layer growth on the confining walls. Both the free and confined jets initially form two shear layers at the injection plane. These shear layers entrain fluid from the freestream and widen until they merge on the jet's centerline. The point where the shear layers merge defines the end of the jet's potential core. Since a jet is made up of two shear layers that grow wider as they proceed downstream until they merge, it follows that data and theories from free shear layers could be applied to both free and confined jets.

A 1972 review of shear layer experimental data by Birch and Eggers (20:23,36) indicated that supersonic shear layers grow slower than incompressible shear layers. The data primarily represented single stream shear layers with one side of the shear layer at rest and the other side in a supersonic flow. The data showed that beginning at approximately Mach 1 the shear layer growth rate begins to decrease with increasing Mach number. The growth rate decreases to approximately 1/3 of the subsonic growth rate at Mach 2 (20:36). Birch and Eggers also concluded that there was a definite lack of good information on two stream supersonic shear layers. Since 1972 there has been a significant amount of work done on understanding the two stream supersonic shear layer mixing due to the birth of the NASP program (12).

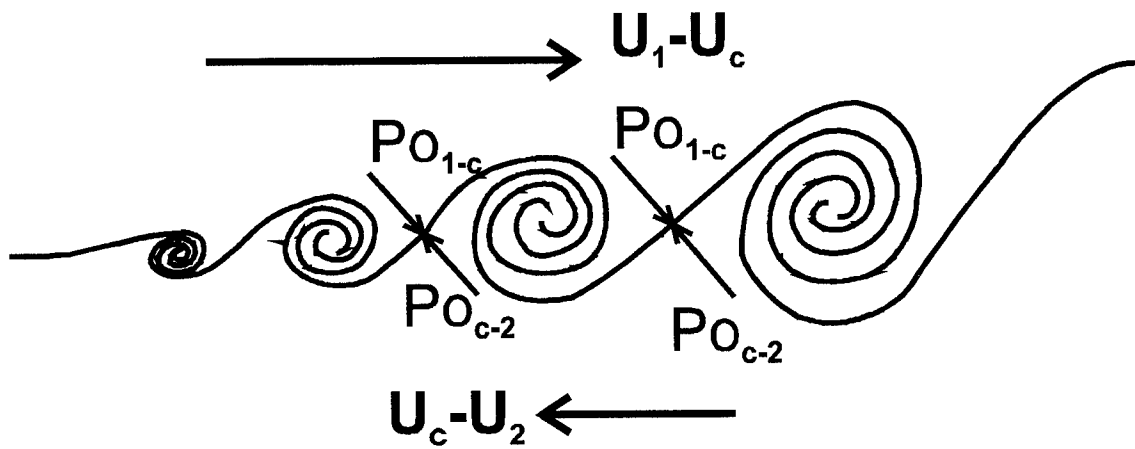
The decrease in growth rate and mixing for compressible shear layers as compared to incompressible shear layers is one of the most significant features of the supersonic shear layer and the feature that limits the usefulness of parallel injection for SCRAMJET combustors. In order to quantify this decrease in mixing several investigators have proposed correlation parameters for compressibility effects. Rudy and Birch (21), Bogdonoff (22) and Chinzei et al. (23) all investigated supersonic air-air shear layers and found that the Mach number of the individual streams was not as important as the relative Mach number between streams and the velocity ratio between the streams. Papamoschou (24) determined the appropriate parameter to use for correlating the compressibility effects of shear layers by performing a linear stability analysis on a compressible vortex sheet. The parameter that he derived has become known as the convective Mach number, M_C . The convective Mach number is based on the difference in velocity between the freestream (U_1, U_2) and the velocity of the large structures (U_C) in the shear layer; the speed of sound (a_1, a_2) being that of either stream (Fig I-3a). This leads to two convective Mach numbers for a single shear layer; one based on the high speed flow (U_1, a_1) and one based on the low speed flow (U_2, a_2). Equation I-1 shows the two convective Mach numbers.

$$M_{C1} = \frac{U_1 - U_C}{a_1} \quad M_{C2} = \frac{U_C - U_2}{a_2} \quad (I-1)$$

The large structures are observed in both supersonic and subsonic shear layers. The convective velocity, U_C , is the velocity of the large structures within the shear layer and is determined by examining the shear layer in a reference frame attached to a large structure within the shear layer. A pressure balance develops on a stagnation point between large



a) Convective velocity of large structures



b) Pressure balance in convective reference frame

Figure I-3: Transformation to convective reference frame

structures within the shear layer, as shown in Figure I-3b. The stagnation pressure balance is calculated in Equation I-2 using isentropic relations assuming that the static pressure in the two streams are equal.

$$\left[1 + \frac{\gamma_1 - 1}{2} \left(\frac{U_1 - U_c}{a_1} \right)^2 \right]^{\frac{\gamma_1}{(\gamma_1 - 1)}} = \left[1 + \frac{\gamma_2 - 1}{2} \left(\frac{U_c - U_2}{a_2} \right)^2 \right]^{\frac{\gamma_2}{(\gamma_2 - 1)}} \quad (\text{I-2})$$

Equation I-2 can be solved for U_c . The convective Mach numbers, M_{C1} and M_{C2} , can then be calculated from Equation I-1. If the streams have equal specific heat ratios ($\gamma_1 = \gamma_2$), then Equations I-1 and I-2 reduce to:

$$M_{C1} = M_{C2} = \frac{U_1 - U_2}{a_1 + a_2} \quad (\text{I-3})$$

If $\gamma_1 \neq \gamma_2$ then the convective Mach numbers are slightly different but Equation I-3 is still a good approximation (25:1). If Equation I-1 is solved with Equation I-3 then:

$$\frac{U_c - U_2}{U_1 - U_2} = \frac{1}{1 + \sqrt{\frac{\rho_1}{\rho_2}}} \quad (\text{I-4})$$

This analysis for subsonic shear layers was validated by the experiments of Brown and Roshko (26) for variable density shear flows. Papamoschou, by actually measuring the convective velocity using a double exposure schlieren system (25), showed experimentally that this analysis was not completely correct for compressible flows but it correlates the data well. Papamoschou's theoretical convective Mach number (Eq. I-1) is the most widely accepted parameter used to correlate compressible shear layers and is the one used in this study.

I.1.2. Confined Jets and Shear Layers

Confined jets and shear layers are similar to free jets and shear layers except they are bounded by walls which impose boundary conditions on the flow. Two important effects caused by walls are: 1) the adverse effect of a positive axial pressure gradient and 2) the influence of reflected pressure waves from the walls on shear layers. The positive axial pressure gradient, ($dP/dX > 0$), that develops in jets and shear layers confined in constant area ducts is caused by the boundary layers that form on the walls and the increase in entropy resulting from the mixing within the shear layers. The pressure gradient slows down the streams and increases the density. The effects of the pressure gradient on shear layer growth rate can usually be accounted for by applying the free shear layer growth formulas to the local flow conditions. The shear layer width at any axial location can be determined by integrating over the entire shear layer length (33:15-16).

The pressure waves and oblique shocks that are generated from the large structures within the shear layers also cause axial pressure gradients. The pressure waves reflect off the duct walls and intersect the shear layer thus causing a series of discrete pressure increases in the axial direction. Theoretical studies on confined shear layers have found that reflected pressure waves effect shear layer growth when they intersect the shear layer (34, 36, 37).

There have been several numerical studies (35-37) investigating the instabilities associated with free and ducted compressible shear layers. Sandham and Reynolds (35:1-9) performed linear stability analysis and direct numerical simulation on free shear layers and found that for low Mach number flows the linear theory correctly predicted the

experimental growth rate trends attributed to density ratio, velocity ratio and Mach number. For convective Mach numbers above 0.6 they found that three dimensional stability modes began to dominate. The numerical simulations they performed showed a reduced growth rate with increasing Mach number, similar to the experimental results of Papamoschou and Roshko (31:453-477).

Numerical studies by Tam and Hu (37) showed that for unconfined free shear layers at high supersonic convective Mach numbers the Kelvin-Helmholtz instability was neutrally stable. If the same shear layer was confined in a rectangular duct then the coupling between the motion of the shear layer and the acoustic modes of the channel produced new instability waves that were unstable and enhanced mixing (37:1). These new instability waves are formed by the Mach waves emanating from the shear layer reflecting off the walls and back into the shear layer. At high supersonic convective Mach numbers these new instabilities, known as supersonic wall instabilities, were found to be the dominant instability mode of the shear layer. A recent numerical study by Greenough et al. (36) confirmed that there are two instability modes for confined shear layers, these being the Kelvin-Helmholtz and the supersonic wall instability modes. The wall instability modes first occur at supersonic convective Mach numbers, whereas the Kelvin-Helmholtz instability modes occur at both subsonic and supersonic convective Mach numbers. Greenough et al. (36) showed that the wall instabilities lead to shock formations that cause large pressure gradients particularly at high Mach numbers. These pressure gradients interact with the shear layer and cause large amounts of vorticity to be generated (36:7). The overall effect of the wall instabilities, and the increase in vorticity, is an increase in

mixing for confined shear layers which is greater than unconfined shear layers at equal supersonic convective Mach numbers.

Guirguis (38:1-7) performed numerical investigations of free and confined shear layers with the same results as the others (35-37), but he also looked at shear layers developed between underexpanded and overexpanded jets. Guirguis found that mixing was enhanced when the static pressures across the end of the splitter plate were unequal. The numerical simulations showed that a mismatch in exit pressure caused the shear layer to begin to roll-up which resulted in large scale mixing. The unconfined shear layers with matched pressures across the splitter plate did not exhibit the same kind of large scale mixing. His paper was unclear as to whether he also simulated a confined shear layer with matched pressures.

I.1.3. Shock - Shear Layer Interactions

There has been some research in SSLIs for mixing enhancement of supersonic shear layers and jets. In recent years both numerical (39, 40, 41) as well as experimental (18, 42, 43) studies have been conducted. In most cases the phenomenon investigated was the effect a misalignment of the pressure gradient and the density gradient had on the generation of vorticity. Both numerical and experimental studies of shock waves interacting with low density bubbles or cylinders of gas have shown that large amounts of vorticity can be generated resulting in rapid mixing of the light gas bubbles with the denser surrounding gas (40, 41, 44). In contrast, two studies where oblique shock waves impinged on two dimensional supersonic air-air shear layers have revealed no increase in mixing as had been expected (18, 43).

A study by Menon did show an increased jet width when an oblique shock interacted with a helium-nitrogen shear layer (42:7). The shear layer was made by injecting helium axially, at sonic conditions, behind a rearward-facing step into a Mach 2.5 nitrogen stream. One of the most significant differences between the work by Menon (42) and that by Shau and Dolling (18) and Samimy et al. (43) is the large density gradient across the shear layer due to the difference in molecular weight of helium and nitrogen. The large density gradient combined with the large pressure gradient across the shock caused the increased jet width observed by Menon.

I.2. Objective and Scope

I.2.1. Objective

The objective of this study was to experimentally investigate the effects of mismatched static pressure at the exit plane of three nozzles that produce parallel supersonic streams and develop a simple engineering model to estimate the mixing within the duct caused by the mismatched exit pressures. The supersonic streams were composed of a helium stream between two air streams bounded by the walls of a constant area duct. This configuration simulated parallel injection of hydrogen fuel into a co-flowing air stream such as might occur in a SCRAMJET combustor. The helium jet was injected into the duct at a higher static pressure than air streams in order to generate shocks that reflect off the duct walls and interact with the variable density shear layers increasing the mass entrainment from the generation of vorticity from the SSLIs and the excitation of the supersonic wall instability modes.

I.2.2. Scope

1. To evaluate the effect of exit pressure mismatch and shock-shear layer interactions on mixing, emphasizing the mixing region's growth and mass entrainment rates. Data were taken at three exit pressure ratios (EPR); 0.89, 1.49, 3.50 under the test conditions shown in Table I-1.

Table I-1: Test Conditions

EPR	AIR(AVERAGE)			HELIUM			MASS FLOW		
	Pe	Me	Ve	Pe	Me	Ve	He	AIR	TOTAL
	psia		ft/sec	psia		ft/sec	lbm/sec		
0.89	3.18	2.61	1918	2.84	1.67	3983	1.019	0.416	0.435
1.49	2.69	2.60	1911	3.99	1.61	3913	0.027	0.338	0.365
3.50	2.30	2.58	1906	8.04	1.60	3889	0.051	0.290	0.341

Pe - Static pressure at nozzle exit plane

Me - Mach number at nozzle exit plane

Ve - Velocity at nozzle exit plane

2. Develop a model that will provide first order estimates of the mass entrainment and mixing between fuel and air jets with high exit pressure ratios and shock shear layer interactions.

3. To establish an experimental facility using the AFIT blowdown wind tunnel and a secondary helium gas supply; to design and fabricate a probe to measure the molar fraction of helium within a supersonic air/helium stream in order to acquire quantitative measurements of the mixing of the helium jet within the air stream; and to develop a data

acquisition system and software to acquire and process the data needed for the investigation.

II. Theory

The flow model studied is shown in Figure II-1. The model is two dimensional and consists of a planar supersonic helium jet and two planar supersonic air streams, one on either side of the helium jet. All three streams discharge into a constant area duct where mixing takes place. The exit plane static pressures of the air and helium nozzles may or may not be matched before the jets enter the constant area duct. The effects of varying the exit plane pressures of the air and helium nozzles on the flow within the constant area duct is the topic of this study. Before discussing the theoretical effects of EPR and SSLIs some nomenclature needs to be discussed.

Throughout this study four terms are used to describe the various portions of the flowfield being studied: helium potential core, mixing region, shear layer and jet. These terms are illustrated in Figure II-1 and defined below.

Helium Potential Core - The helium potential core is the central region of the helium stream that is pure helium and can be modeled using potential flow equations.

Mixing Region - The mixing region is the viscous region where the two gases meet and mix by molecular and turbulent diffusion. The mixing region is characterized by gradients of the various gas properties (i.e. composition, velocity, density, pressure). The mixing region initially consists of two shear layers that grow until they merge into a region characteristic of a jet with no potential core.

Shear Layer - The shear layer is the region between the helium potential core and the air stream where mixing of the helium and air is taking place. The mixing region after the two shear layers, that bound the helium potential core, merge can be modeled as two shear

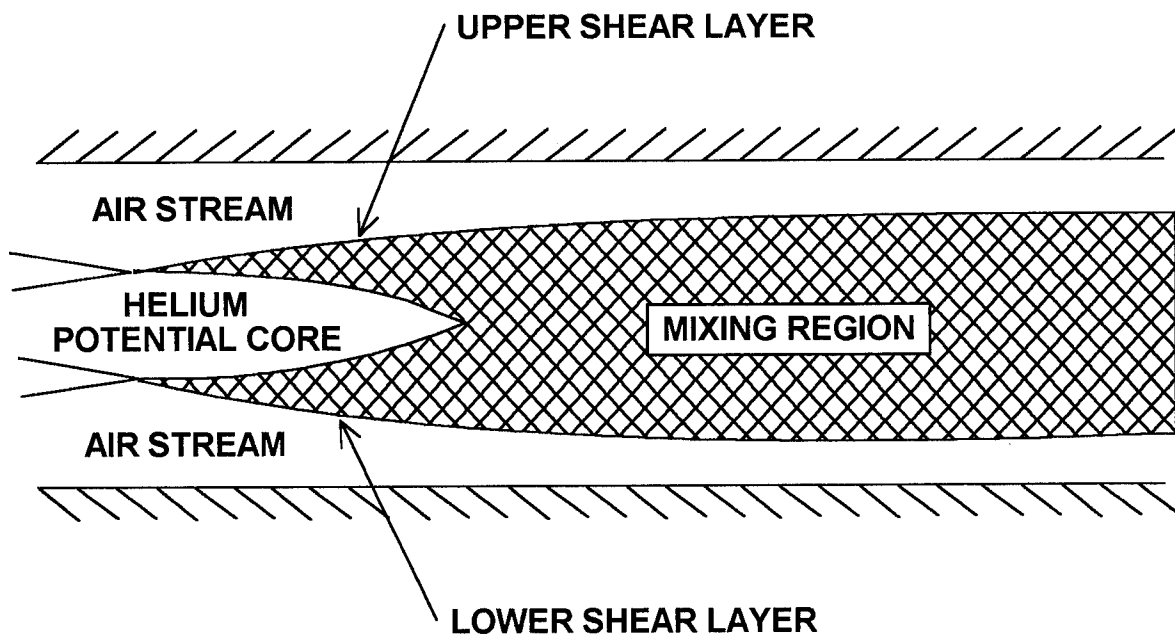


Figure II-1: Experimental flow model

layers that have a common boundary along the mixing region's (i.e. duct's) centerline. The gas mixture properties along the duct centerline will define one of the gas streams making up the shear layer.

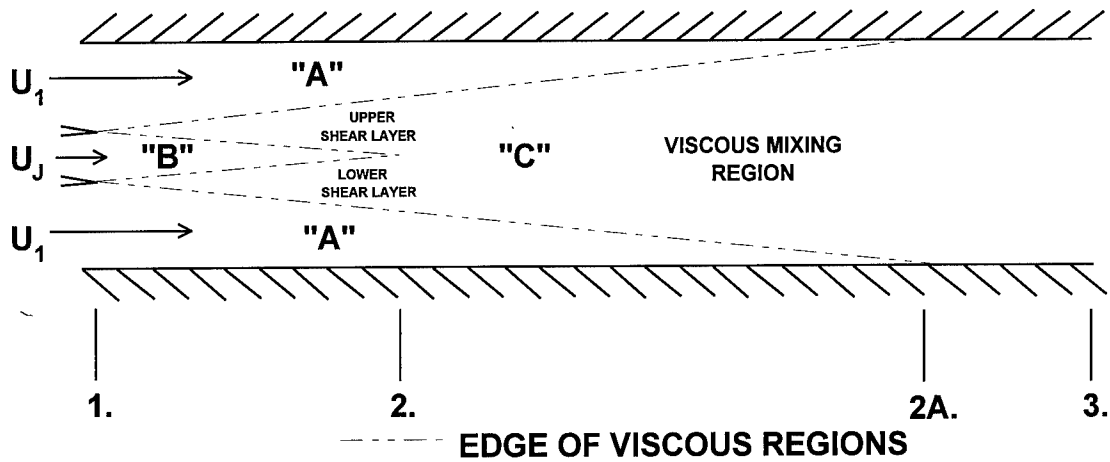
Jet - The term jet refers to all the regions that have any amount of helium present. The jet includes the helium potential core and the mixing region. The term jet will be used in the discussions on growth and entrainment rates in order to have terminology similar to that commonly found in the literature.

II.1. Exit Pressure Ratio (EPR)

The EPR is defined as the ratio of the nozzle exit plane static pressure of the helium jet to that of the air jets. There are three possible EPR cases. First there is the case where the exit pressures of the helium and air jets are matched which gives an EPR of unity ($EPR = 1$). This condition is referred to as case I or the ideally expanded case. The second possibility is when the helium exit pressure is less than the air exit pressure which gives an EPR less than unity ($EPR < 1$). This condition is referred to as case II or the overexpanded case. Finally, there is the condition where the helium exit pressure is greater than the air exit pressure and the EPR is greater than unity ($EPR > 1$). This condition is referred to as case III or the underexpanded case.

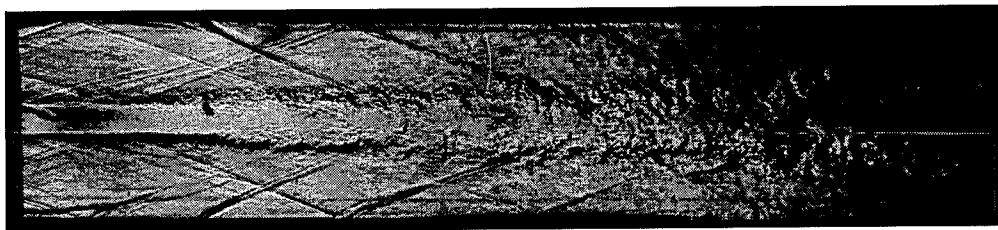
II.1.1. Case I: $EPR = 1$

In case I (Fig. II-2) the helium jet's exit pressure is equal to the air jet's exit pressure. The two shear layers, that separate the helium and air streams, each grow and entrain fluid from both the air and helium streams. Eventually the shear layers merge



STATION 1. JET EXIT PLANE
 STATION 2. END OF HELIUM POTENTIAL CORE
 STATION 2A. END OF AIR POTENTIAL CORE
 REGION "A" AIR POTENTIAL CORE
 REGION "B" HELIUM POTENTIAL CORE
 REGION "C" VISCOUS MIXING REGION

a) Theoretical Model



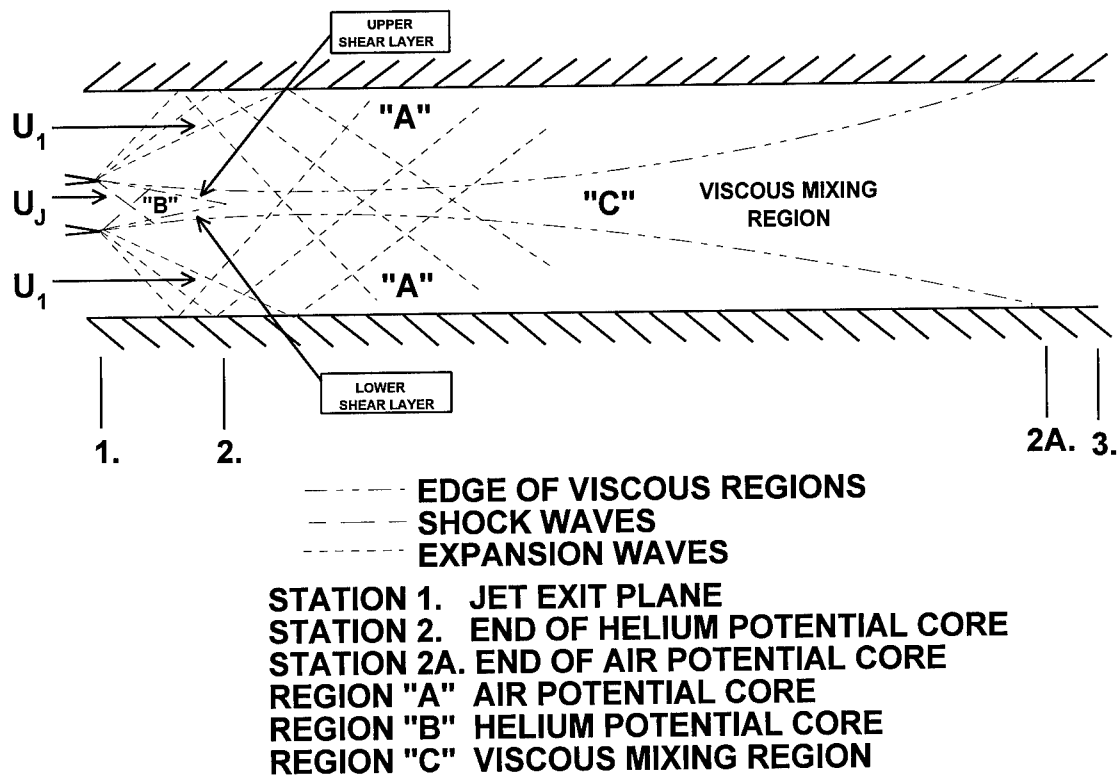
b: Representative schlieren photograph

Figure II-2: Case I Theoretical Model

defining the end of the helium jet's potential core. When the two shear layers merge the centerline helium concentration begins to decay until the entire flow reaches equilibrium and uniform fluid properties are achieved across the duct. Under ideal conditions there would be no shocks or expansion waves generated but under actual conditions, shocks, expansion waves, and Mach waves are present (Fig. 2b). These waves are generated from the boundary layer separation at the tips of the nozzles and from small flow changes caused by the large structures within the shear layers. The expansion waves and shock waves generated from the boundary layer separation and the large structures within the shear layer are unsteady.

II.1.2. Case II: $EPR < 1$

For case II the helium jet exit pressure is less than the air exit pressure thus the helium jet acts like flow from an overexpanded nozzle. In case II, Figure II-3, the flowfield pattern is governed initially by the effects of the helium and air jets reaching an equal pressure immediately downstream from the exit plane. The pressure is equalized by a combination of shock waves and Prandtl-Meyer (P-M) expansion waves originating from the tip of the splitter plate between the helium and air jets. Within the duct there will be a series of shocks and expansion waves that will determine the location of the shear layer centerlines that defines the jet boundary. The wave pattern within the helium jet will start with an oblique shock in order to increase the pressure within the helium jet to that of the surrounding air streams. The air streams will at the same time expand toward the duct centerline reducing the air static pressure until an equilibrium pressure is reached across the shear layer separating the air and helium streams. The final location of the two shear



a) Theoretical Model



b: Representative schlieren photograph

Figure II-3: Case II Theoretical Model

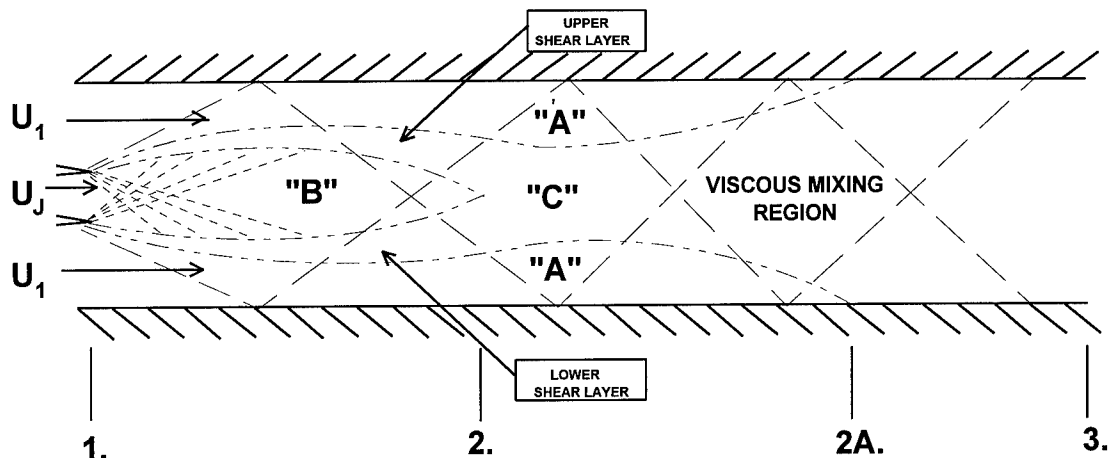
layers that separate the helium and air streams will be determined by the amount of turning needed to equalize the pressure across the shear layers. The two shear layers initially will be directed inward toward the duct centerline then turn and proceed axially down the duct. It should be noted that Figure II-3a represents ideally what is happening in the mixing duct. In reality there will be numerous unsteady shocks, expansion waves and Mach waves caused by boundary layer separation at the end of the nozzles, the large structures within the shear layer and the turning of the shear layers. Figure II-3b is a representative schlieren of case II with a EPR slightly less than unity thus the turning of the shear layers is not as dramatic as in the theoretical model.

Along each shear layer, entrainment and diffusion are taking place which causes the two shear layers to grow and eventually merge. As in case I the point at which the shear layers meet defines the end of the potential core of the helium jet. In case II the merging of the shear layers takes place sooner (upstream) than in case I, because the pressure mismatch deflects the shear layers toward each other, as seen in Figure II-3. For a fixed geometry and fixed air stream pressure the case II helium jet has a lower mass flow rate than the case I helium jet. In the limit as the EPR approaches zero (i.e. the helium jet exit pressure approaches zero) the shocks in the helium jet move into the nozzle and the flow approaches a base flow with small amounts of injection. Base flows and base flows with small amounts of air injection at low velocity have been studied by Chow (45), Korst (46), and Durand (47).

II.1.3. Case III: $EPR > 1$

The final case, case III Figure II-4, has an EPR greater than unity, thus the helium jet acts like the flow from an underexpanded nozzle. The helium jet expands outward into the air streams through a P-M expansion in order to equalize the jet's helium exit static pressure with the static pressure of the air streams. As the air-helium shear layers turn outward oblique shocks form in the air streams which reflect off the confining walls redirecting the air streams parallel to the wall. The result of the oblique shock is a compression of the air stream in order to match the helium jet's exit pressure. After the shocks in the air streams reflect off the duct walls they pass through the helium jet toward the opposite wall. The expansion waves within the helium jet reflect off the shear layer as oblique shocks and proceed downstream in a periodic pattern as shown in Figure II-4. Figure II-4a, like the previous two figures, is an idealization of the flowfield and in reality there will be numerous unsteady shocks, expansion waves, and Mach waves as discussed in cases I and II (Fig. II-4b).

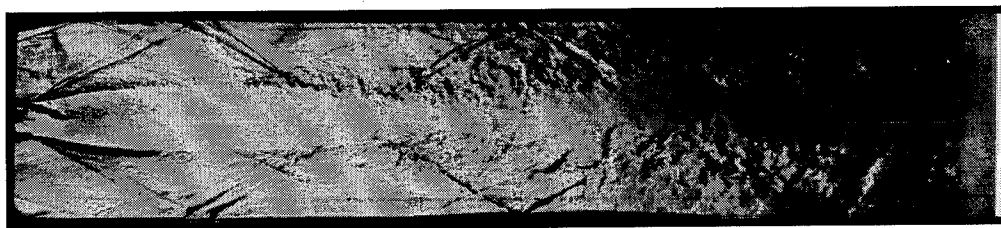
As in the previous cases the two shear layers grow due to entrainment of both helium and air and eventually merge defining the end of the helium jet's potential core. The potential core in this case is longer than that of cases I and II because the helium jets boundaries are displaced outward due to the nature of the underexpanded helium jet. In the limit as the EPR goes to infinity the flow becomes a helium jet expanding into a vacuum, but bounded by the duct walls.



- - - - - EDGE OF VISCOUS REGIONS
 - - - - - SHOCK WAVES
 - - - - - EXPANSION WAVES

STATION 1. JET EXIT PLANE
 STATION 2. END OF HELIUM POTENTIAL CORE
 STATION 2A. END OF AIR POTENTIAL CORE
 REGION "A" AIR POTENTIAL CORE
 REGION "B" HELIUM POTENTIAL CORE
 REGION "C" VISCOUS MIXING REGION

a) Theoretical Model



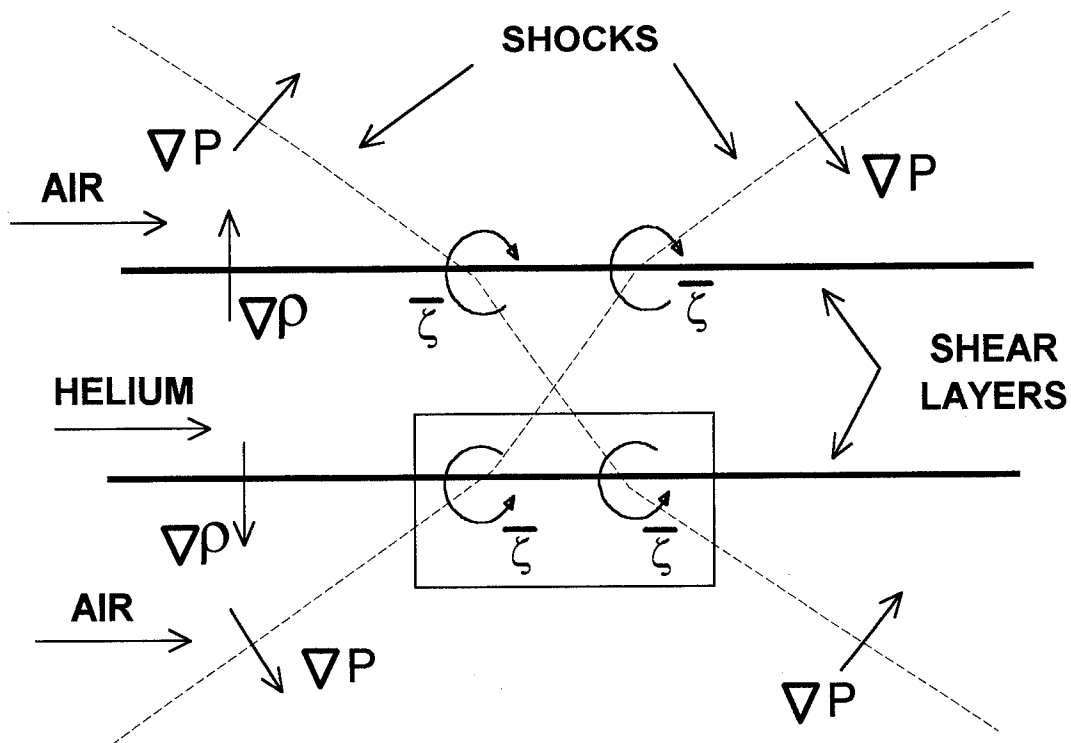
b: Representative schlieren photograph

Figure II-4: Case III Theoretical Model

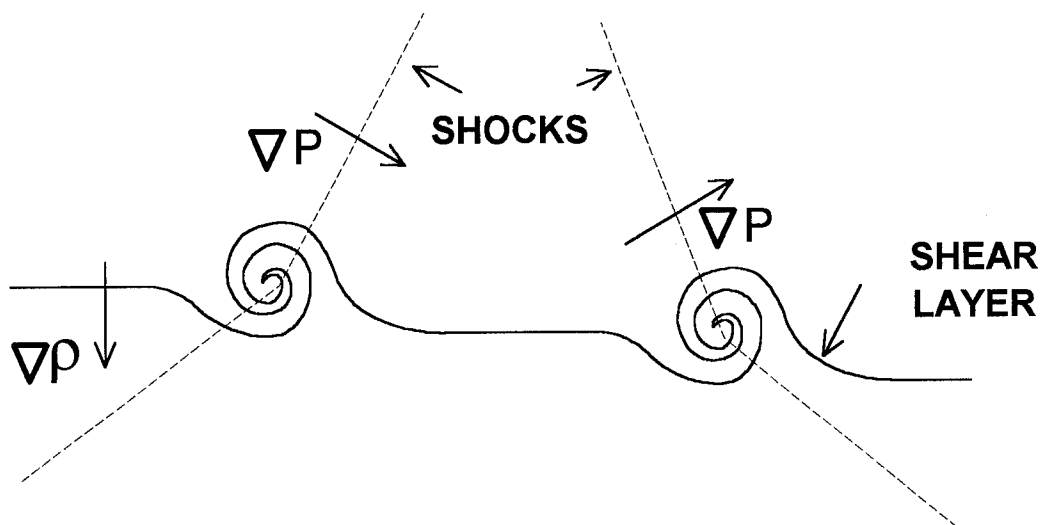
II.2. Shock - Shear Layer Interactions

In order to fully understand the dynamics and the mechanism of mixing for cases II and III, where the EPRs are not unity, one must investigate the SSLI. In this study the SSLI of interest is that of an oblique shock and a variable density free shear layer. The variable density is important because without a large density gradient across the shear layer the effect of the shock on the mixing is minimal as was found by Shau and Dolling (18:7) and Samimy et al. (43:5).

The model that will be used to investigate the SSLI is shown in Figure II-5 which represents the SSLI observed in case III ($EPR > 1$). Figure II-5 shows a supersonic helium jet bounded by two supersonic air streams with two oblique shocks intersecting on the centerline. The helium/air shear layer has a density gradient ($\nabla\rho$) that is directed outwards from the centerline. The shock waves have a pressure gradient (∇P) that is perpendicular to the shock waves as shown in Figure II-5a. The misalignment of the density and pressure gradients is important because the inviscid equation for the time evolution of vorticity (Eq. II-1) will have a nonzero source term (44:432). In other words, if a shock wave passes through a shear layer with a density gradient, vorticity will be generated. The generation of vorticity at the intersection of the shock and shear layer causes additional entrainment and mixing of the air and helium jets.



a) Simplified model of shock-shear layer (jet) interaction



b) Details of shock-shear layer interaction

Figure II-5: Shock-shear layer interaction model

$$\frac{d\bar{\zeta}}{dt} + \bar{\zeta} \nabla \cdot \bar{V} = \bar{\zeta} \cdot \nabla \bar{V} + \overline{(\nabla \rho \times \nabla P) / \rho^2}$$

Source Term

$\bar{\zeta}$ = Vorticity
 ρ = Density
P = Pressure
t = Time
 \bar{V} = Velocity

(II-1)

Figure II-5b shows conceptually what may be happening at the intersection point of the shock and the shear layer. At the intersection point a vortex forms that rapidly entrains fluid from the freestream into the mixing layer causing the mixing layer to grow rapidly. The vortex may remain stationary, pumping freestream fluid into the shear layer or it may break off and travel downstream as a large vortical structure while a new vortex forms at the intersection point. The author believes that when the vortex reaches a particular size, viscous interactions with the freestream causes it to break off and travel downstream.

Vorticity generation has been demonstrated by the intersections of normal shocks and low density gas bubbles (40, 41, 44). Recent studies have investigated the effects of oblique shocks (18) and curved bow shocks (43) on free shear layers created by supersonic and subsonic air jets. The results of these studies have shown little effect on the growth or structure of the shear layer. The minimal effect is thought to be due to small density gradients which cause the amount of vorticity generated to be small. A study by Menon (42) on helium and nitrogen shear layers did show an increase in growth rate due to SSLIs. In Menon's case there was a large density gradient across the shear layer which, combined with the pressure gradient of an oblique shock wave, caused

considerable vorticity to be generated. The increased vorticity in turn caused enhanced mass entrainment into the shear layer and the increase in growth rate observed by Menon.

II.3. Entrainment and Growth Rates

Entrainment and growth rates of shear layers and jets quantify mass transfer from the freestream to the viscous shear layers. The transfer of mass occurs through large scale mixing when turbulent eddies capture freestream fluid and entrain the mass into the viscous shear layer and by molecular diffusion when the motion of the individual molecules mix freestream fluid into the viscous region. The turbulent eddies are the dominant mass transfer mode on a large scale while molecular diffusion is required for fine scale mixing which allows chemical reactions to occur. Two parameters that are useful in determining the total mass transfer taking place are the shear layer's entrainment and growth rates. Both parameters deal with the amount of fluid entrained into the shear layer. The entrainment rate deals with the amount of mass within the shear layer boundaries without regard to the physical size of the shear layer. The shear layer growth rate deals with how the shear layer expands or grows as freestream fluid is absorbed into the shear layer.

II.3.1. Entrainment Rate

The entrainment rate is defined as the amount of mass entrained into the viscous region per unit length. The non-dimensional parameter that was used by Ho and Gutmark (48:386), in their study of mass entrainment into circular and elliptical free jets, was the entrainment ratio (ER) defined by Equation II-2;

$$ER = \frac{Q(X) - Q_{He}}{Q_{He}} \quad (II-2)$$

where $Q(X)$ is the total mass flow rate within the jet boundaries at axial location X and Q_{He} is the initial mass flow rate of the helium jet. The ER measures the degree of entrainment by relating the entrained mass to the initial mass of the jet. The ER is fine for free jets but misleading for confined jets. Confined jets unlike free jets have a limited amount of fluid to entrain therefore a parameter that measures the degree of entrainment should consider the limited fluid within the duct. A new parameter, the duct mixing ratio (DMR), is proposed to evaluate entrainment for confined jets and shear layers. The DMR unlike the ER takes into account the finite amount of air available for mixing and entrainment within the duct. The DMR parameter is given by Equation II-3;

$$DMR = \frac{Q(X) - Q_{He}}{Q_{Air}} \quad (II-3)$$

where $Q(X)$ is the total mass flow rate within the jet at axial location X , Q_{He} and Q_{Air} are the initial mass flow rates of the helium and air jets respectively. The DMR takes on a value of 0 when no mixing has taken place and 1 when the entire air stream has been mixed into the helium jet.

The entrainment rate can be calculated from either the ER or the DMR but for confined jets the DMR is preferred. The non-dimensional entrainment rate is then the rate at which the DMR changes per unit length downstream, $d(DMR)/dX$. The dimensional entrainment rate can be determined by multiplying the non-dimensional entrainment rate by the initial mass flow of air (Eq. II-4).

$$\frac{d\dot{m}}{dX} = (\dot{m}_{Air}) \frac{d(DMR)}{dX} \quad (II-4)$$

The helium jet boundaries in this study were arbitrarily defined as the locus of points at which the helium molar fraction is <0.03 . The mass flow rate within the helium jet at axial location X , $Q(X)$, is determined by integrating the mass flux across the width of the helium jet. The initial mass within the helium jet is determined from the condition at the throat of the helium nozzle.

II.3.2. Growth Rate

The growth rate of a shear layer can be measured by determining the diffusion rate of a jet's concentration, velocity, temperature, momentum, or total pressure. Growth rates are usually the cross-stream diffusion distance of a given quantity per unit distance downstream (i.e. inches laterally per inch axially or in/in). The most common published growth rates are the visual (determined by either schlieren and shadowgraph photography), pitot pressure, total pressure, vorticity and concentration. The growth rate can be related to the entrainment rate if the velocity and density profiles of the shear layer or jet are known. In most studies dealing with supersonic heterogeneous flows the concentration, velocity and density profiles are not measured or reported and only visual and pitot pressure growth rates are reported. The pitot pressure is the pitot probe pressure measurement with no correction for the normal shock. If the loss in total pressure due to the normal shock in front of the pitot probe is accounted for then the measured pressure reported is the total pressure. To account for the normal shock the local static pressure and gas composition must be known. In most studies they are not measured across the shear layer. In this study visual and concentration growth rates were determined from schlieren photographs and contour plots of helium molar fraction.

II.4. Modeling

Modeling can extend from simple empirical relations that fit the data to complex computer codes that require hours of processing time on super computers. In this study a model based on simple empirical relations similar to those used by Schetz et al. (49, 50) was developed from the experimental data acquired.

Schetz et al. (49) developed a simple engineering model for mismatched exit pressures in wall jets that could be extended to cover the three EPR cases previously discussed. For the potential core regions, where there are no viscous effects taking place, Schetz uses either supersonic or hypersonic small disturbance theory and weak shock relations to calculate the fluid velocity and pressure. The viscous regions are modeled as a one-dimensional flow that represents the average properties in the viscous region. The model relies heavily on empirical relations to account for the entrainment of freestream fluid into the one-dimensional viscous regions.

The empirical entrainment model used by Schetz is based on the difference in momentum between the inner and outer freestreams (50:3). The entrainment model was developed by Ferri based on the work by Crocco and Lees on wall boundary layers. Crocco and Lees proposed that mass entrainment rate into boundary layers could be calculated from the momentum of the freestream.

$$\frac{dm}{dX} \approx \rho u \quad (II-5)$$

Ferri extended this theory to shear layers by basing the entrainment rate on the difference in momentum between the two freestreams (50:3).

$$\frac{dm}{dX} \approx \rho u_1 - \rho u_2 \quad (\text{II-6})$$

One of the objectives in this study was to further extend the entrainment theory proposed by Ferri and used by Schetz to jet flows where the momentum of the second flow is the momentum of the jet's centerline. The model must also be modified to account for additional entrainment resulting from SSLI. This enhanced theory will be developed in Chapter VII.

Schetz et al. (49) applied Ferri's model to case III flows for slot injection (wall jet) and had fairly good results matching the limited data available within the range of $0.8 \leq \text{EPR} \leq 1.25$. Schetz points out that for large EPR's the entire flow pattern can change drastically due to shock and expansion wave interactions with the shear layer (49:8). Simplified models of Schetz's type have trouble handling these cases with complicated shock wave and expansion wave patterns and complicated SSLIs. In order to model large EPRs and binary gas mixtures accurately, as in this study, a model that accounted for the effects of shocks and expansion waves, diffusion of multi-gases and viscous effects on the flowfield was needed.

III. Experimental Apparatus

The experiments for this study were performed in the AFIT blowdown gasdynamic facility. The basic facility included an air supply, a helium gas supply, a test section, a traversing mechanism, and a data acquisition system. The instrumentation used for this study consisted of pressure taps on the sides of the test section, two probes that traversed the flowfield, one to measure helium concentration and one to measure pitot pressure, and a schlieren optical system.

III.1. Blowdown Gasdynamic Facility

III.1.1. Air and Vacuum Supply

A schematic of the blowdown facility is shown in Figure III-1. The air for the facility is provided by two compressors each fitted with condensation and absorption air dryers. The air is supplied to the laboratory via a 3 in pipe that feeds the blowdown facility. The air then passes through a cyclone separator and a paper filter before passing through a 3 in flexible hose to the Grove dome valve that regulates the primary air supply. After the dome valve a manually operated 3 in disk valve is used to control the air flow into the stilling chamber. The stilling chamber is 12 in in diameter and 4 ft long and contains baffles, screens and a final paper air filter to condition the air flow. The baffle and screens are used to smooth the flow and reduce turbulence before the flow enters the test section. The dome valve, disk valve, and stilling chamber are mounted on rails that allow them to be rolled back from the vacuum chamber for installation of the test section. The test section is bolted between the stilling chamber and the dump tank. The dump tank

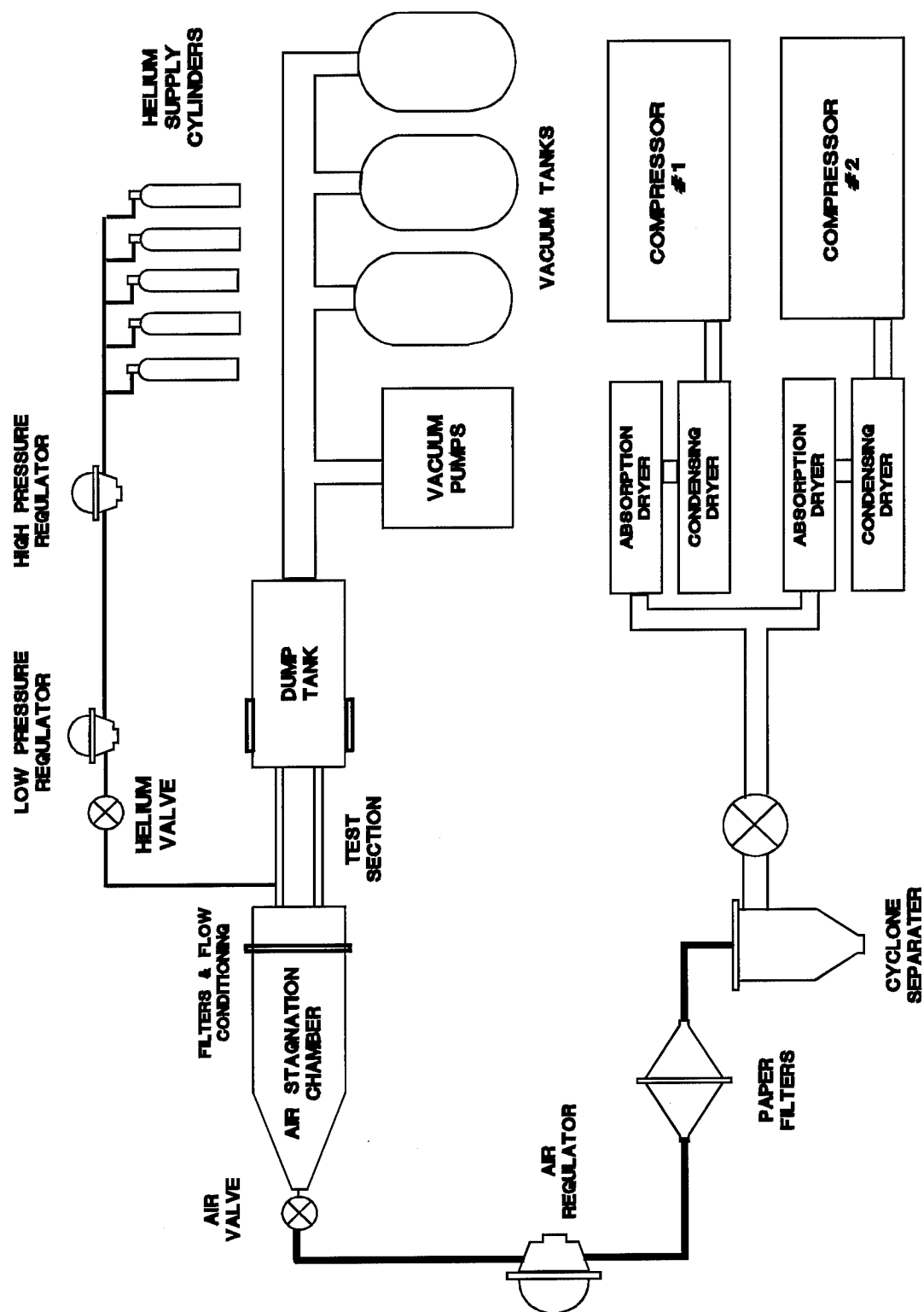


Figure III-1: Schematic of AFIT blowdown facility

is connected via 12 in pipe to a vacuum system that has a 540 ft³ reservoir tank that is evacuated by three vacuum pumps. Run time for the system varies depending on the maximum acceptable back pressure and the mass flow rate. The configuration used in this study allowed run times on the order of 60 s before the back pressure became marginal to unacceptable.

III.1.2. Helium Supply

Helium was injected coaxially with the supersonic air streams. A helium gas supply system was constructed to deliver and control the required helium at the appropriate pressure. Five standard gas bottles were attached to a manifold which piped the gas through two Grove dome valves used to regulate the pressure in a two-step process. The first dome valve reduced the pressure to approximately 300 psig; the second reduced the pressure to that required for the various 0 to 100 psig tests. After the second dome valve, a solenoid valve was used to start and stop the flow into the test section.

III.1.3. Traversing Mechanism

A traversing mechanism that could be operated remotely was designed and constructed for installation within the dump tank. The mechanism traversed in two dimensions which allowed probes to measure flow properties across the jets at various axial distances from the nozzle exit plane. The probes were mounted in a wedge shaped plate that moved vertically on four support shafts mounted to a carriage that moved horizontally. The wedge shaped plate was fitted with a digital encoder (Astrosystems Inc model MT23-1 /100) that provided vertical position data to within 0.001 in. The plate

was driven vertically by a DC motor. The voltage supplied to the motor determined its speed; the polarity its direction. The vertical movement of the plate was limited by two adjustable microswitches to prevent damage to the probes and sensors. The carriage holding the probe support plate and its associated vertical drive and position mechanism, was moved horizontally, in the axial direction, by a second DC motor controlled in the same manner as the vertical drive motor. The horizontal position was measured manually with a machinist's rule. The horizontal positioning was accurate to within $1/32$ in (0.0313 in). The maximum range of the traverser was 12 in horizontally and 4 in vertically which was more than sufficient for this study. The traversing mechanism was mounted within the dump tank such that vertical traverses on the centerline of the test section could extend to within 0.125 in of the upper and lower walls.

III.1.4. Test Section

The test section was designed to have a nominal Mach 3 air jet on either side of a nominal Mach 2 helium jet. The three jets mixed within a constant area duct before discharging into the vacuum chamber. The test section consisted of upper and lower walls that contained two of the four nozzle contours needed to make up the two air nozzles as well as 7 in of straight section for the constant area mixer. A center body containing the remaining two contours for the air nozzles as well as the complete helium nozzle, was mounted between the walls to complete the test configuration shown in Figure III-2. The upper wall, lower wall and center body were all mounted between two side walls with a series of alignment pins and bolts. Two sets of side walls were constructed, one from Plexiglas with a series of pressure ports for measuring static pressures, and the other set

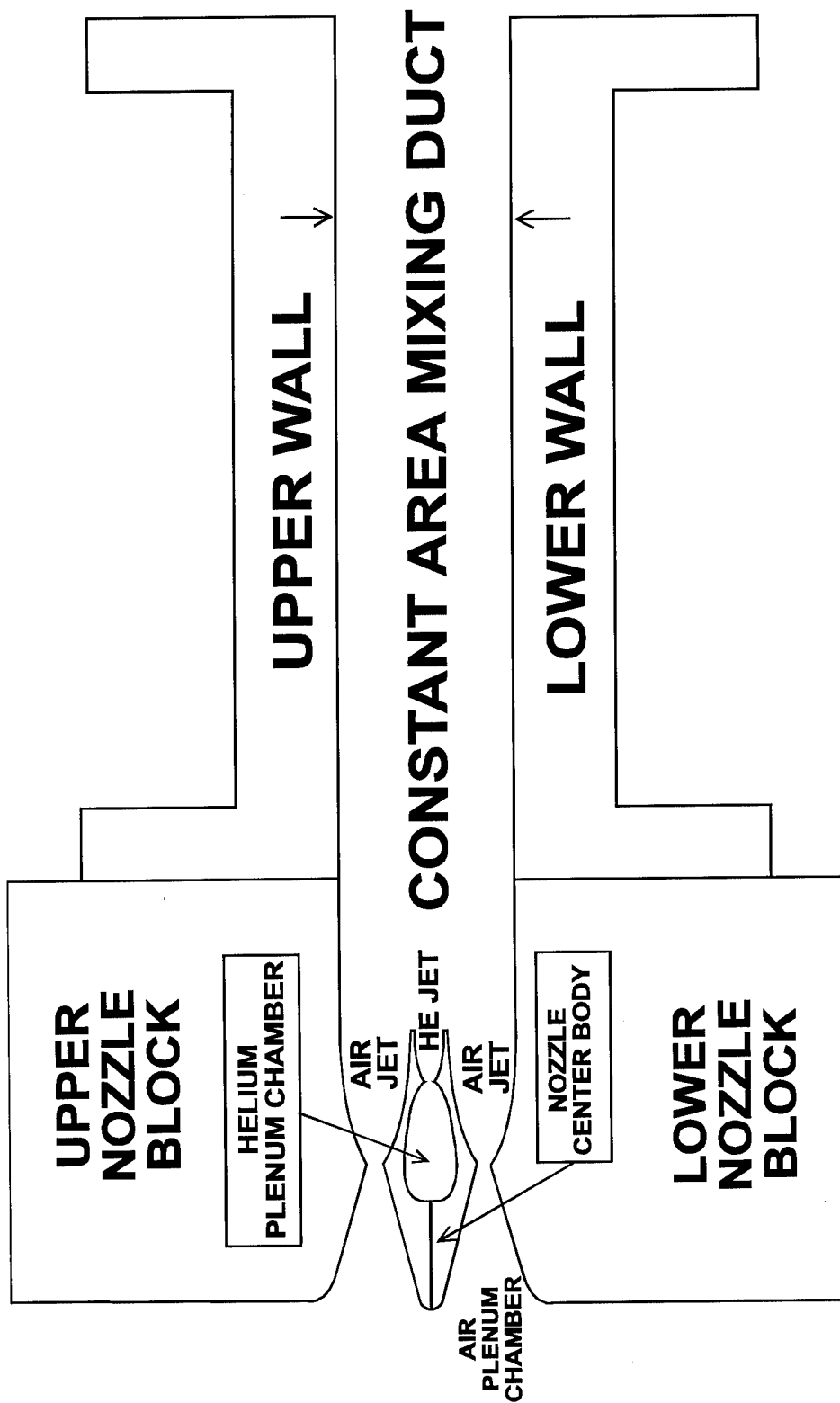


Figure III-2: Test section layout

from aluminum with optical glass inserts for taking schlieren and shadowgraph pictures. Circular end plates were attached for mounting the test section between the air stilling chamber and the dump tank.

The center body used for this study contained a Mach 2 nozzle designed for a ratio of specific heats (γ) of 1.667, that of helium. The nozzle contours were determined by the method developed by Foelsch and used by Papamoschou (24:14) because it allowed an analytical formula for the contours that was easily programmed to provide the coordinates of the necessary nozzle designs. The air nozzles were designed to have an exit height of 0.5 in and the helium nozzle with an exit height of 0.2 in. The test section is 1 in deep. The throat and exit areas of each air nozzle was 0.118 in² and 0.5 in² for a combined throat and exit areas of 0.236 in² and 1.0 in² respectively. The throat and exit areas of the helium nozzle was 0.131 in² and 0.2 in² respectively. There were no allowances for boundary layer thickness in the design of the nozzles thus the actual Mach numbers were less than the two-dimensional design values.

III.2. Instrumentation and Data Acquisition

The data collected consisted of schlieren photographs, side wall static pressure measurements, centerline pitot pressure surveys and centerline concentration surveys. The side wall static pressure measurements and the centerline pitot pressure measurements were straight forward and posed no problem. The concentration measurements required the design and construction of a novel probe that analyzed the gas mixture for helium concentration while the probe traversed the flowfield. The details of its operation, design,

and calibration are contained in Chapter IV. The schlieren photographs were taken for a qualitative interpretation of the flowfield.

III.2.1. Pressure Measurements

Twenty-six static pressure ports were installed on one set of test section side walls. The pressure ports were located as shown in Figure III-3. Because of limitations in the data acquisition system only a few could be used at any one time. The static pressure ports that were used were connected to either a 5 or 15 psia transducer (Endevco model 8510B-5 or 8510B-15) via 0.060 in tygon tubing. The static pressure ports that were not being used during a particular test were capped.

The total pressure within the air stilling chamber was monitored by an Endevco model 8510B-100 pressure transducer mounted in the end of the stilling chamber. The helium total pressure was monitored by an Endevco model 8510B-15 pressure transducer attached to a 0.050 in stainless steel tube leading to the helium plenum chamber.

The total pressure measurement traverses of the flow at various axial locations in the mixing chamber were conducted with a total pressure probe constructed from a 0.25 in stainless steel tube with a 0.125 in stainless steel tube insert that protruded 2 in from the 0.25 in tube. A small 0.062 in diameter (Endevco model 4385-50) absolute pressure transducer was mounted within the 0.125 in tube. A conical end cap with a 0.020 in diameter hole was installed over the end of the transducer to increase the spatial resolution of the probe.

Each of the pressure transducers was connected to an Endevco Model 4225 power supply and Endevco Model 4423 signal conditioner that amplified the signal and

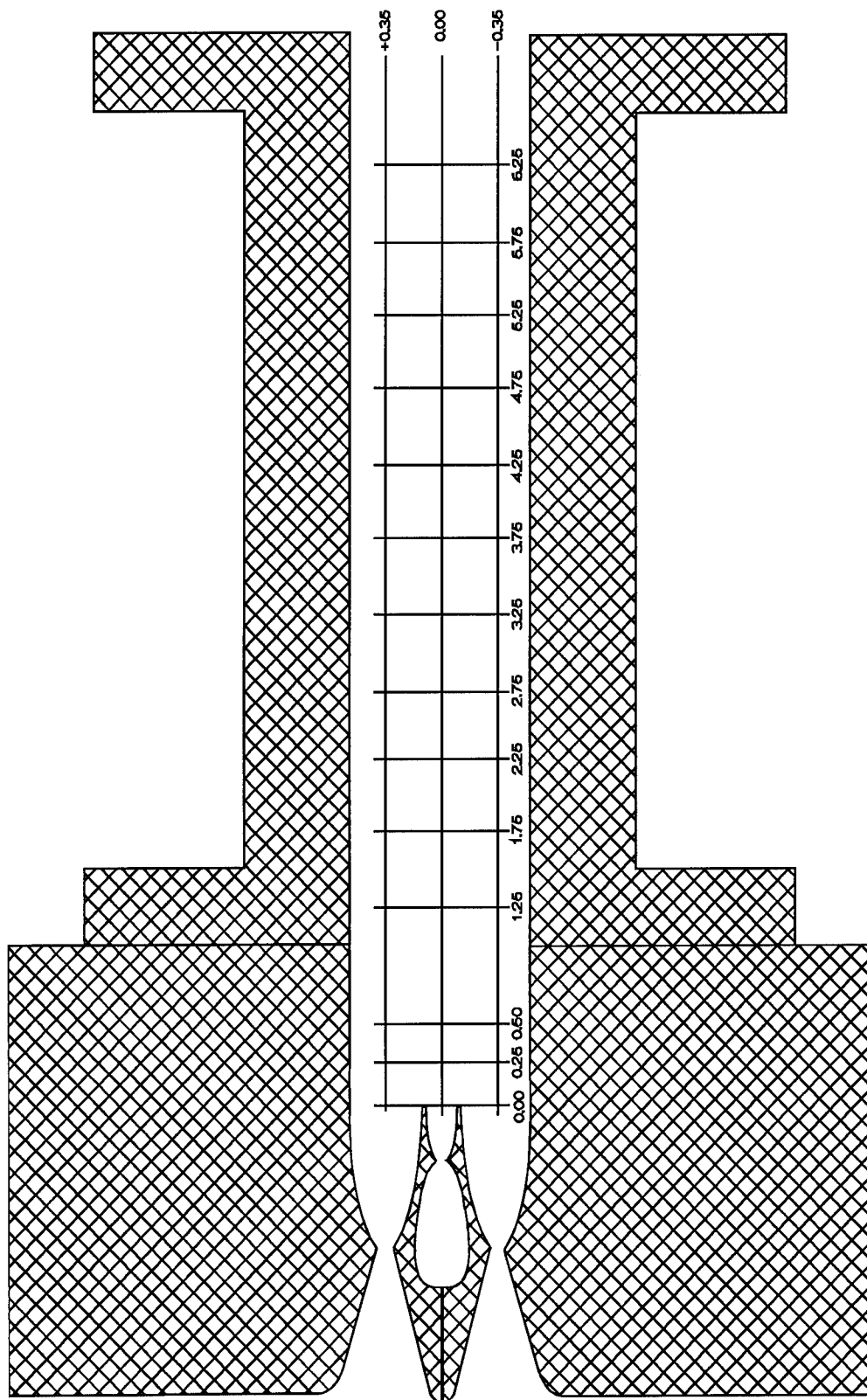


Figure III-3: Location of side wall static pressure ports

minimized electronic noise. The pressure transducers and signal conditioners were calibrated as a unit in order to minimize experimental error. The calibration was performed using a dead weight tester and a digital voltmeter. The amplified signal then went to the data acquisition system.

The Endevco model 8510B transducers, used for the side wall static and the air and helium total pressures, are differential transducers that required a reference pressure which was supplied by a Cenco model 92003 Megavac vacuum pump. The reference pressure was maintained at 1 torr or less as monitored by a precision Wallace and Tiernan vacuum gauge (Model FA160).

III.2.2. Data Acquisition System

The data acquisition system consisted of a Data Laboratories waveform recorder Model DL1200, henceforth referred to as the DL1200. The DL1200 contained eight 12 bit analog to digital (A/D) converters that simultaneously sampled eight channels at the preset sample rate and stored the data. The output from the vertical position encoder was recorded in the binary input ports of the DL1200. The reading and storing of the binary data at these ports were simultaneous with that for the eight A/D converters. The data sampling rate chosen allowed the probes to continuously traverse the flowfield and correlate the data with the vertical position. The DL1200 as configured allowed 4096 data points to be obtained on each of the 8 analog and 32 binary channels. The recorded digital data were downloaded via an IEEE-488 data bus to a Zenith 386 personal computer (PC) and converted to voltages and then into engineering units as required. All

of the software required to perform the data acquisition and data reduction was written by the author specifically for this study.

III.2.3. Schlieren Camera System

A schlieren camera system was set up for making visual observations of the flowfield. The system was the standard Z-configuration shown schematically in Figure III-4. Two light sources were used, a steady arc lamp for setup and a spark lamp (Cook Technologies Spark Gap Unit #596-4116) for short duration (160 ns) still photographs. The photographs were recorded on Polaroid film with an ASA rating of either 400 or 3000 depending on the particular setup. Photographs were taken with the knife edge both vertical and horizontal in order to get a good qualitative representation of the density gradients in both the longitudinal and lateral directions.

III.2.4. Test Procedures

The test procedure was fairly simple after the facility was setup, checked out, and ready for testing. The typical operating procedure was as follows:

1. Configure the test section to acquire the appropriate data.
2. Setup the DL1200 following the software prompts.
3. Open the air valve to initiate the flow of air.
4. Turn the IFA-100 from STAND-BY to RUN.
5. Switch on the helium flow.
6. Start the traverser moving downward.
7. Once the traverser has started to move, trigger the DL1200.

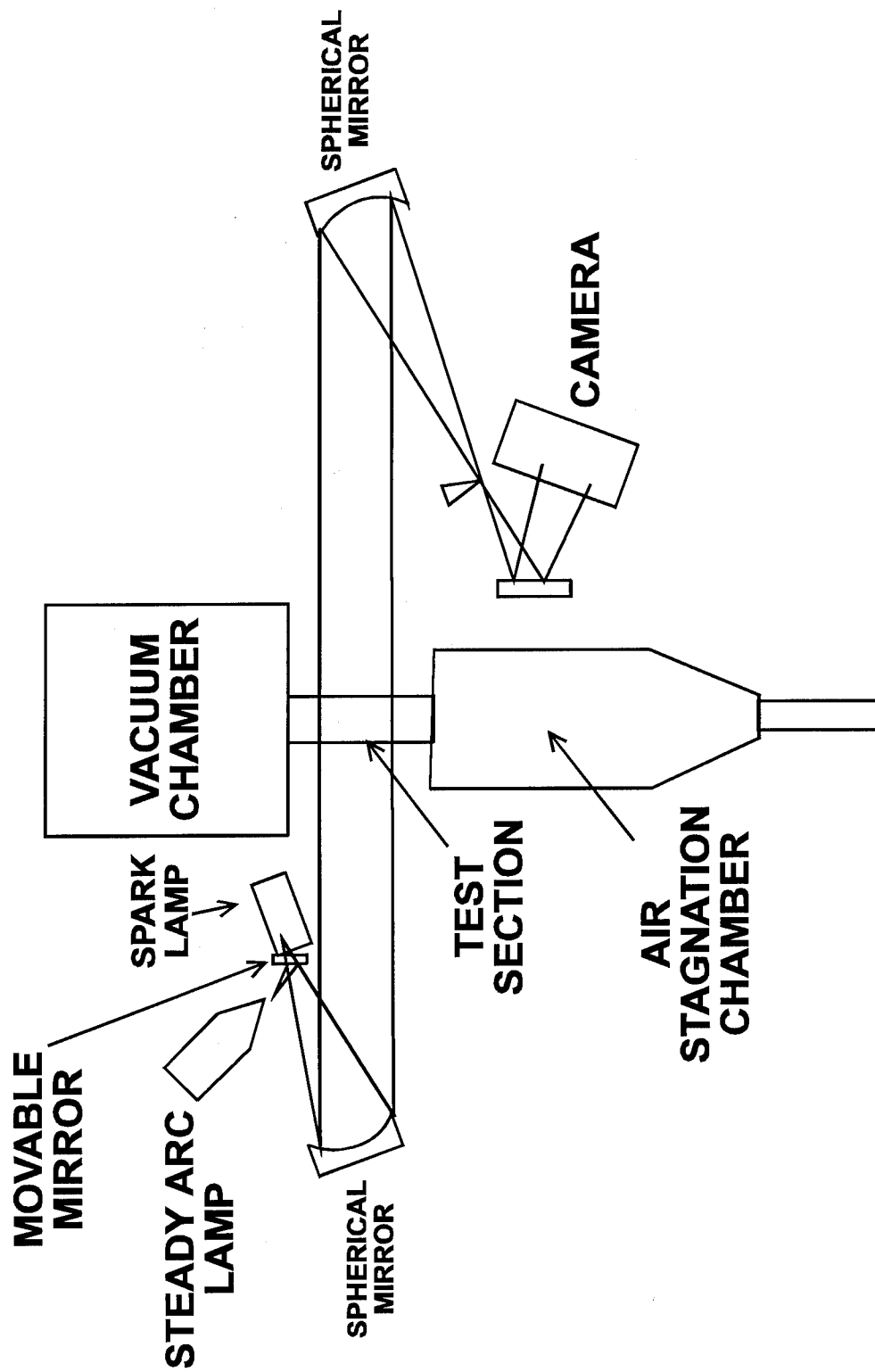


Figure III-4: Schematic of schlieren system

8. When the traverser has stopped at the end of the traverse switch off the helium flow.
9. Turn the IFA-100 to STAND-BY.
10. Close the air valve.
11. After the DL1200 stops taking data, the data are automatically downloaded from the DL1200 to the hard disk in the computer for storage and post processing.
12. After being downloaded the raw data are displayed on the screen for preliminary analysis.
13. If the preliminary analysis indicates that the data are good then the data are converted into engineering units; if not, the test is re-run.

III.3. Facility Performance

As expected the air and helium nozzles did not operate at the design conditions of Mach 3 and Mach 2 due to the boundary layer thickness not accounted for in their design. The exit plane static and pitot pressure measurements indicated that the upper and lower air nozzles operated at approximately Mach 2.6 and the helium nozzle operated at 1.6. The variations between the design Mach number and the actual Mach number measured was due to several factors. The largest factor was the presence of boundary layers on the walls of the nozzles which was not taken into account when the nozzles were designed. The boundary layers are clearly visible in the various schlieren photographs and are turbulent. The circumference of each air nozzle is 3.0 in, thus the boundary layer displacement thickness is roughly 0.05 in. The circumference of the helium nozzle is 2.4

in, thus the displacement thickness is 0.02 in. If the difference in Mach number was only due to the displacement thickness of the boundary layer, then, from simple area ratios, the boundary layer reduces the exit area of the air nozzles from 0.5 in² to 0.34 in². The helium nozzle's exit area was effectively reduced from 0.2 in² to 0.16 in². In addition there are shock waves within the nozzles which can be seen in Figure III-5. These waves most likely originate at the location where the boundary layer transitions from laminar to turbulent (Fig. III-5, Point A). The transition location was assumed to be at the location where the expansion waves from the throat impinge on the nozzle walls. Measurements of the shock angles indicate that the shock waves were very weak approaching Mach waves. The measured shock angles ranged from 19 to 20 deg and are close to the Mach angle of 22.6 deg for a Mach 2.6 air stream.

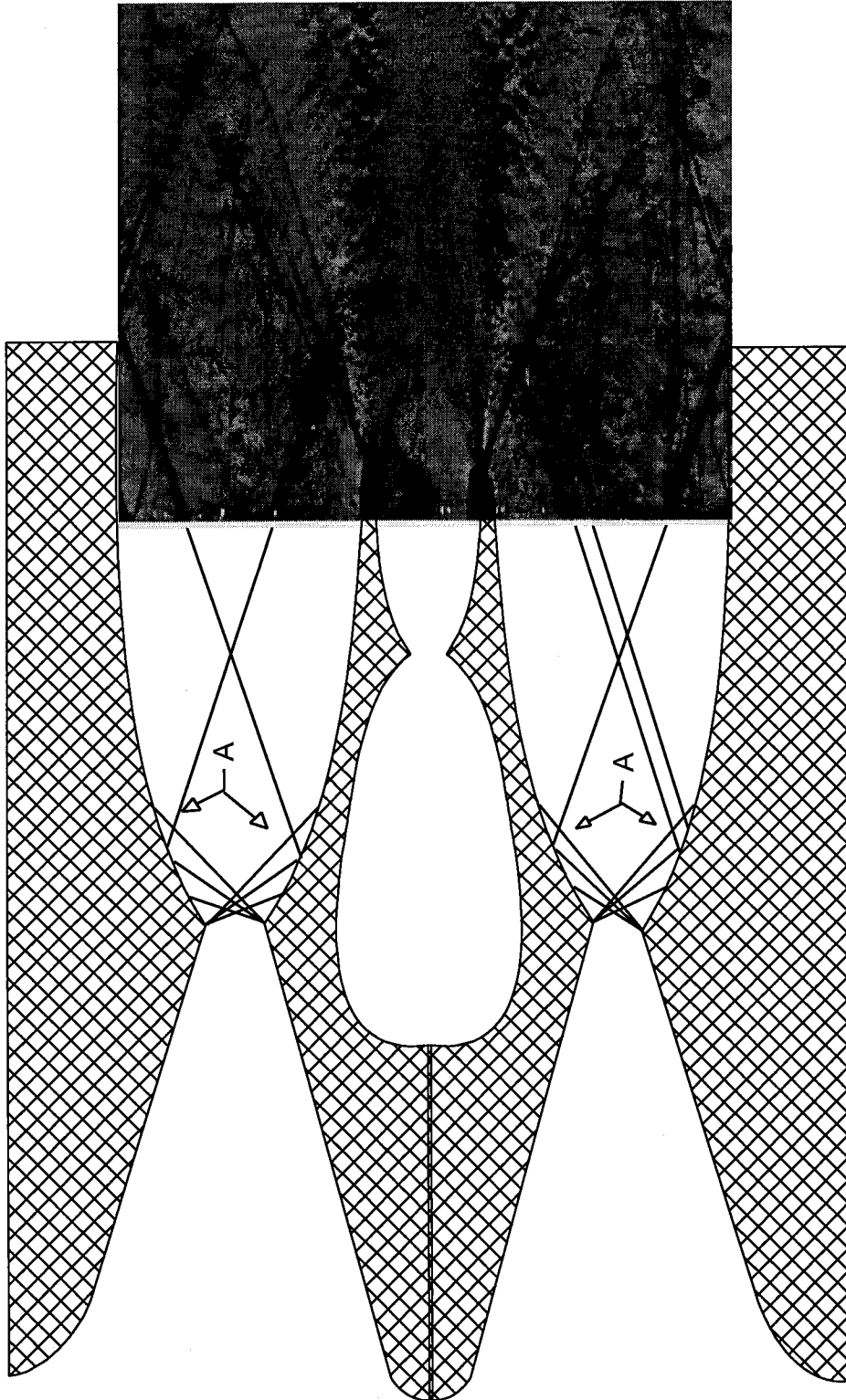


Figure III-5: Shocks within air nozzles

IV. Binary Gas Concentration Probe

IV.1. Background

In order to evaluate the mean concentration of helium in the jet, a probe was needed that was capable of measuring helium concentration profiles rapidly across supersonic streams with varying total pressures. The binary gas probes used by previous investigators and those commercially available were inadequate for this study but provided useful insight for the development of the present binary gas probe (52:54). All the previous concentration probes were designed for subsonic, low velocity flows where the total pressure did not change significantly. The probe used by Brown and Rebollo (52:649) was made from a glass tube drawn to a point with the tip ground and polished until a 0.0005 in diameter hole was formed. Downstream from the tip a Wollaston wire was placed in the glass tube and then etched to a 0.0005 in diameter. The gas mixture was drawn into the tip of the probe by attaching a vacuum source to the opposite end of the tube. The probe was calibrated for various helium/nitrogen concentrations and pressures and a family of curves was drawn. When the probe was used the pressure was known and the voltage needed to balance the hot wire gave the concentration directly. The pressure differential across the opening in the tip was great enough to choke the flow. The probe worked very well for Brown and Rebollo and was sensitive enough to record concentration fluctuations across the shear layer being investigated (52:650). The Brown and Rebollo probe worked well for flows with fixed total pressure but in this study the total pressure varied across the jet as well as downstream from the jet injection plane. The

probe described by Blackshear and Fingerson (53) and that available from Thermal Systems Incorporated (54) are very similar. Both are based on the flow through a choked orifice being independent of freestream velocity and dependent only on freestream total pressure, temperature and gas mixture. Both probes place a hot film sensor in front of the sonic orifice in a small duct where the cross-sectional area is fixed. Each probe is capable of measuring either temperature fluctuations or concentration fluctuations. The Blackshear and Fingerson probe was developed for high temperature flows and utilizes a water cooled hot film sensor. It was used in conditions where the Mach number was substantially constant and apparently subsonic. The TSI probe is advertised for use in flows where the velocity is <300 ft/s (54 & 55).

The probe developed for this investigation is similar to the Thermal Systems Incorporated probe but incorporates a pressure port and thermocouple in the cavity where the sonic orifice and hot wire are located. The pressure port and thermocouple provide the total pressure and total temperature measurements needed in the mass flow equation for a sonic orifice thus reducing the unknown to only the gas concentration. After the first probe was designed and built for this study a paper by Ng et al. (56) was published describing the development and use of a binary gas probe very similar to the one used in this study. The major difference was that Ng's probe did not incorporate a thermocouple in its design and the data reduction procedure consisted of a graph of concentration values plotted for various pressures, temperatures, and hot wire bridge voltages. The temperatures for Ng's calculations were determined by traversing the flow with a temperature probe during a separate test run.

IV.2. Theory

The mass flow through a sonic orifice is given by Shapiro (57:85)

as:

$$\dot{m} = \frac{P_0 A^*}{\sqrt{T_0}} \sqrt{\frac{\gamma_m}{R_m} \left(\frac{2}{\gamma_m + 1} \right)^{\frac{\gamma_m + 1}{\gamma_m - 1}}} \quad (\text{IV-1})$$

The total pressure (P_0) and total temperature (T_0) are measured quantities. The ratio of specific heats (γ_m) and the gas constant (R_m) are functions of the gas mixture, as given below.

$$\gamma_m = \frac{Cp_m}{Cv_m} \quad (\text{IV-2})$$

$$\begin{aligned} Cp_m &= X_{He} m_{He} Cp_{He} + (1 - X_{He}) m_{Air} Cp_{Air} \\ Cv_m &= X_{He} m_{He} Cv_{He} + (1 - X_{He}) m_{Air} Cv_{Air} \end{aligned} \quad (\text{IV-3})$$

$$R_m = \hat{R} (X_{He} m_{He} + (1 - X_{He}) m_{Air})^{-1} \quad (\text{IV-4})$$

When Equations IV-1 to IV-4 are combined, the molar concentration of helium (X_{He}) is a function of mass flow rate (\dot{m}), total pressure (P_0), total temperature (T_0), and the gas properties. The mass flow rate through the probe was measured using a hot wire sensor placed in front of the sonic orifice.

Hot wire anemometry is based on the heat transfer rate from a wire placed perpendicular to the mean flow being a function of the density, temperature, velocity and the gas transport properties; viscosity (μ), and thermal conductivity (k). The power needed to maintain the wire at constant temperature is equal to the rate of heat removal by the gas flowing across it and can be expressed as follows:

$$\text{POWER} = \dot{Q} = h(T_w - T_f) A_{\text{ref}} \quad (\text{IV-5})$$

where h is the convective heat transfer coefficient; T_w and T_f are the hot wire and fluid temperature respectively; A_{ref} is a reference area that is determined by the product of the length and diameter of the hot wire. The power is a function of the bridge voltage across the hot wire (V_w), the resistance of the hot wire sensor (R_w) and the resistance across the bridge (R_b).

$$\dot{Q} = \frac{V_w^2 R_w}{(R_w - R_b)^2} \quad (\text{IV-6})$$

The convective heat transfer coefficient is obtained from King's law for the average heat transfer rate from an infinite cylinder in cross flow and is expressed in the form of a Nusselt number as a function of Prandtl and Reynolds numbers.

$$\text{Nu} = (A + B \text{Re}^{\text{nr}}) \text{Pr}^{\text{np}} \quad (\text{IV-7})$$

A and B are calibration coefficients: nr and np are exponents that are ≈ 0.5 and 0.3 respectively. The Nusselt, Reynolds and Prandtl numbers in Equation IV-7 are determined as follows.

The Nusselt number is defined in Equation IV-8

$$\text{Nu} = \frac{h \cdot d_w}{k} \quad (\text{IV-8})$$

where h is the heat transfer coefficient, d_w is the diameter of the hot wire and k is the thermal conductivity. Combining Equations IV-5 and IV-6 and substituting the result into Equation IV-8 for the heat transfer coefficient, h , gives Equation IV-9.

$$\text{Nu} = \frac{V_w^2 \cdot R_w \cdot d_w}{(T_w - T_f) \cdot k \cdot A_{\text{ref}} \cdot (R_w - R_b)^2} \quad (\text{IV-9})$$

Equation IV-9 provides a means of calculating the Nusselt number in terms of measured quantities (T_f and V_w), design parameters (R_w , d_w , T_w , A_{ref} , and R_b), and gas property (k).

The Reynolds number and mass flow rate through the probe are defined in Equations IV-10 and IV-11

$$Re = \frac{\rho V \cdot d_w}{\mu} \quad (IV-10)$$

$$\dot{m} = \rho V A_{hw} \quad (IV-11)$$

where A_{hw} is the cross-sectional area of probe cavity where the hot wire is located and ρV is the mass flux across the hot wire used to calculate the Reynolds number for King's Law. Substituting ρV from Equation IV-11 into Equation IV-10 then substituting \dot{m} from Equation IV-1 yields Equation IV-12.

$$Re = \frac{\dot{m} \cdot d_w}{A_{hw} \cdot \mu} = \frac{d_w \cdot P_0 \cdot A^*}{A_{hw} \cdot \mu \cdot \sqrt{T_0}} \sqrt{\frac{\gamma_m}{R_m} \left(\frac{2}{\gamma_m + 1} \right)^{\frac{\gamma_m + 1}{\gamma_m - 1}}} \quad (IV-12)$$

Equation VI-12 provides a means of calculating the Reynolds number in terms of measured quantities (P_0 and T_0), design parameters (d_w , A^* and A_{hw}), and gas properties (μ , γ , and R).

The Prandtl number is defined by Equation IV-13 and is only a function of gas properties.

$$Pr = \frac{C_p \cdot \mu}{k} \quad (IV-13)$$

Equations IV-7, IV-9, IV-12, and IV-13 are the governing equations for the probe. Expressing these equations as functional relationships it becomes obvious that the

only unknown is the molar concentration of helium (X_{He}) because P_0 , T_0 , and V_w are measured quantities.

$$\text{Re} = \frac{P_0}{\sqrt{T_0}} f_1(X_{\text{He}}) \quad (\text{IV-14})$$

$$\text{Pr} = f_2(X_{\text{He}}) \quad (\text{IV-15})$$

$$\text{Nu} = V_w^2 f_3(X_{\text{He}}) \quad (\text{IV-16})$$

$$V_w^2 f_3(X_{\text{He}}) = \left(A + B \left(\frac{P_0}{\sqrt{T_0}} f_1(X_{\text{He}}) \right)^{\text{nr}} \right) (f_2(X_{\text{He}}))^{\text{np}} \quad (\text{IV-17})$$

Given the calibration coefficients A and B and exponents nr and np along with the measured quantities V_w , P_0 , and T_0 , Equation IV-17 can be solved for the molar concentration of helium (X_{He}) by trial and error using a digital computer.

The functions f_1 to f_3 are combinations of the transport properties of the unknown gas mixture along with fixed design parameters. Appendix A discusses the method used to determine the transport properties of the gas mixture.

IV.3. Probe Design

The probe was designed to have minimal impact on the flow, a rapid response time, and good spatial resolution. Figure IV-1 is a sketch of the probe showing the important features and parts. The inlet cap is removable to allow access to the hot wire for replacement purposes. The outside diameter of the probe was chosen to be 0.125 in to reduce the influence of the probe on the flowfield. This diameter caused only a 1 percent blockage of the flow duct where the measurements were being taken. With the outside diameter given the next step was to determine the diameters of the stagnation chamber,

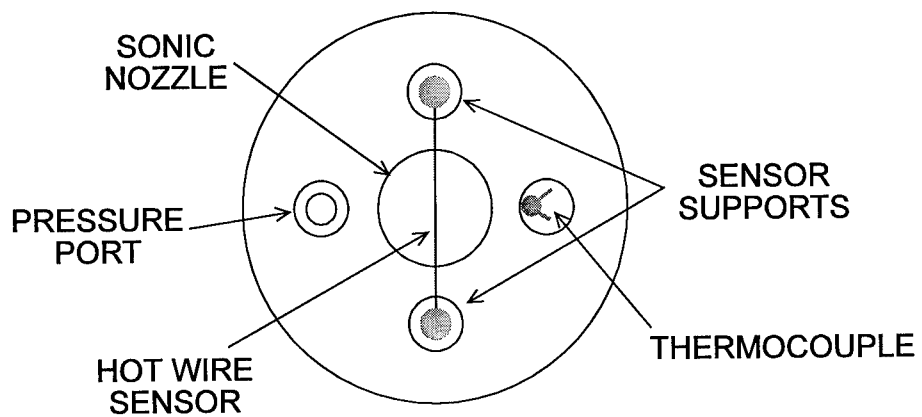
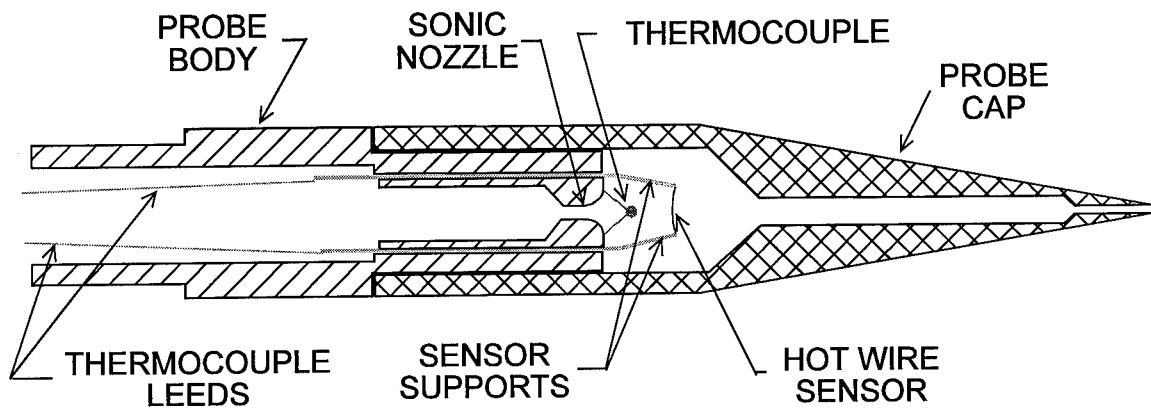


Figure IV-1: Schematic of concentration probe

sonic orifice and inlet. An inlet diameter of 0.013 in was used to give good spatial resolution. The diameter of the stagnation chamber was chosen to be 0.100 in in order to allow space to locate the thermocouple, pressure port and the two hot wire mounts. The only other diameter was the sonic orifice which governs the response time of the probe. The sonic orifice had to be larger than the inlet diameter so that the bow shock could be swallowed by the probe thus eliminating the effect of the shock on the concentration measurement. The sonic orifice also had to be large enough so that the gas in the stagnation chamber was changed fast enough to provide a good frequency response. The last requirement was that the sonic orifice be small enough to be drilled in the base of the stagnation chamber along with the pressure port, thermocouple, and hot wire mounts. The orifice diameter was chosen to be 0.020 in which provided a response time of 0.0004 s. This response time is short enough for continuous traverses to be made across the duct without significant loss of accuracy. The accuracy of the probe deteriorates if traverses are >32 in/s. The speed of the traverses in this study was <1 in/s, well within the probe's capability.

Within the probe there was a hot wire sensor, a thermocouple, and a pressure port to measure the quantities V_w , T_0 , and P_0 , respectively. The hot wire was mounted on two #10 sewing needles glued in place with epoxy cement to insulate them from the brass body of the probe. The hot wire itself was 0.0005 in tungsten wire spot welded to the mounts. The hot wire sensor leads were connected to a TSI intelligent flow analyzer (Model IFA-100) which controlled and measured the voltage applied to the hot wire sensor. The thermocouple was a type K (iron-constantan) with a bead diameter of 0.010 in attached to

an electronic ice point (Omega Corp. Model MCJ-K). The pressure port was 0.018 in diameter. The pressure port was attached to a pressure transducer (Endevco model 8515B) via 24 in of 0.030 in tubing.

IV.4. Calibration of Concentration Probe

The probe was custom made by the author therefore the internal resistance of the cables, supports and sensors were unknown and needed to be determined. The resistance of the cables were measured using the IFA-100 with a shorting plug on the end of the last BNC connector as described in the IFA-100 manual (58). The internal resistance of the probe was determined before the hot wire sensor was soldered to the prongs. This was accomplished by shorting across the prongs and measuring the resistance using an ohmmeter (HP model 3466A). The resistance of the probe and cables was then the sum of the two. Once the resistance of the cables and probe was determined it was entered into the IFA-100 as cable resistance. The hot wire sensor's thermal coefficient of resistance is usually supplied by the manufacturer of hot wire probes but because this probe was custom-made it needed to be determined in order to calculate the operating resistance. The coefficient was determined by attaching the probe to the cables and IFA-100 and inserting the tip of the probe into a glass flask through a rubber stopper. The flask was then heated, using a hot air heat gun, until the temperature on the probe's internal thermocouple reached 200 F. Once this temperature was reached the flask was wrapped in insulating cloths in order to keep the temperature from dropping rapidly. The resistance was measured with the IFA-100 as the temperature dropped (every 10° F) until the temperature reached room temperature. The resistance versus temperature was then

plotted and the coefficient of thermal resistance determined. The operating temperature of the probe was determined by applying an over-heat ratio of 1.5 and using the procedure described in the IFA-100 manual (58). The operating resistance of the hot wire was determined from the operating temperature and the measured coefficient of thermal resistance.

The calibration of the probe for various helium/air mixtures was accomplished in a small tank that could be evacuated and then filled with a known mixture of air and helium. The gas mixture was determined by filling the evacuated tank with a known pressure and temperature of air then adding helium and measuring the pressure and temperature of the mixture. The mixture concentration was then determined by the ratio of the pressures and temperatures.

$$\text{Molar concentration of air} = \left(\frac{P_{\text{air}}}{P_{\text{mixture}}} \right) \cdot \left(\frac{T_{\text{mixture}}}{T_{\text{air}}} \right) \quad (\text{IV-18})$$

The gases were assumed to be mixed during the injection process of the helium into the air through turbulent and molecular motion. Once the gas mixture was made it was then released into an evacuated pipe that forced it to pass through the probe. While the gas mixture was passing through the probe, the probe pressure (P_0), hot wire bridge voltage (V_w) and the probe total temperature (T_0) were being recorded simultaneously using the DL1200 data acquisition system. Each tank of gas mixture allowed two runs of 81 s before being emptied. The first run was at a higher pressure than the second run. Enough data from the two runs were collected to cover the entire range of pressures encountered during test in the blowdown facility. The temperature of the gas mixture could be

changed by either heating or cooling the calibration tank. This procedure provided calibration data for a wide range of pressures, temperatures and concentrations.

Once the calibration data were collected for various helium/air mixtures it was reduced into Nusselt, Reynolds, and Prandtl numbers using Equations IV-9, IV-12, and IV-13 respectively. The Reynolds, Prandtl and Nusselt numbers were then combined to form the following Equation and plotted to find the calibration constants.

$$\frac{\text{Nu} \left(1 + \frac{T_w}{T_f} \right)^{nt}}{T1} \frac{\text{Pr}^{-np} (1 + X_{\text{He}})^{-(nc \cdot \text{Re} - nc1)}}{T2} = \frac{(A + B \cdot \text{Re}^{nr})}{T3} \quad (\text{IV-19})$$

Equation IV-19 has seven calibration constants to be determined, five are exponent type constants nt, nr, np, nc and nc1 which are determined by repeated trials. The remaining two constants, A and B are determined by a least square curve fit. In practice the left side of IV-19 was curve fitted to a polynomial in powers of (Re^{nr}) in order to get a more accurate calibration curve.

$$\text{LEFT SIDE OF IV-19} = A + B(\text{Re}^{nr})^1 + C(\text{Re}^{nr})^2 + D(\text{Re}^{nr})^3 \quad (\text{IV-20})$$

Figure IV-2 is an example calibration for one of the concentration probes used in this study.

Equations IV-19 and IV-20 were formulated during the initial calibration of the concentration probe. It was found experimentally that King's law (Eq. IV-7) was not adequate for multi-gas mixtures. King's Law was valid for any single gas mixture of helium and air but would not collapse the entire range of helium and air mixtures

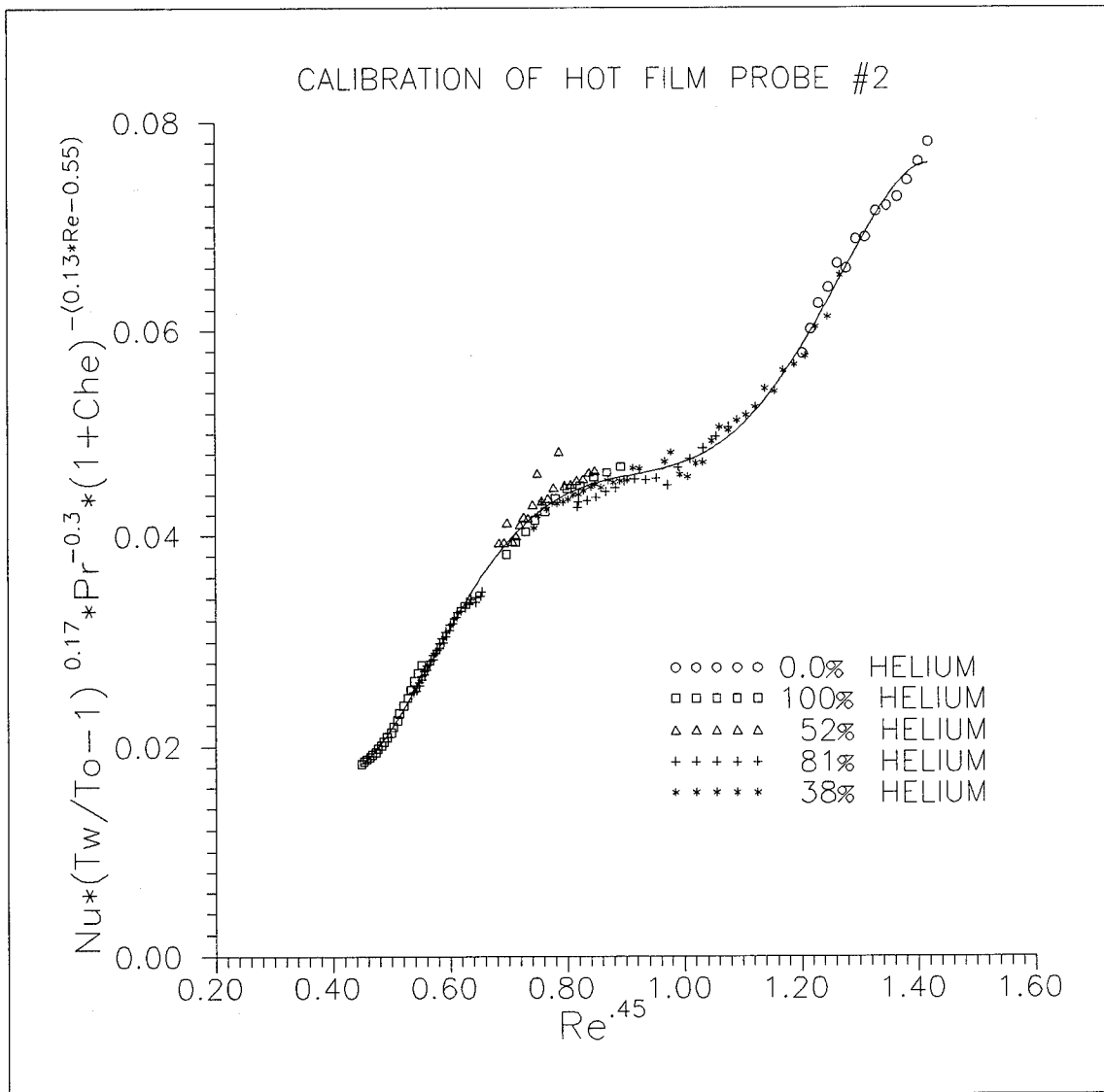


Figure IV-2: Example concentration probe calibration curve

($X_{he} = 0$ to 1). The explicit concentration term, term T2 in Equation IV-19, was added initially with a fixed exponent but it was found to vary across the range of Reynolds numbers encountered in this study. The solution was to give the exponent a linear dependence which was found to be adequate for this investigation. The physical significance of the concentration term was not investigated in this study but would be a good follow on project.

The temperature term, term T1 Equation IV-19, was added to account for temperature variations within the probe stagnation chamber. The temperature term was found to have little effect on the performance of the probe for the temperatures encountered in this investigation. The exponent values in Equation IV-19 varied depending on the type of wire used and the particular probe used but were generally close to the following (min-max value): $n_t = 0.17$ (0-0.17), $n_r = 0.45$ (0.45-0.45), $n_p = 0.3$ (0.3-0.3), $n_c = 0.13$ (0.13-2), $n_{c1} = 0.55$ (0.55-0.9). The primary values presented are the values that occurred most often during calibrations while the min-max values show the variations that occurred. The coefficients for the polynomial fits varied considerably from sensor to sensor thus none are given.

The repeatability of the concentration probe was good with most variations less than 0.05 molar fraction as can be seen in Figure IV-3. There were some problems with the probe measuring accurately near shocks where there are large pressure gradients as can be seen in Figure IV-3 near ± 1.5 Y/H. The probe's repeatability in the shear layer and the jet was very good, generally much less than the 0.05 molar fraction.

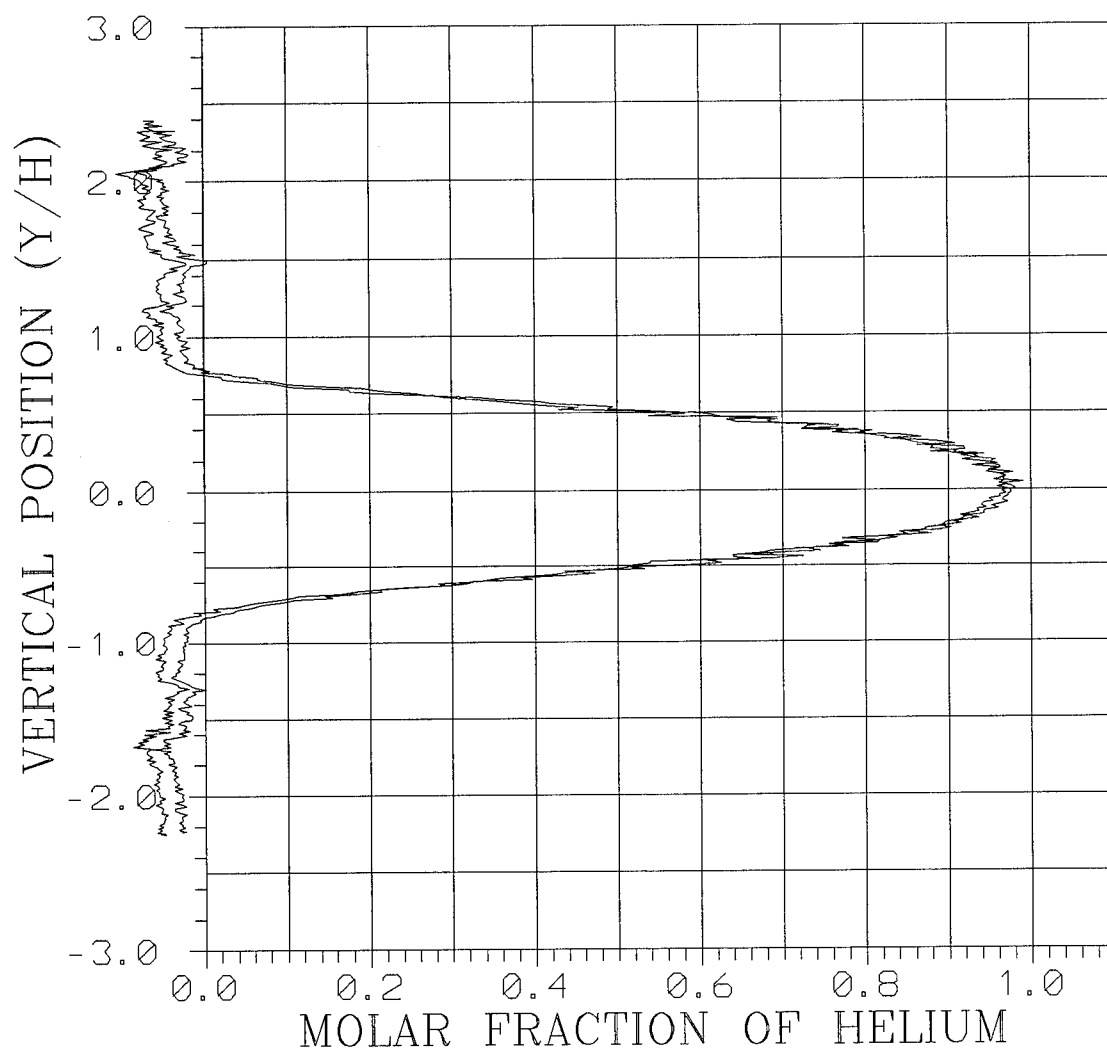


Figure IV-3: Repeatability of concentration probe

IV.5. Data Reduction

The data collected from the probe consisted of a pressure, temperature, and hot wire voltage. In order to reduce these data into a molar concentration of helium the following procedure was followed:

1. Make an initial estimate of the molar concentration of helium.
2. Calculate the gas properties of the mixture (γ_m , R_m , k , μ , ρ) using the assumed molar concentration of helium.
3. Calculate the power into the hot wire using Equation IV-6.
4. Calculate the Nusselt, Reynolds and Prandtl numbers using Equations IV-9, IV-12 and IV-13 respectively.
5. Calculate the right and left sides of Equation IV-20 and see if they are equal.
6. If the right (left) side is larger than the left (right) side then the guess is too high (low), select a lower (higher) molar concentration of helium and repeat steps 2 through 5.

The above procedure was programmed on a Zenith 386 personal computer in order to automate the procedure. A bisection routine was used to speed up the convergence to the appropriate helium concentration from the initial estimate. The entire procedure required 1 to 2 s to run at each data point.

V. Flowfield Results

The flowfield of each exit pressure ratio tested is discussed in order to give a clear picture of the flow within the mixing duct. A correlation between centerline helium concentration and axial distance is developed that reduces all three EPRs into a universal equation. This chapter also discusses the increase in jet width due to SSLIs. The mass entrainment rates, calculated from the data acquired using the binary gas concentration probe, and a correlation developed to relate the enhancement in mass entrainment rates with the strength of the SSLI are presented in Chapter VI. In Chapter VII this new correlation is used to develop a simple model that can be applied to the analysis of mass entrainment in SCRAMJET combustors. This new model predicts the entrainment between the fuel and air for fuel injectors operating at high exit pressure with SSLIs. Previous models have not accounted for the effects of large EPRs and SSLIs on mass entrainment.

V.1. Mixing Duct Flowfield

The flow parameters for each of the three pressure ratios tested are given in Table I-1 in order of increasing EPR; repeated here for convenience. The desired EPR was obtained by a combination of reducing the air exit pressure and increasing the helium exit pressure as seen in Table I-1. The three cases tested represent theoretical cases II and III. The attempt to achieve the conditions for theoretical case I ($EPR=1$) resulted in achieving an EPR of 0.89 which is case II. The next section will show that the flowfield

for an $EPR=1$ and that achieved with an $EPR=0.89$ are similar and therefore $EPR 0.89$ will act as the baseline case for this study.

Table I-1: Test Conditions

EPR	Air (Average)			Helium			Mass Flow		
	Pe	Me	Ve	Pe	Me	Ve	He	Air	Total
	psia		ft/sec	psia		ft/sec	lbm/sec		
0.89	3.18	2.61	1918	2.84	1.67	3983	1.019	0.416	0.435
1.49	2.69	2.60	1911	3.99	1.61	3913	0.027	0.338	0.365
3.50	2.30	2.58	1906	8.04	1.60	3889	0.051	0.290	0.341

Pe - Static pressure at nozzle exit plane

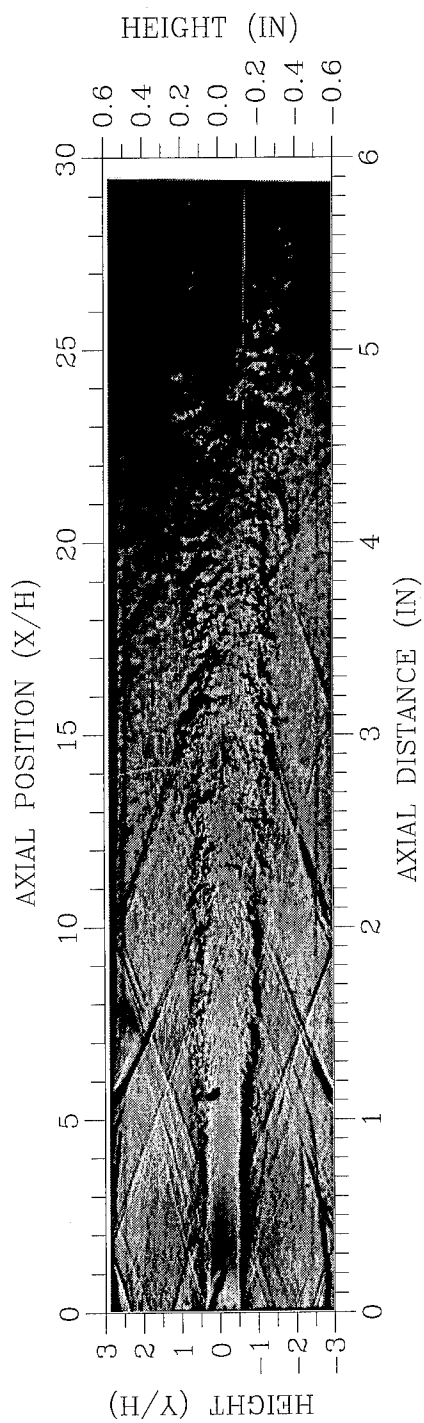
Me - Mach number at nozzle exit plane

Ve - Velocity at nozzle exit plane

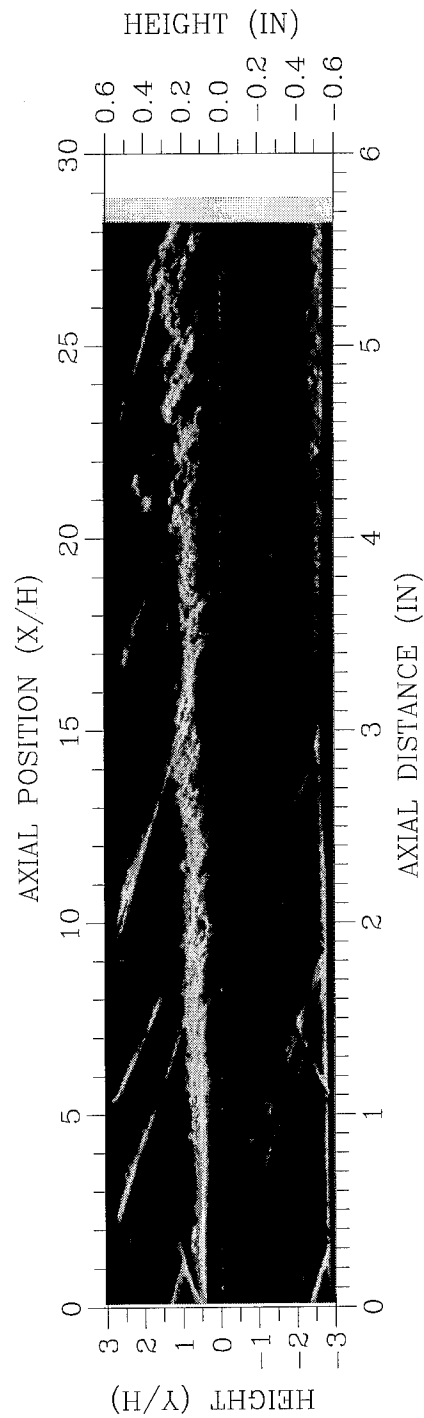
V.1.1. Exit Pressure Ratio 0.89

$EPR 0.89$ represents theoretical case II but since it requires <1 degree of turning to equalize the exit pressures it also approximates theoretical case I. This pressure ratio will be used as the baseline for evaluating the effect of large EPR s on jet mixing and decay.

The schlieren photographs of $EPR 0.89$ are presented in Figure V-1 for both horizontal (parallel) and vertical (perpendicular) knife edges. The horizontal knife accentuates lateral density gradients in the flowfield, in particular the density gradients across the shear layers while the vertical knife edge accentuates axial density gradients, emphasizing the large structures within the shear layer. Together the two schlieren photos give a good representation of the density gradients within the flowfield. The flowfield for this pressure ratio exhibits a multitude of waves not accounted for in the simple theory presented in Chapter II. The schlieren photographs show waves emanating from the



a) Perpendicular knife edge



b) Parallel knife edge

Figure V-1: Schlieren photographs of EPR 0.89

mixing region which coalesce and reflect off the walls. These waves are weak shocks or Mach waves generated by the large structures within the shear layers along the edges of the helium jet. These pressure waves in free shear layers and jets normally propagate out to infinity but in confined jets they reflect off the walls and back into the jet. The effect of these waves on mixing will be discussed in detail later in Chapter VI. The schlieren photographs show the two shear layers that are formed between the helium jet and the air streams growing until they merge at 1.5-2.0 in (7.5-10 X/H) downstream from the exit plane of the nozzle. The photographs also clearly show large structures within the shear layer that are similar to those observed by Papamoschou in supersonic flow (24) and Brown and Roshko in subsonic flows (26). The structures appear to be roughly elliptical with their major axis tilted 45 deg to the vertical axis. The slope of the structures is due to the helium within the central jet traveling faster than the air in the outer stream; thus the portion of the structure in the helium jet is pushed further downstream than the portion of the structure within the air stream, this causes the structure to elongate and tilt (Fig. V-2). The structures in each shear layer appear to be independent of each other until 3 in (15 X/H) downstream when they begin to merge and interact with each other. At 4 in (20 X/H) downstream the large structures within the two shear layer appear to have completely merged and only one large structure pattern is evident.

Analysis of the schlieren photographs shows the visual growth rate of the helium jet to be linear and growing at a rate of 0.05 to 0.07 in laterally per in axially (in/in). The linear growth of the jet can also be seen in the contour plots of helium molar fraction, Figure V-3a, which shows the jet growing at 0.04 in/in. The contour plot was made from

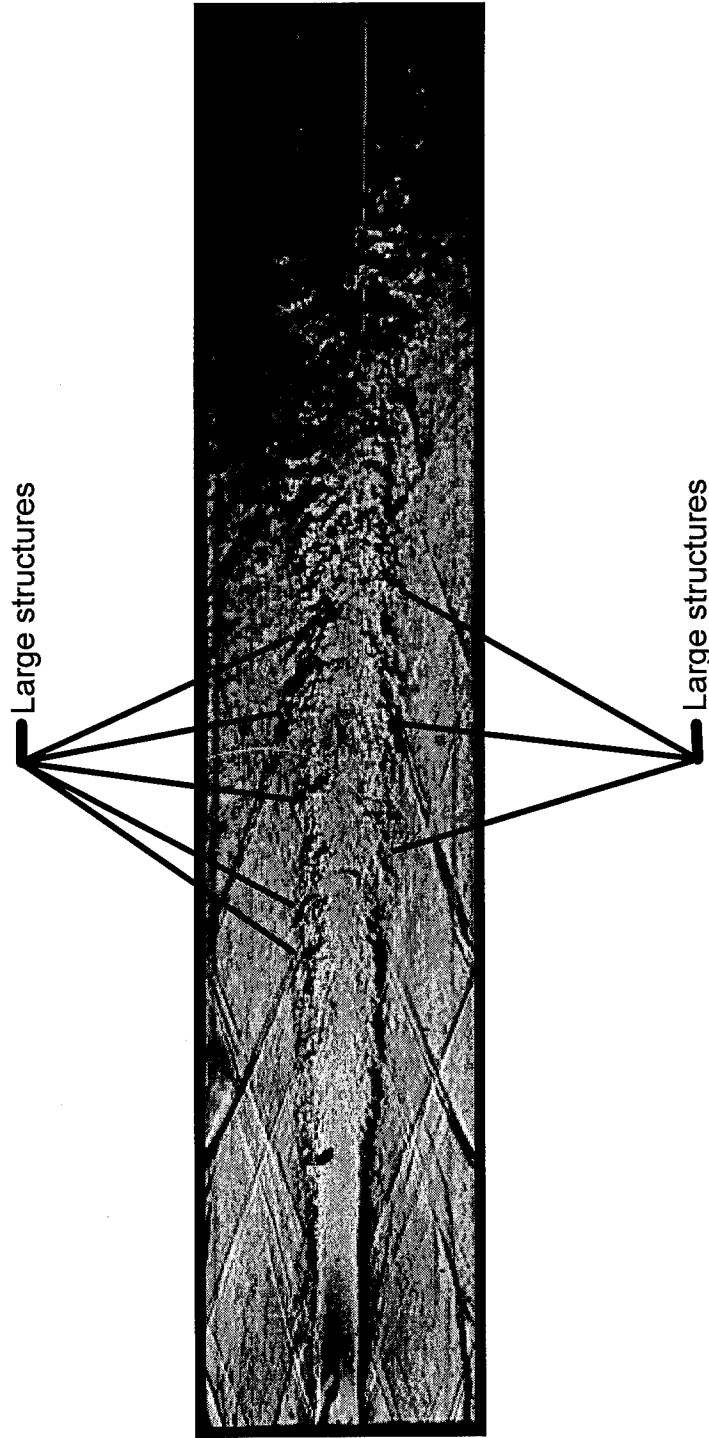
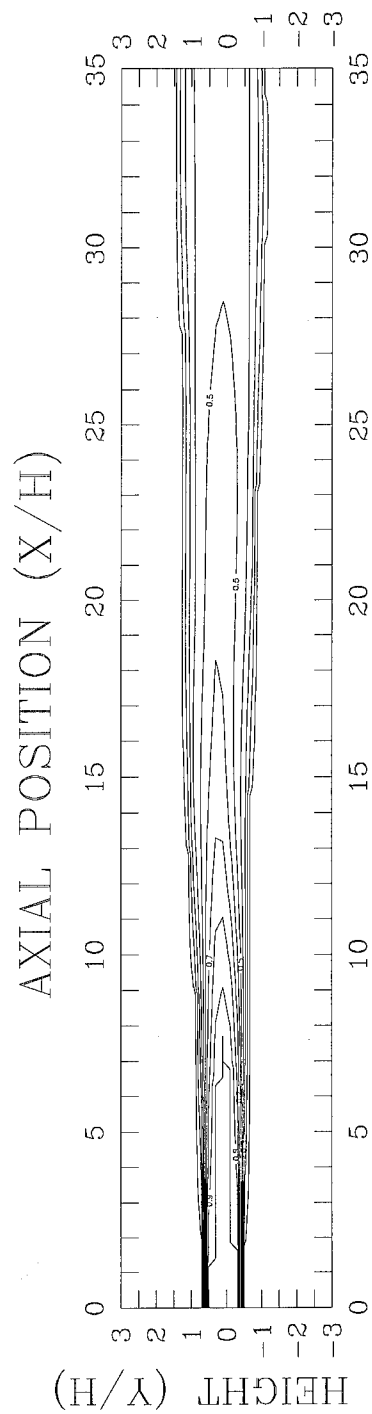
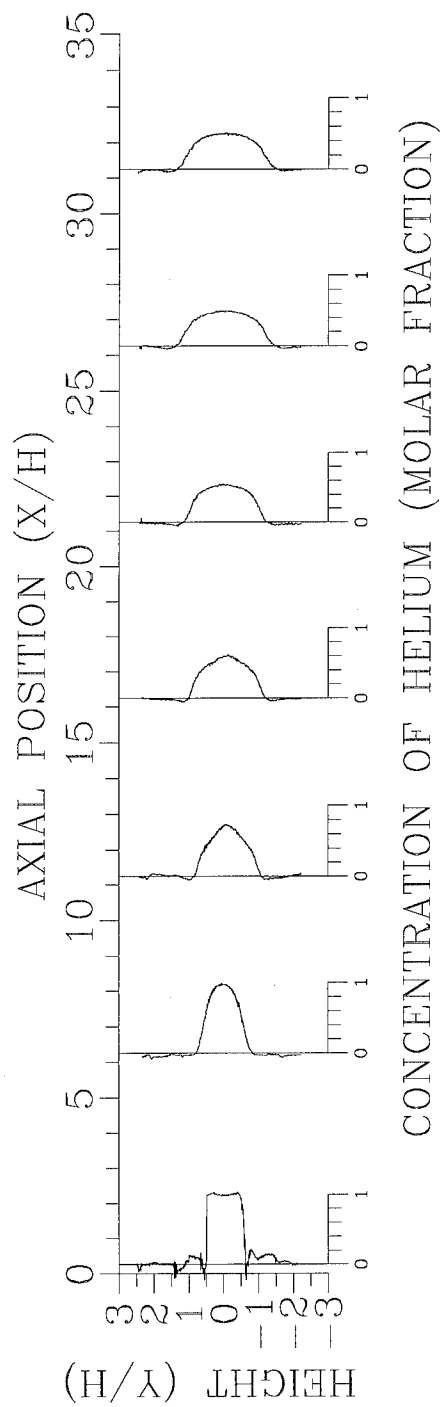


Figure V-2: Large structures within shear layer



a) Molar fraction contour plot



b) Molar fraction composite profile plot

Figure V-3: Concentration plots for EPR 0.89

the data measured at various axial locations. The concentration data used to develop the contour plots are presented in Figure V-3b. The visual growth rates of the two shear layers before they begin to merge at 3 in (15 X/H) are 0.06 in/in as measured from the schlieren photos. The concentration contour plot shows the shear layers growing at 0.04-0.05 in/in due to turbulent and molecular diffusion of helium into the air. Papamoschou found the pitot pressure growth rates for shear layers with conditions that bound those in this study to vary between 0.023 and 0.069 in/in (24:44). Papamoschou indicated that when pressure discontinuities are present in the test section, as in this study, the shear layer thickness increased by as much as 25 percent over similar shear layers without pressure discontinuities (24:39). The data in this study falls within the range reported by Papamoschou thus the data is consistent with the published data. The visual and diffusion growth rates of the shear layers are basically the same as the jet's visual and diffusion growth rates which was expected for case I jets. The average growth rates for EPR 0.89 calculated from both the shear layer measurements and the jet measurements are 0.06 in/in for the visual growth rate and 0.05 in/in for the concentration (diffusion) growth rate. A difference between the visual and concentration growth rates is to be expected because the visual growth rate is based on the density gradients which are affected by both the helium concentration and the pressure while the concentration growth rate is based solely on the helium concentration. The visual growth rate represents the growth of the density gradient; the concentration growth rate represents both the turbulent and molecular diffusion of the helium.

Figure V-4 shows the side wall static pressures measured along the duct centerline and ± 0.35 in from the duct centerline, corresponding to the centerlines of the upper and lower air nozzles. The static pressures show the effects of the EPR as predicted qualitatively by the EPR theory for case II. The centerline pressure increases and the outer air stream pressure drops due to the shocks and the expansion waves generated to balance the exit pressures of the helium and air nozzles. The static pressure increases along the duct, as is expected for a constant area diffuser, due to the numerous weak shocks and the increase in entropy caused by the mixing and turbulence.

V.1.2. Exit Pressure Ratio 1.49

EPR 1.49 represents theoretical case III. Because the EPR is greater than unity the helium jet will expand immediately after exiting the center nozzle. The theory presented in Chapter II predicts a shock forming in the upper and lower air jets and two P-M expansions occurring in the central helium jet, one from each side. These gasdynamic effects cause the two shear layers to turn outward as seen in the schlieren photographs (Fig. V-5) and the helium molar fraction contour plot (Fig. V-6a). The theoretical turning angle required to balance the pressure between the helium and air streams is 3 deg (See Appendix B for example calculation). The schlieren photographs show that the upper and lower shear layers turned outward 4 ± 1 and 6 ± 1 deg respectively (Fig V-7). The contour plots show the shear layers turning outward between 4 to 6 deg (Fig V-6a). The EPR theory predicts the angle of the shock needed to turn the air stream 3 degrees, thus balancing the pressure across the shear layer, is 24.8 deg. The angles measured from the schlieren photos are 22 ± 1 and 21 ± 1 degrees for the shocks in the upper and lower air

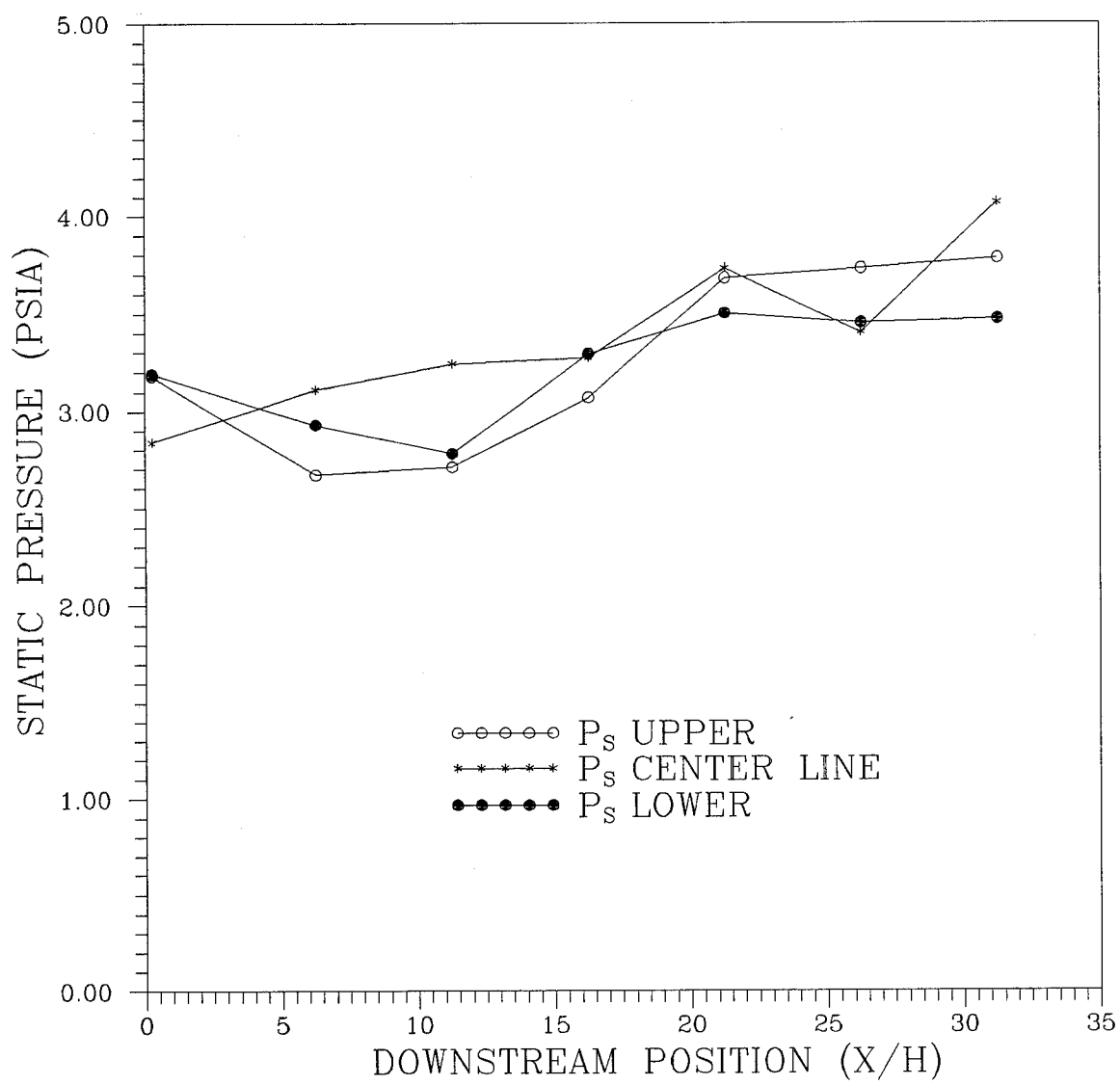
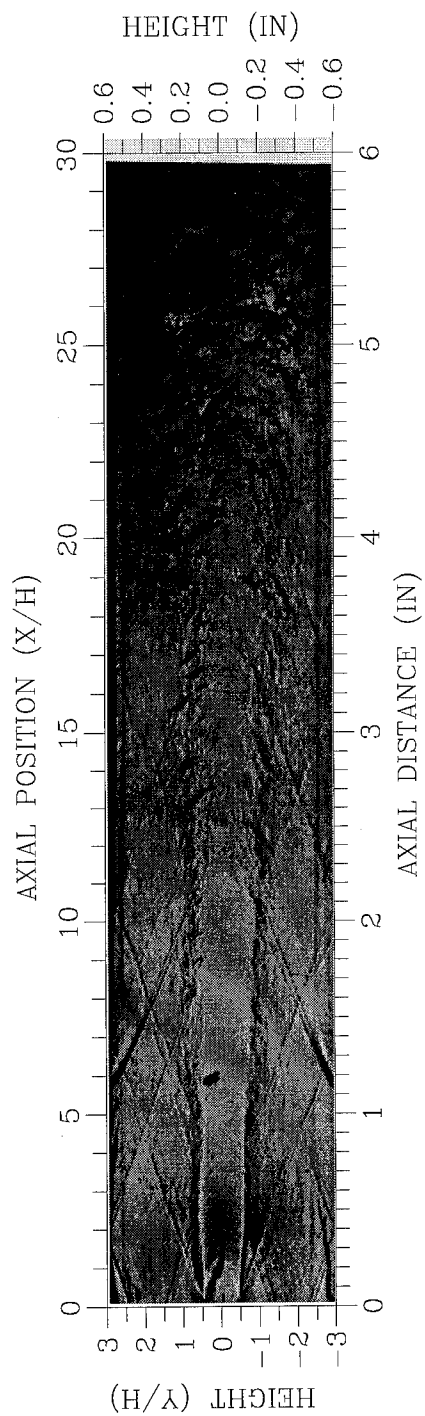
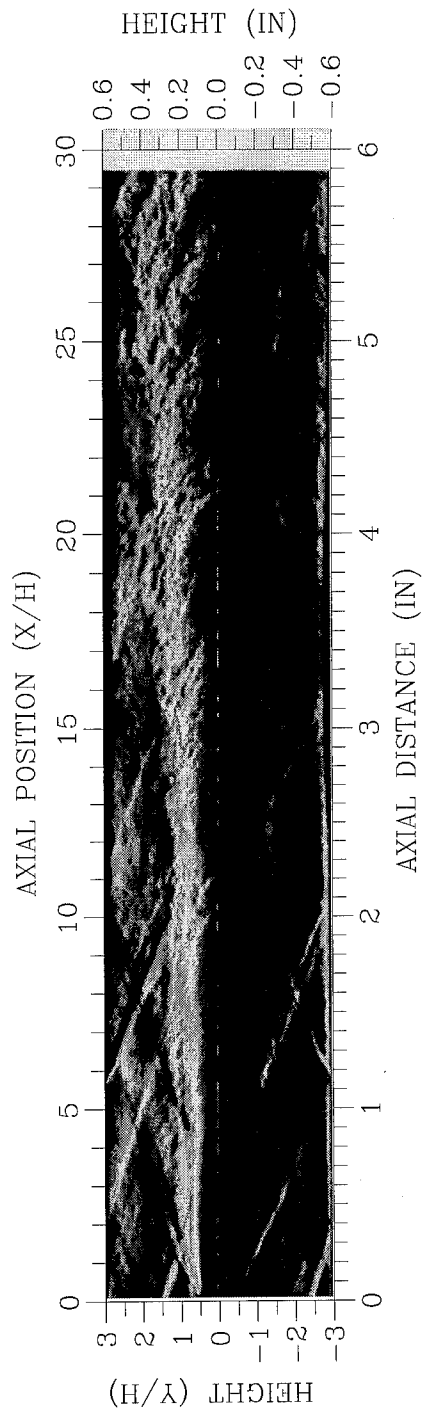


Figure V-4: Side wall static pressure for EPR 0.89

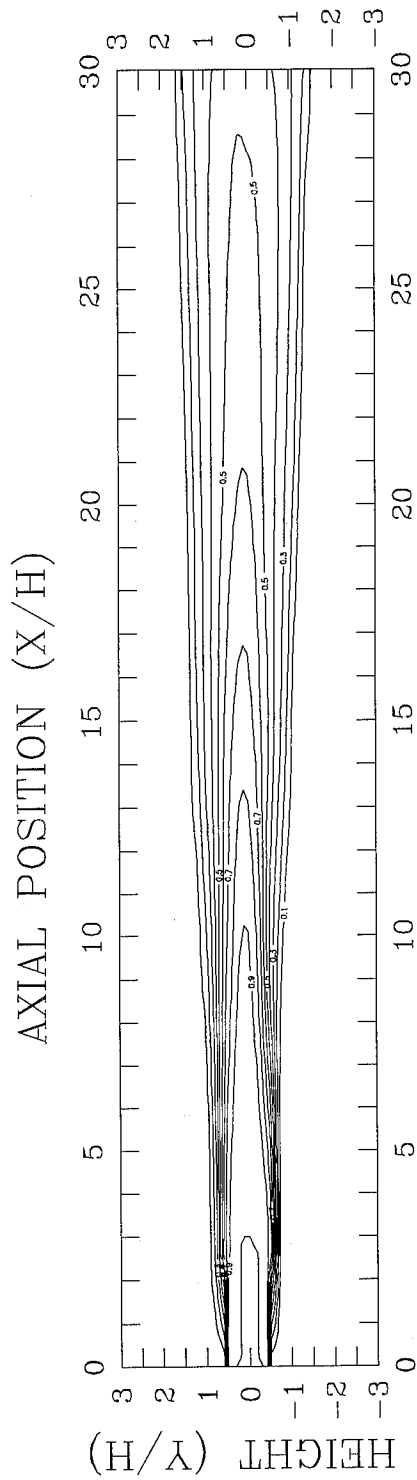


a) Perpendicular knife edge

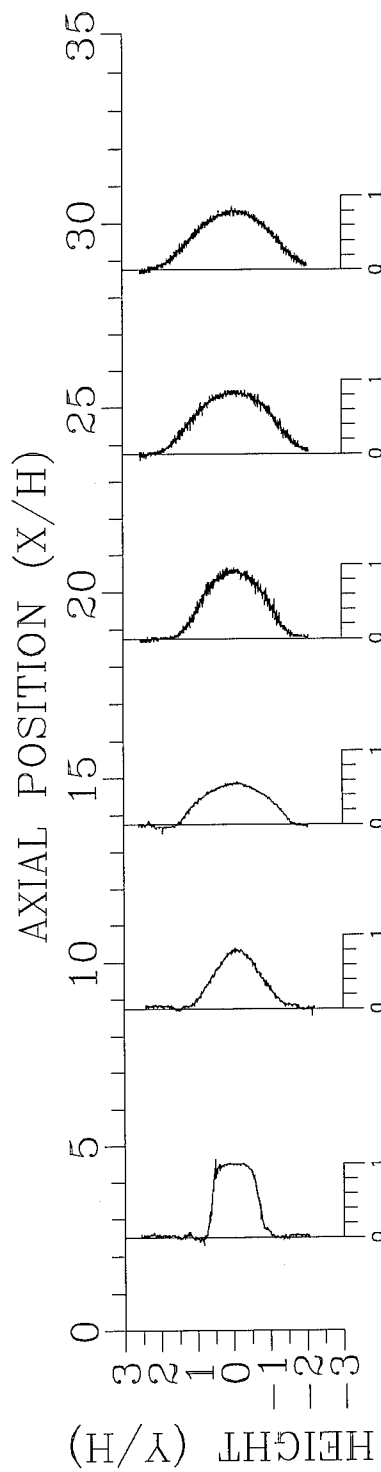


b) Parallel knife edge

Figure V-5: Schlieren photographs of EPR 1.49



a) Molar fraction contour plot



b) Molar fraction composite profile plot

Figure V-6: Concentration plots for EPR 1.49

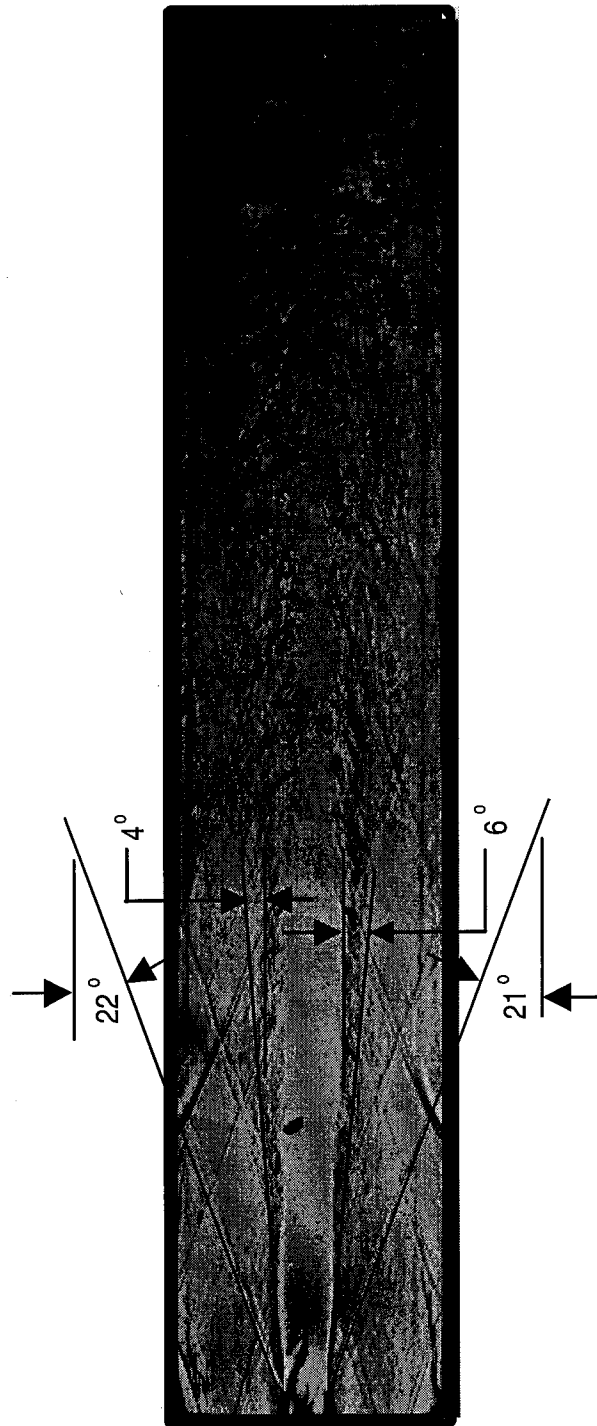


Figure V-7: EPR 1.49 shear layer and shock angles

streams, respectively (Fig. V-7). The P-M expansions within the helium jet can also be seen in the schlieren photographs but they are not well defined thus no attempt to measure their angles was attempted. The shock and shear layer angles measured from the schlieren photographs and the contour plots agree remarkably well with the theory considering the theory did not take into account any boundary layer or nozzle base effects, both of which are present in the experimental data.

The side wall static pressures indicate the large effect of the expansion fans within the helium jet to equalize the exit pressures (Fig. V-8). The centerline static pressure drops rapidly, below the air static pressure, then recovers to near the air static pressure. After the initial pressure equalization the duct static pressure rises downstream as expected for a constant area diffuser.

Examination of the flow downstream from the initial expansion region ($X/H > 3$) shows the shear layers turning towards the centerline and proceeding axially downstream (Fig. V-5). The shocks reflect off the side walls and interact with the helium jet 2.25 in (11.25 X/H) downstream from the exit plane of the nozzles. The shocks are not as clearly defined in the schlieren photographs after they reflect off the walls, and appear to be weak when they intersect the jet downstream. Both the schlieren photographs and the helium contour plot show the helium jet growing linearly with axial distance until about 2.5 in (12.5 X/H) from the exit plane, near the point where the shocks intersect the jet. Between 2.5 and 3.5 in (12.5 to 17.5 X/H) the jet expands and the two shear layers merge. Beyond 3.5 in (17.5 X/H) the helium jet appears to grow linearly again but the outer boundary is poorly defined and the jet appears very turbulent. The growth rates measured from the

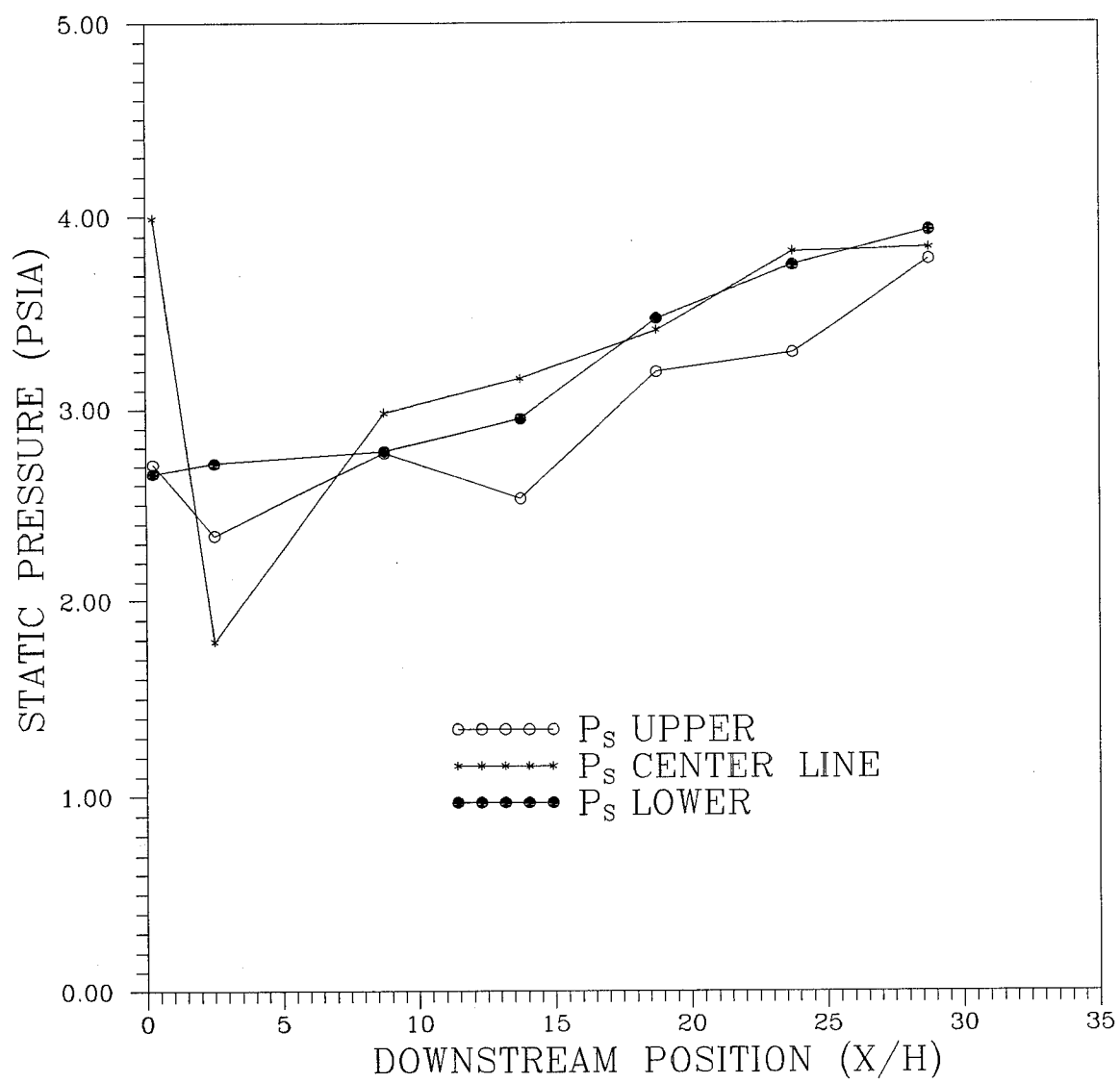


Figure V-8: Side wall static pressure for EPR 1.49

schlieren photographs indicate that the jet grows at 0.06 in/in from 0.6 to 2.5 in (3 to 12.5 X/H) from the nozzle exit plane. At 2.5 in (12.5 X/H) the jet expands rapidly then settles down to a growth rate of 0.06 in/in from 3.5 in (17.5 X/H) until the end of the duct. The contour plot of helium molar fraction shows similar growth rates. Between 0.5 to 2.0 in (2.5 to 10 X/H) downstream the jet grows at 0.03 in/in. Between 2.0 and 2.5 in (10 to 12.5 X/H) downstream the jet grows at 0.16 in/in; beyond 2.5 in (12.5 X/H) downstream the jet grows at 0.02 in/in. The rapid change in growth rate that occurred where the shocks intersected the shear layer is not predicted or accounted for in the EPR theory presented in Section II.1, but is hypothesized by the SSLI theory presented in Section II.2. The large visual and concentration growth rates observed around 12 X/H are caused by the SSLI taking place at that location. The shock, formed from the mismatch in helium and air exit pressures, reflects off the wall and intersects the jet in the region where the jet grows at an accelerated rate. The SSLI theory presented in Section II.2 showed that vorticity is generated in the SSLI region which causes fluid from the freestream to be rapidly entrained into the shear layers. The additional fluid entrained into the shear layer causes the shear layer growth rate to increase significantly in the vicinity of the SSLI.

The SSLI theory indicated that the generation of vorticity was due to the mismatch of the pressure and density gradients through the cross product of the two gradients. The relative vorticity generated for the SSLI in EPR 1.49 was determined from the source term of Equation II-1 using the procedure outlined in Appendix C. The following details the calculation of the relative vorticity generated at $X/H=11.25$.

CALCULATIONS FOR SSLI AT X/H=11.25

1. Calculate the pressure gradient ∇P :

The pressure across the shock was determined from the shock strength which was determined from the upstream Mach number and the shock angle. A Mach wave angle upstream of the oblique shock, that intersected the shear layer at 11.25 X/H, was measured to be 22° and the upstream Mach number (M_1) was calculated to be 2.7. The oblique shock has an angle (Θ_{shock}) to the flow direction of 23° .

If $\Theta_{\text{shock}} = 23^\circ$ and $M_1 = 2.7$ then $\delta = 3^\circ$ and $\frac{P_2 - P_1}{1/2 \gamma M_1^2} = 0.05$ from NACA

Report No. 1135 (59) compressible flow tables. Using $\gamma=1.4$ and $M_1 = 2.7$ gives:

$$\frac{P_2}{P_1} = 0.05 \left(\frac{1}{P_1} \right) (1/2 \gamma M_1^2) + 1 = 1.25$$

The upstream static pressure (P_1) was measured to be 2.3 psia therefore $P_2 = 2.9$ psia. The shock thickness (ΔX_{shock}) was calculated using the following equation from Shapiro (56:133) for weak shocks

$$\frac{\rho_x C_x \Delta X_{\text{shock}}}{\mu_x} = \frac{4}{\gamma + 1} \left(\frac{4}{3} + \frac{\gamma - 1}{Pr^*} \right) \frac{1}{M_x^* - 1}$$

where ρ_x , C_x , and μ_x are the density, speed of sound and viscosity upstream from the shock and ΔX_{shock} is the shock thickness. Pr^* is the Prandtl number at conditions where the Mach number is unity and was taken to be that of air (0.75). M_x^* is the normal component of the Mach number, relative to the oblique shock, evaluated upstream of the shock and using the speed of sound at $M=1$.

$$M_x = M_1 \sin (\Theta_{\text{shock}})$$

$$M_x = 2.7 \sin (23)$$

$$M_x = 1.05 \quad \Rightarrow \quad M_x^* = 1.04 \quad \text{from NACA Report No. (59)}$$

compressible flow tables. The upstream speed of sound, density, and viscosity were calculated from measured temperatures and pressures.

$$C_x = 810 \frac{\text{ft}}{\text{s}} \quad \rho_x = 0.03 \frac{\text{lbm}}{\text{ft}^3} \quad \mu_x = 5.59 \times 10^{-6} \frac{\text{lbm}}{\text{ft} \cdot \text{s}}$$

The shock thickness can now be calculated

$$\Delta X_{\text{shock}} = \frac{\mu_x}{\rho_x C_x} \frac{4}{\gamma + 1} \left(\frac{4}{3} + \frac{\gamma - 1}{\text{Pr}^*} \right) \frac{1}{M_x^* - 1}$$

$$\Delta X_{\text{shock}} = \frac{(5.59 \times 10^{-6} \frac{\text{lbm}}{\text{ft} \cdot \text{s}})(12 \frac{\text{in}}{\text{ft}})}{(0.03 \frac{\text{lbm}}{\text{ft}^3})(810 \frac{\text{ft}}{\text{s}})} \frac{4}{1.4 + 1} \left(\frac{4}{3} + \frac{1.4 - 1}{.75} \right) \frac{1}{1.04 - 1}$$

$$\Delta X_{\text{shock}} = 2.147 \times 10^{-4} \text{ in}$$

The pressure gradient is then calculated.

$$\nabla P = \frac{P_2 - P_1}{\Delta X_{\text{shock}}} = \frac{2.9 - 2.3 \frac{\text{lbf}}{\text{in}^2}}{2.15 \times 10^{-7} \text{ in}} = 2794 \frac{\text{lbf}}{\text{in}^3}$$

2. Determine shear layer density gradient $\nabla \rho_{\text{sl}}$:

The shear layer thickness (ΔX_{SL}) at the interaction point was measured to be 0.15

in. The density in the air stream (ρ_{air}) was calculated to be $0.03 \frac{\text{lbm}}{\text{ft}^3}$ and the

density on the jet centerline (ρ_{CL}) was calculated to be $0.007 \frac{\text{lbm}}{\text{ft}^3}$. The density

gradient is then calculated to be:

$$\nabla \rho = \frac{\rho_{\text{Air}} - \rho_{\text{CL}}}{\Delta X_{\text{SL}}} = \frac{0.03 - 0.007 \left(\frac{\text{lbm}}{\text{ft}^3} \right)}{0.15 \text{ in}} = 0.15 \left(\frac{\text{lbm}}{\text{ft}^3 - \text{in}} \right)$$

3. Determine average shear layer density $\bar{\rho}_{\text{sl}}$:

$$\bar{\rho}_{\text{sl}} = \frac{\rho_{\text{Air}} + \rho_{\text{CL}}}{2} = \frac{0.03 + 0.007 \left(\frac{\text{lbm}}{\text{ft}^3} \right)}{2} = 0.018 \left(\frac{\text{lbm}}{\text{ft}^3} \right)$$

4. Angle between pressure and density gradients:

The angle between the pressure and density gradients (Θ) at $X/H=11.25$, the

location of the SSL, was measured from the schlieren photographs to be 23° .

5. Calculate relative vorticity from the source term in Equation II-1:

$$\text{RELATIVE VORTICITY}(\bar{\zeta}) = \frac{\nabla P \times \nabla \rho_{\text{sl}}}{(\bar{\rho}_{\text{sl}})^2} \sin \Theta$$

$$\text{RELATIVE VORTICITY}(\bar{\zeta}) = \frac{\left(2794 \frac{\text{lbf}}{\text{in}^3} \right) \left(0.15 \frac{\text{lbm}}{\text{ft}^3 - \text{in}} \right)}{\left(0.018 \frac{\text{lbm}}{\text{ft}^3} \right)^2} \sin(23^\circ) \left(32.2 \frac{\text{lbf-ft}}{\text{lbf-s}^2} \right) \left(12 \frac{\text{in}}{\text{ft}} \right)^4$$

$$\text{RELATIVE VORTICITY}(\bar{\zeta}) = 3.45 \times 10^{11} \text{ } 1/\text{s}^2$$

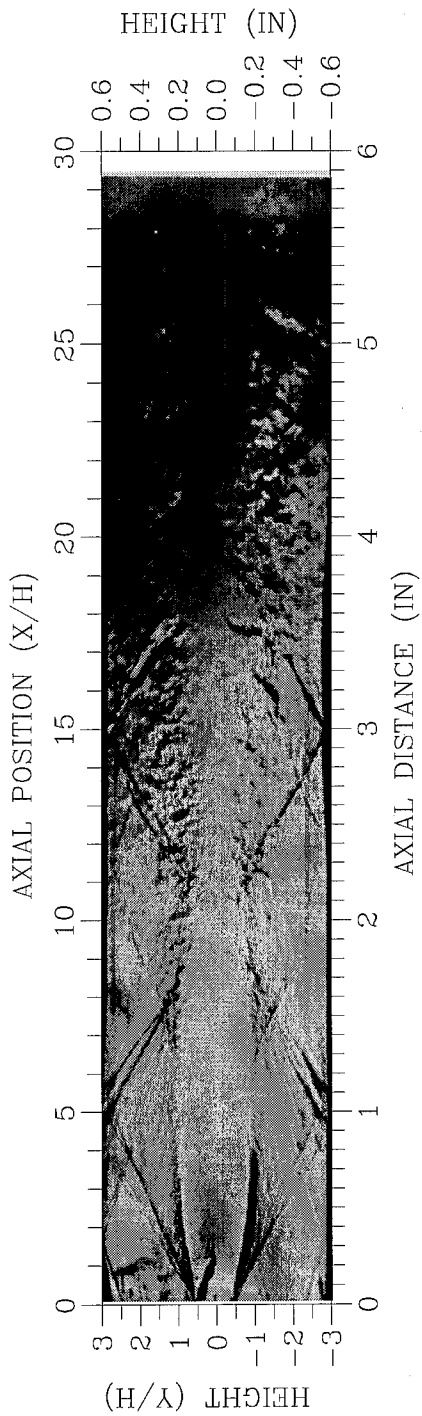
The above calculations show that the relative vorticity generated for the SSLI at 2.25 in (11.25 X/H) was $3.45 \times 10^{11} / \text{s}^2$. The vorticity calculated will be used in Chapter VI to correlate the enhanced mass entrainment that occurred during the SSLI.

V.1.3. Exit Pressure Ratio 3.50

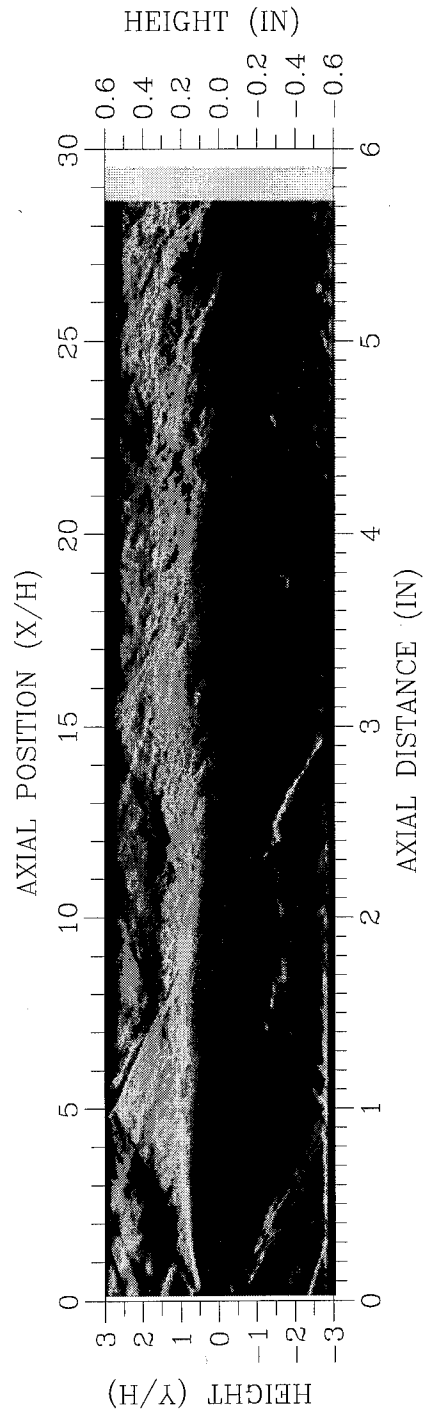
This EPR also represents theoretical case III but with an EPR of 3.50, over twice that of the previous pressure ratio. Mixing of the air-helium streams at this pressure ratio

has the same basic characteristics as EPR 1.49 but they are much more pronounced, as seen in the schlieren photographs (Fig. V-9). The helium jet in EPR 1.49 expanded outward at the exit plane forming oblique shocks in the air streams which reflected off the duct walls; intersected the helium jet then effectively dissipated. The helium jet in pressure ratio 3.50 also expands outward forming shocks in the air jets but the shocks are much stronger due to the greater turning of the shear layers required to equalize the exit pressures of the helium and air nozzles. These shocks reflect off the walls and intersect the helium jet three times before exiting the duct. The EPR theory predicts that the shear layer will need to turn 10 deg outward to equalize the exit pressures between the helium and air with a corresponding oblique shock in the air stream with an angle of 30.8 deg. The angles measured from the schlieren photographs were 11 ± 2 deg for the average shear layer turning angle and 29 ± 1 deg for the average oblique shock angle (Fig. V-10). The angle of the shocks changed little between the first and second reflection from the walls as shown in Figure V-10. After the shocks passed through the jet the second time at 4 in (20 X/H) downstream the shock angles increased to 35 ± 1 deg. The helium molar fraction contour plot, Figure V-11, shows the shear layer turning angle to be 9 ± 1 deg. The EPR theory predicted the initial expansion well for large EPR's considering the simplicity of the theory. The shocks, that were formed in the air streams, remained intact and reflected off the walls and continued reflecting off the walls as the EPR theory predicted. This is in contrast to the shocks in pressure ratio 1.49 which dissipated as they proceeded down the duct.

Examination of the flow downstream from the initial expansion region shows the helium jet getting narrower than it was after the initial expansion. This effect is due to the



a) Perpendicular knife edge



b) Parallel knife edge

Figure V-9: Schlieren photographs of EPR 3.50

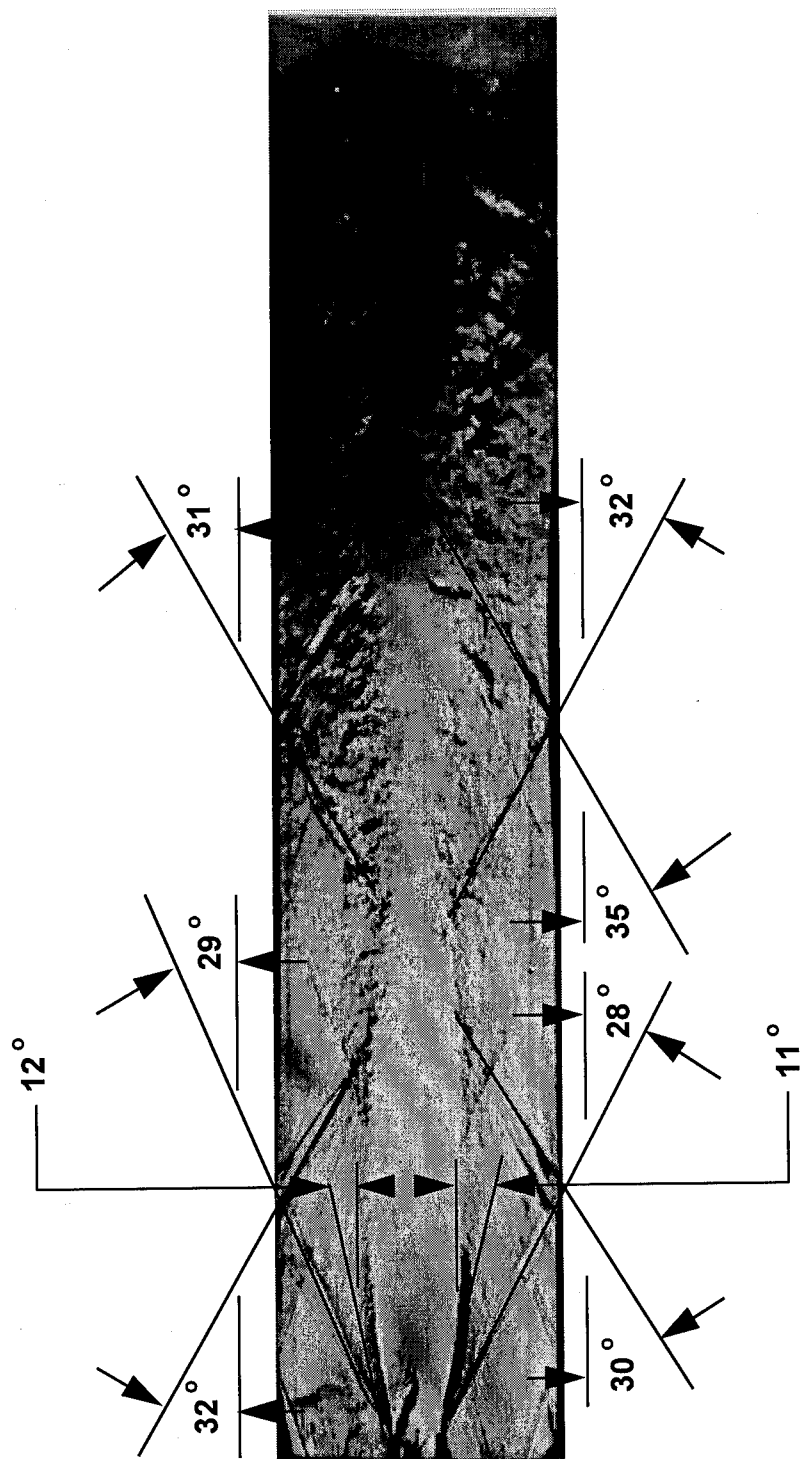


Figure V-10: EPR 3.50 shear layer and shock angles

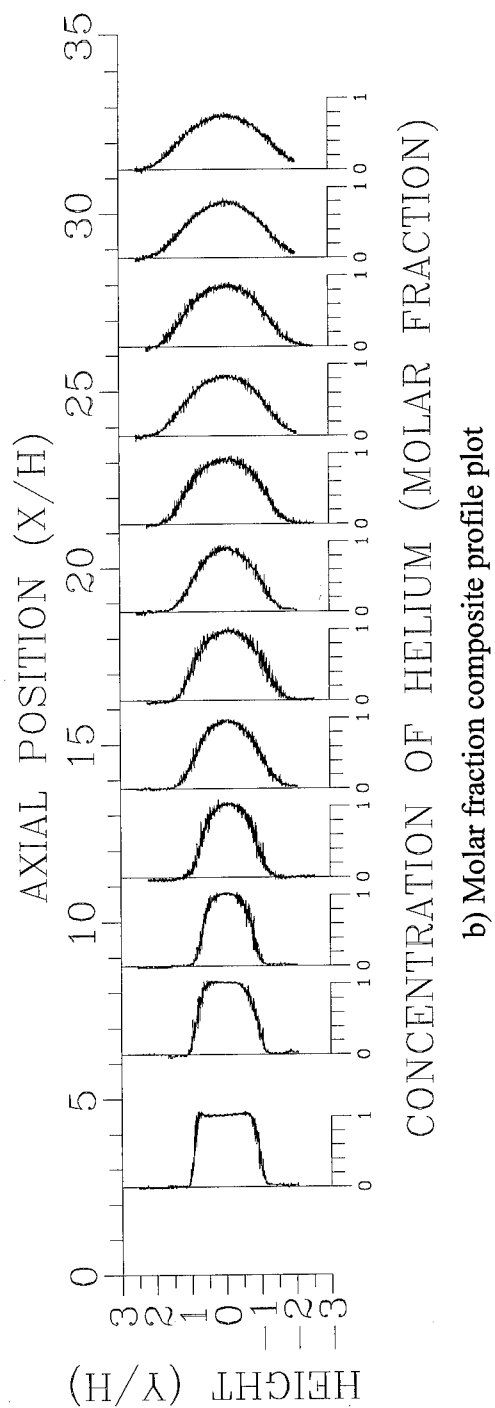
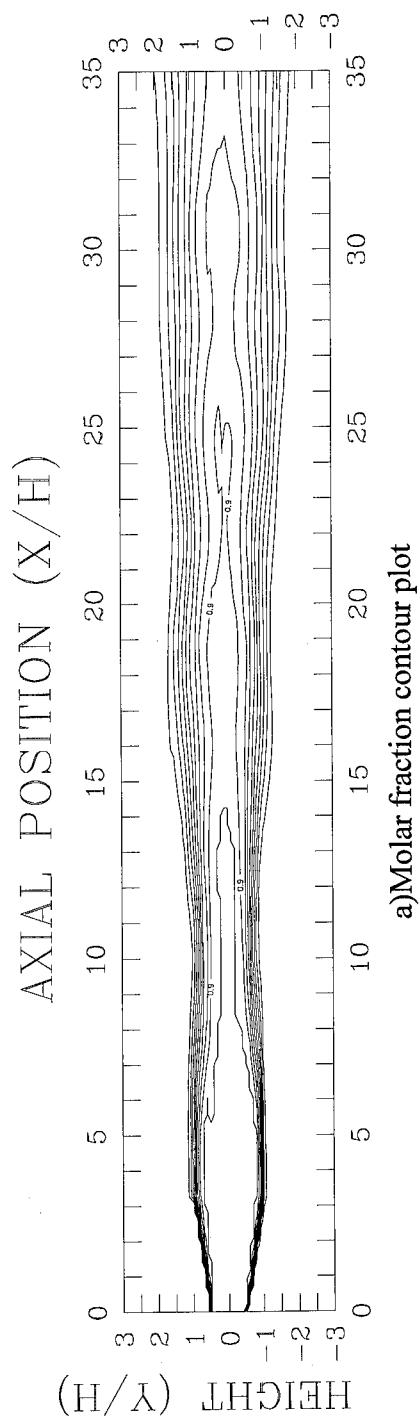
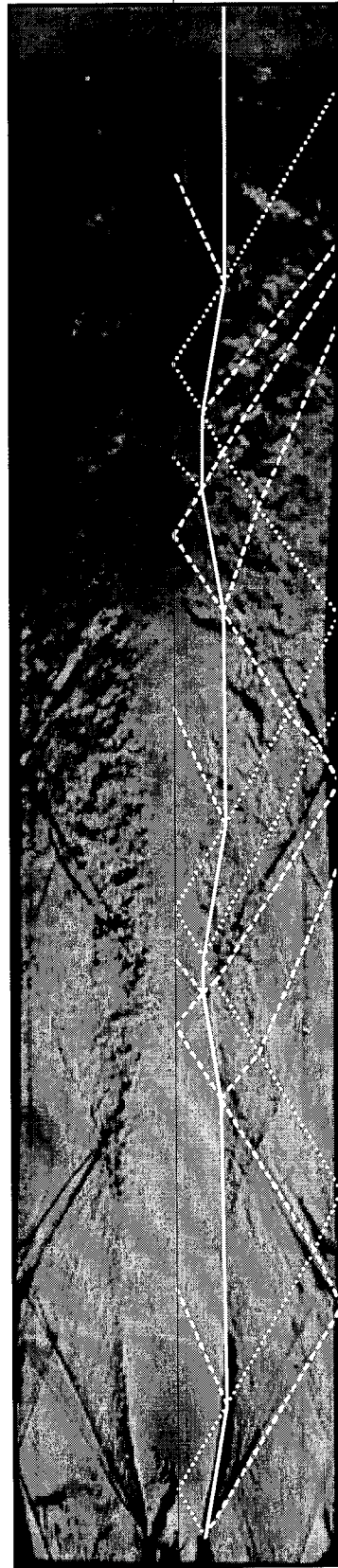


Figure V-11: Concentration plots for EPR 3.50

P-M expansion waves, that were generated within the helium jet when the shear layer turned outward, intersecting the shear layer and turning the shear layer towards the centerline. Both the schlieren photographs and the contour plot of the helium mole fraction show the expansion and then contraction which is due to gasdynamic effects and not viscous effects. The effects of the P-M expansion waves and the shock waves on the jet width are clearly shown by a simple wave analysis of the flowfield, shown in Figure V-12 overlaid on the schlieren photograph of EPR 3.50.

The shear layers that separate the helium and air streams are very thin in the initial region. The shear layers merge about 2.5 in (12.5 X/H) downstream and even at this point it is only the edges that are interacting. The schlieren photographs do not show the shear layers interacting with each other until about 4.5 in (22.5 X/H) downstream. In EPR 3.50, the helium jet does not appear to grow linearly after the initial expansion region which is due to the multiple SSLIs taking place. In EPR 0.89 the helium jet grew linearly with no major SSLIs. In EPR 1.49 the helium jet grew linearly before the SSLI and then grew linearly after the SSLI. In the present EPR there are two major SSLIs that are very pronounced and a third near the exit of the mixing duct that is not well defined. Because of the multiple SSLIs the helium jet does not have a chance to stabilize and grow linearly within the length of the duct. The helium jet alternately expands and contracts all the way down the mixing duct. The amount of expansion and contraction appears to diminish downstream and eventually the jet probably will grow linearly. An average growth rate of 0.06 in/in was measured from the concentration contour plot by ignoring all the expansions and contractions except the initial expansion due to the mismatched exit pressures. The shear layers do appear to grow linearly as they proceed downstream. The



- Prandtl-Meyer expansion
- Shock wave
- Jet boundary (He-Air Shear layer)

Figure V-12: Simple wave model of EPR 3.50

growth rates of the shear layers before they merged at 2.5 in (12.5 X/H) are 0.07 and 0.06 in/in for the upper and lower shear layers respectively, as determined by the concentration data (Fig. V-11).

The side wall static pressure clearly shows the effects of the EPR and the reflected shocks (Fig. V-13). The rapid drop in the centerline pressure due to the expansion within the helium jet is clearly visible. The shock waves are also evident by the rise of static pressures in the streamwise direction. The pressure rise due to the shock is smeared out and displaced forward from the actual shock location because of the shock boundary layer effects on the side walls where the pressure ports are located.

The relative vorticity generated during the first and second SSLI in EPR 3.50 was determined from the source term of Equation II-1, using the procedure outlined in Appendix C. The following details the calculation of the relative vorticity generated during the SSLIs at $X/H=8.75$ and $X/H=21.25$

CALCULATIONS FOR SSLI AT $X/H=8.75$

1. Calculate the pressure gradient ∇P :

The pressure across the shock was determined from the shock strength as determined from the upstream Mach number and the shock angle. A Mach wave angle upstream of the oblique shock, that intersected the shear layer at 8.75 X/H, was measured to be 25° therefore the upstream Mach number (M_1) was calculated to be 2.4. The oblique shock has an angle (Θ_{shock}) to the flow direction of 30° .

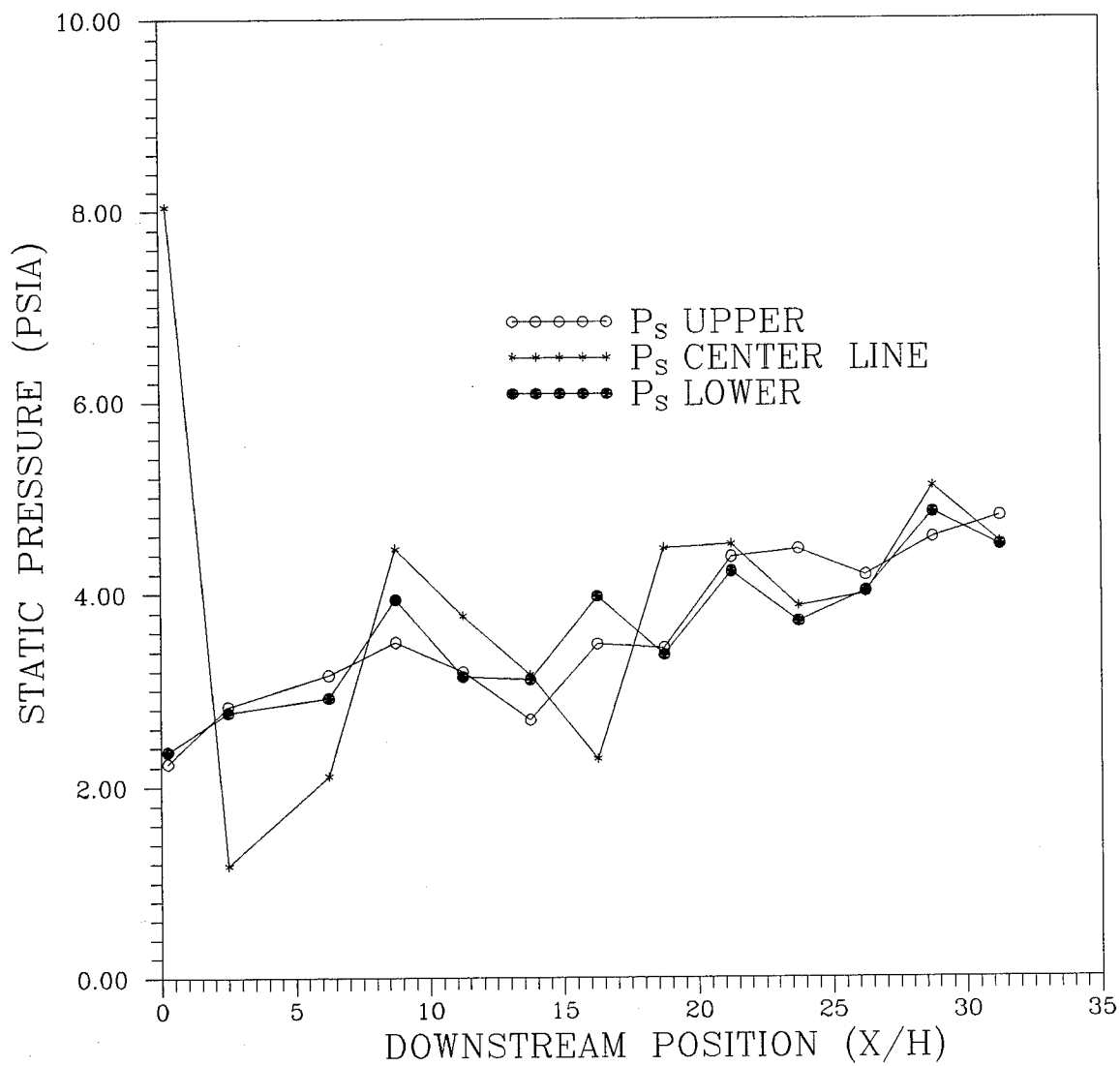


Figure V-13: Side wall static pressure for EPR 3.50

If $\Theta_{\text{shock}} = 30^\circ$ and $M_1 = 2.4$ then $\delta = 6.5^\circ$ and $\frac{P_2 - P_1}{1/2 \gamma M_1^2} = 0.12$ From NACA

Report No. 1135 (59) compressible flow tables. Using $\gamma=1.4$ and $M_1 = 2.4$ gives:

$$\frac{P_2}{P_1} = 0.12 \left(\frac{1}{P_1} \right) (1/2 \gamma M_1^2) + 1 = 1.48$$

The upstream static pressure (P_1) was measured to be 3.0 psia therefore $P_2 = 4.5$ psia. The shock thickness (ΔX_{shock}) was calculated using the following equation from Shapiro (56:133) for weak shocks

$$\frac{\rho_x C_x \Delta X_{\text{shock}}}{\mu_x} = \frac{4}{\gamma + 1} \left(\frac{4}{3} + \frac{\gamma - 1}{Pr^*} \right) \frac{1}{M_x^* - 1}$$

where ρ_x , C_x , and μ_x are the density, speed of sound and viscosity upstream from the shock and ΔX_{shock} is the shock thickness. Pr^* is the Prandtl number at conditions where the Mach number is unity and was taken to be that of air (0.75). M_x^* is the normal component of the Mach number, relative to the oblique shock, evaluated upstream of the shock and using the speed of sound at $M=1$.

$$M_x = M_1 \sin (\Theta_{\text{shock}})$$

$$M_x = 2.4 \sin (30)$$

$$M_x = 1.2 \quad \Rightarrow \quad M_x^* = 1.16 \quad \text{from NACA Report No. 1135 (59)}$$

compressible flow tables. The upstream speed of sound, density, and viscosity were calculated from measured temperatures and pressures.

$$C_x = 846 \frac{\text{ft}}{\text{s}} \quad \rho_x = 0.034 \frac{\text{lbm}}{\text{ft}^3} \quad \mu_x = 6.48 \times 10^{-6} \frac{\text{lbm}}{\text{ft} - \text{s}}$$

The shock thickness can now be calculated

$$\Delta X_{\text{shock}} = \frac{\mu_x}{\rho_x C_x} \frac{4}{\gamma + 1} \left(\frac{4}{3} + \frac{\gamma - 1}{Pr^*} \right) \frac{1}{M_x^* - 1}$$

$$\Delta X_{\text{shock}} = \frac{(6.48 \times 10^{-6} \frac{\text{lbm}}{\text{ft-s}})(12 \frac{\text{in}}{\text{ft}})}{(0.034 \frac{\text{lbm}}{\text{ft}^3})(846 \frac{\text{ft}}{\text{s}})} \frac{4}{1.4 + 1} \left(\frac{4}{3} + \frac{1.4 - 1}{.75} \right) \frac{1}{1.16 - 1}$$

$$\Delta X_{\text{shock}} = 5.32 \times 10^{-5} \text{ in}$$

The pressure gradient is then calculated.

$$\nabla P = \frac{P_2 - P_1}{\Delta X_{\text{shock}}} = \frac{4.5 - 3.0 \frac{\text{lbf}}{\text{in}^2}}{5.32 \times 10^{-5} \text{ in}} = 28195 \frac{\text{lbf}}{\text{in}^3}$$

2. Determine shear layer density gradient $\nabla \rho_{\text{sl}}$:

The shear layer thickness (ΔX_{SL}) at the interaction point was measured to be

0.12 in. The density in the air stream (ρ_{air}) was calculated to be $0.034 \frac{\text{lbm}}{\text{ft}^3}$ and the

density on the jet centerline (ρ_{CL}) was calculated to be $0.006 \frac{\text{lbm}}{\text{ft}^3}$. The density

gradient is then calculated to be:

$$\nabla \rho = \frac{\rho_{\text{Air}} - \rho_{\text{CL}}}{\Delta X_{\text{SL}}} = \frac{0.034 - 0.006 \left(\frac{\text{lbm}}{\text{ft}^3} \right)}{0.12 \text{ in}} = 0.23 \left(\frac{\text{lbm}}{\text{in} - \text{ft}^3} \right)$$

3. Determine average shear layer density $\bar{\rho}_{\text{sl}}$:

$$\bar{\rho}_{\text{sl}} = \frac{\rho_{\text{Air}} + \rho_{\text{CL}}}{2} = \frac{0.034 + 0.006 \left(\frac{\text{lbm}}{\text{ft}^3} \right)}{2} = 0.020 \left(\frac{\text{lbm}}{\text{ft}^3} \right)$$

4. Angle between pressure and density gradients:

The angle between the pressure and density gradients (Θ) at $X/H=8.75$, the location of the SSL, was measured from the schlieren photographs to be 33° .

5. Calculate relative vorticity from the source term in Equation II-1:

$$\text{RELATIVE VORTICITY } (\bar{\zeta}) = \frac{\nabla P \times \nabla \rho_{sl}}{(\bar{\rho}_{sl})^2} \sin \Theta$$

$$\text{RELATIVE VORTICITY } (\bar{\zeta}) = \frac{\left(28195 \frac{\text{lbf}}{\text{in}^3}\right) \times \left(0.23 \frac{\text{lbm}}{\text{ft}^3 \cdot \text{in}}\right) \sin(23^\circ) \left(32.2 \frac{\text{lbm} \cdot \text{ft}}{\text{lbf} \cdot \text{s}^2}\right) \left(12 \frac{\text{in}}{\text{ft}}\right)}{\left(0.02 \frac{\text{lbm}}{\text{ft}^3}\right)^2}$$

$$\text{RELATIVE VORTICITY } (\bar{\zeta}) = 5.72 \times 10^{12} \text{ } 1/\text{s}^2$$

CALCULATIONS FOR SSLI AT $X/H=21.25$

1. Calculate the pressure gradient ∇P :

The pressure across the shock was determined from the shock strength as determined from the upstream Mach number and the shock angle. A Mach wave angle and the oblique shock angles were the same as for the first SSLI in EPR 3.50 measuring 25° and 30° respectively. From the first SSLI for EPR 3.50 the upstream Mach number is 2.4 and $\frac{P_2}{P_1} = 1.48$. The upstream static pressure (P_1) was measured to be 3.4 psia therefore $P_2 = 5.0$ psia. The shock thickness (ΔX_{shock}) was calculated using the following equation from Shapiro (56:133) for weak shocks

$$\frac{\rho_x C_x \Delta X_{\text{shock}}}{\mu_x} = \frac{4}{\gamma + 1} \left(\frac{4}{3} + \frac{\gamma - 1}{Pr^*} \right) \frac{1}{M_x^* - 1}$$

where ρ_x , C_x , and μ_x are the density, speed of sound and viscosity upstream from the shock and ΔX_{shock} is the shock thickness. Pr^* is the Prandtl number at conditions where the Mach number is unity and was taken to be that of air (0.75). M_x^* is the normal component of the Mach number, relative to the oblique shock, evaluated upstream of the shock and using the speed of sound at $M=1$.

$$M_x = M_1 \sin(\Theta_{\text{shock}})$$

$$M_x = 2.4 \sin(30)$$

$$M_x = 1.2 \quad \Rightarrow \quad M_x^* = 1.16 \quad \text{from NACA Report No. 1135 (59)}$$

compressible flow tables. The upstream speed of sound, density, and viscosity were calculated from measured temperatures and pressures.

$$C_x = 792 \frac{\text{ft}}{\text{s}} \quad \rho_x = 0.035 \frac{\text{lbm}}{\text{ft}^3} \quad \mu_x = 6.60 \times 10^{-6} \frac{\text{lbm}}{\text{ft} \cdot \text{s}}$$

The shock thickness can now be calculated

$$\Delta X_{\text{shock}} = \frac{\mu_x}{\rho_x C_x} \frac{4}{\gamma + 1} \left(\frac{4}{3} + \frac{\gamma - 1}{Pr^*} \right) \frac{1}{M_x^* - 1}$$

$$\Delta X_{\text{shock}} = \frac{(6.60 \times 10^{-6} \frac{\text{lbm}}{\text{ft} \cdot \text{s}})(12 \frac{\text{in}}{\text{ft}})}{(0.035 \frac{\text{lbm}}{\text{ft}^3})(792 \frac{\text{ft}}{\text{s}})} \frac{4}{1.4 + 1} \left(\frac{4}{3} + \frac{1.4 - 1}{.75} \right) \frac{1}{1.16 - 1}$$

$$\Delta X_{\text{shock}} = 6.35 \times 10^{-5} \text{ in}$$

The pressure gradient is then calculated.

$$\nabla P = \frac{P_2 - P_1}{\Delta X_{\text{shock}}} = \frac{5.0 - 3.4 \frac{\text{lbf}}{\text{in}^2}}{6.35 \times 10^{-5} \text{ in}} = 25197 \frac{\text{lbf}}{\text{in}^3}$$

2. Determine shear layer density gradient $\nabla \rho_{sl}$:

The shear layer thickness (ΔX_{SL}) at the interaction point was measured to be

0.24 in. The density in the air stream (ρ_{air}) was calculated to be $0.035 \frac{\text{lbm}}{\text{ft}^3}$ and the

density on the jet centerline (ρ_{CL}) was calculated to be $0.010 \frac{\text{lbm}}{\text{ft}^3}$. The density

gradient is then calculated to be:

$$\nabla \rho = \frac{\rho_{Air} - \rho_{CL}}{\Delta X_{SL}} = \frac{0.035 - 0.010 \left(\frac{\text{lbm}}{\text{ft}^3} \right)}{0.24 \text{ in}} = 0.10 \left(\frac{\text{lbm}}{\text{in} - \text{ft}^3} \right)$$

3. Determine average shear layer density $\bar{\rho}_{sl}$:

$$\bar{\rho}_{sl} = \frac{\rho_{Air} + \rho_{CL}}{2} = \frac{0.035 + 0.010 \left(\frac{\text{lbm}}{\text{ft}^3} \right)}{2} = 0.023 \left(\frac{\text{lbm}}{\text{ft}^3} \right)$$

4. Angle between pressure and density gradients:

The angle between the pressure and density gradients (Θ) at $X/H=21.25$, the

location of the SSL, was measured from the schlieren photographs to be 30° .

5. Calculate relative vorticity from the source term in Equation II-1:

$$\text{RELATIVE VORTICITY } (\bar{\zeta}) = \frac{\nabla P \times \nabla \rho_{sl}}{(\bar{\rho}_{sl})^2} \sin \Theta$$

$$\text{RELATIVE VORTICITY } (\bar{\zeta}) = \frac{(25197 \frac{\text{lbf}}{\text{in}^3}) \times (0.10 \frac{\text{lbm}}{\text{ft}^3 - \text{in}})}{(0.023 \frac{\text{lbm}}{\text{ft}^3})^2} \sin(30^\circ) \left(32.2 \frac{\text{lbm} - \text{ft}}{\text{lbf} - \text{s}^2} \right) \left(12 \frac{\text{in}}{\text{ft}} \right)^4$$

$$\text{RELATIVE VORTICITY } (\bar{\zeta}) = 1.59 \times 10^{12} \text{ } 1/\text{s}^2$$

The above calculations showed that the relative vorticity generated during the first and second SSLI were $5.72 \times 10^{12} /s^2$ and $1.59 \times 10^{12} /s^2$ respectively. These values for the relative vorticity will be used in Chapter VI to correlate the enhanced mass entrainment rates with the strength of the SSLI.

V.2. Centerline Decay

The decay of the jet's centerline helium concentration is a measure of the mixing between the air and helium within the duct. A plot of the centerline mass fraction (C_{mass}) versus axial distance is given in Figure V-14 with a power law curve fit of the form

$$C_{mass} = A (X/H)^{-B} \quad (V-1)$$

where A and B are constants determined by a least squares fit to the experimental data.

Figure V-14 shows that the centerline concentration data do not fit the power law exactly but deviate slightly. The power law decay is generally for free jets with constant axial pressure; the data are for confined jets with variable axial pressure, caused by both the confining duct and the oblique shocks within the duct, thus the power law would not be expected to fit the data exactly. Most of the data presented in the literature are for free jets that decay to the freestream gas concentration rather than for confined jets that decay to a concentration between that of the freestream and the jet. In order to make comparisons to the free jet data a parameter is proposed that compares the centerline concentration to the fully mixed concentration (C_{FM}). This parameter is given by the following equation.

$$\bar{C}_{mass} = \frac{C_{mass} - C_{FM}}{1 - C_{FM}} \quad (V-2)$$

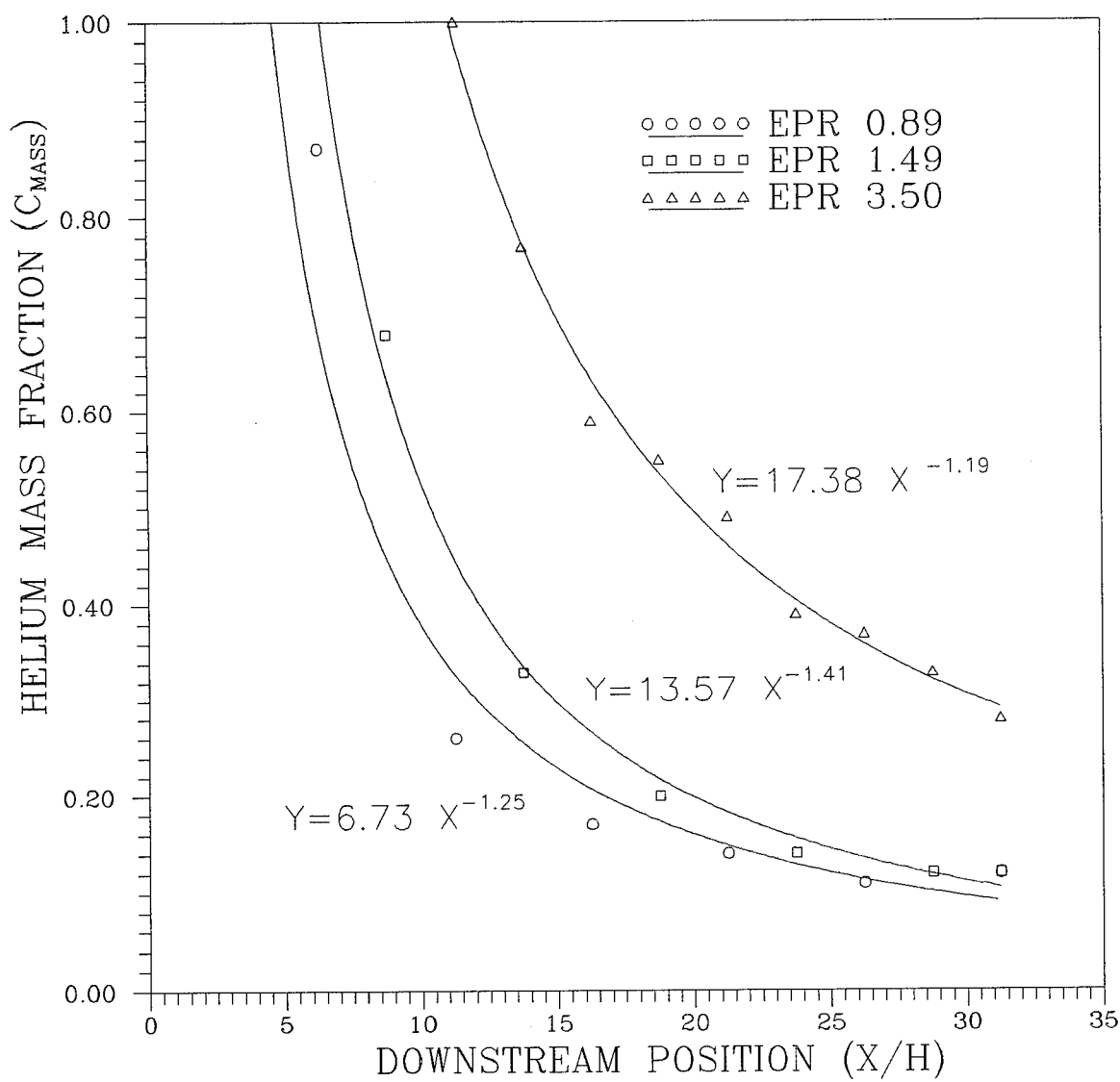


Figure V-14: Jet centerline helium mass fraction versus X/H

This parameter takes on the value of 1 when the concentration is pure helium and a value of 0 when the flow is totally mixed. It reduces to the concentration for free jets when the fully mixed concentration approaches zero ($C_{FM} \Rightarrow 0.0$). A plot of \bar{C}_{mass} versus X/H is given in Figure V-15. Table V-1 shows the fully mixed concentrations used to calculate \bar{C}_{mass} in Figures V-15.

Table V-1: Fully Mixed concentrations

EPR	Fully Mixed Concentration (C_{FM}) He Mass Fraction
0.89	0.043
1.49	0.072
3.50	0.150

There appears to be little variation between the mass fraction and mass parameter plots (Figs. V-14 and V-15) other than the mass parameter being slightly lower than the mass fraction. The reason there is such a small difference between the mass fraction and the mass parameter plots results from the fully mixed concentrations being close to zero, the fully mixed free jet concentration, as shown in Table V-1.

The centerline decay data for the three pressure ratios is not well correlated because of the difference in the length of the potential core in the helium jet. Hamelin (60:25) used a non-dimensional axial distance based on the length of the potential core (L_{pc}) rather than the jet height (H). This non-dimensional parameter was originally used by Zakkey and Krause (61) in the study of axisymmetric jets. The mass concentration parameter (\bar{C}_{mass}) versus X/L_{pc} (Fig. V-16) correlates the centerline concentration of all

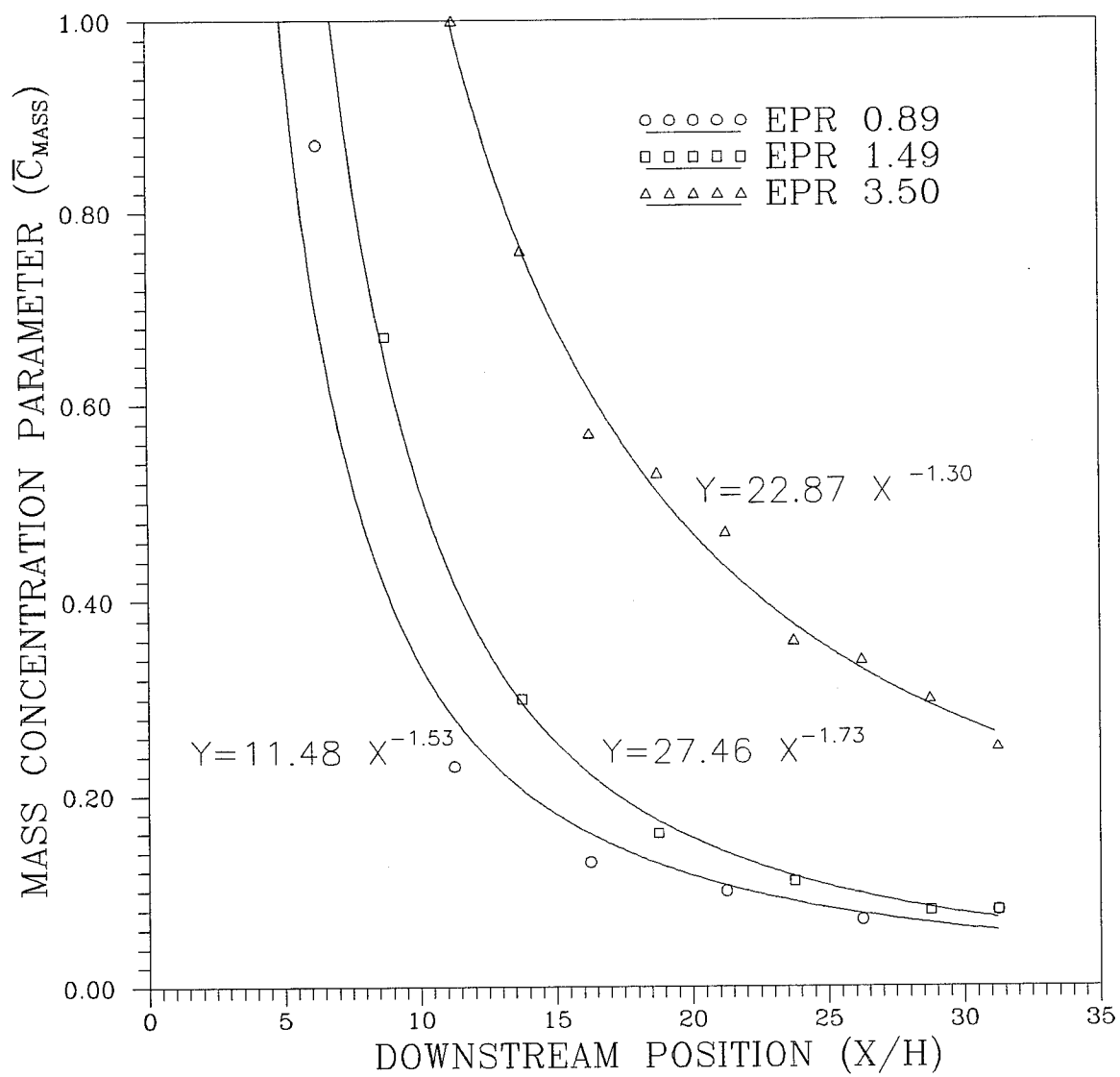


Figure V-15: Mass concentration parameter versus X/H

three EPRs nicely. The parameters \bar{C}_{mass} and X/L_{pc} appear to be universal parameters that will correlate both confined and free jets as well as axisymmetric and planar jets.

The decay rate exponents, B in Equation V-1, for the three pressure ratios tested are presented in Table V-2 along with decay rate exponent data for axisymmetric free jets from Schetz (62:45) with momentum ratios similar to the ones in this study, $(\rho V)_{he}/(\rho V)_{air} = 0.21-0.58$.

Table V-2: Center line decay rate exponents*

Exit Pressure	Measured Decay Exponent			Free Jet Exponent from Schetz (62:45)
Ratio (EPR)	C_{mass} vs. X/H	\bar{C}_{mass} vs. X/H	\bar{C}_{mass} vs. X/L_{pc}	C_{mass}
0.89	1.25	1.53	1.63	1.7-2.0
1.49	1.41	1.73	1.63	1.7-2.0
3.50	1.19	1.30	1.63	1.7-2.0

*Exponent B in Equation V-1

The measured decay rate exponents were determined by a least squares fit to the data as shown in Figures V-14 to V-16. The decay rates are just below the accepted range for axisymmetric free jets (last column in Table V-2) indicating confined planar jets generally decay slower than free axisymmetric jets with similar momentum ratios. Hamelin (60) studied two-dimensional sonic helium jets exhausting coaxially into a Mach 1.54 air jet with a momentum ratio of $(\rho V)_{he}/(\rho V)_{air} = 0.125$ and found an exponent of 1.33 (60:26) correlated his data well. Hamelin's value for the decay rate exponent is also lower than the published value of 2.0 for an axisymmetric free jet with a similar momentum ratio. The exponent of 1.63 correlated all of the centerline decay data acquired in this

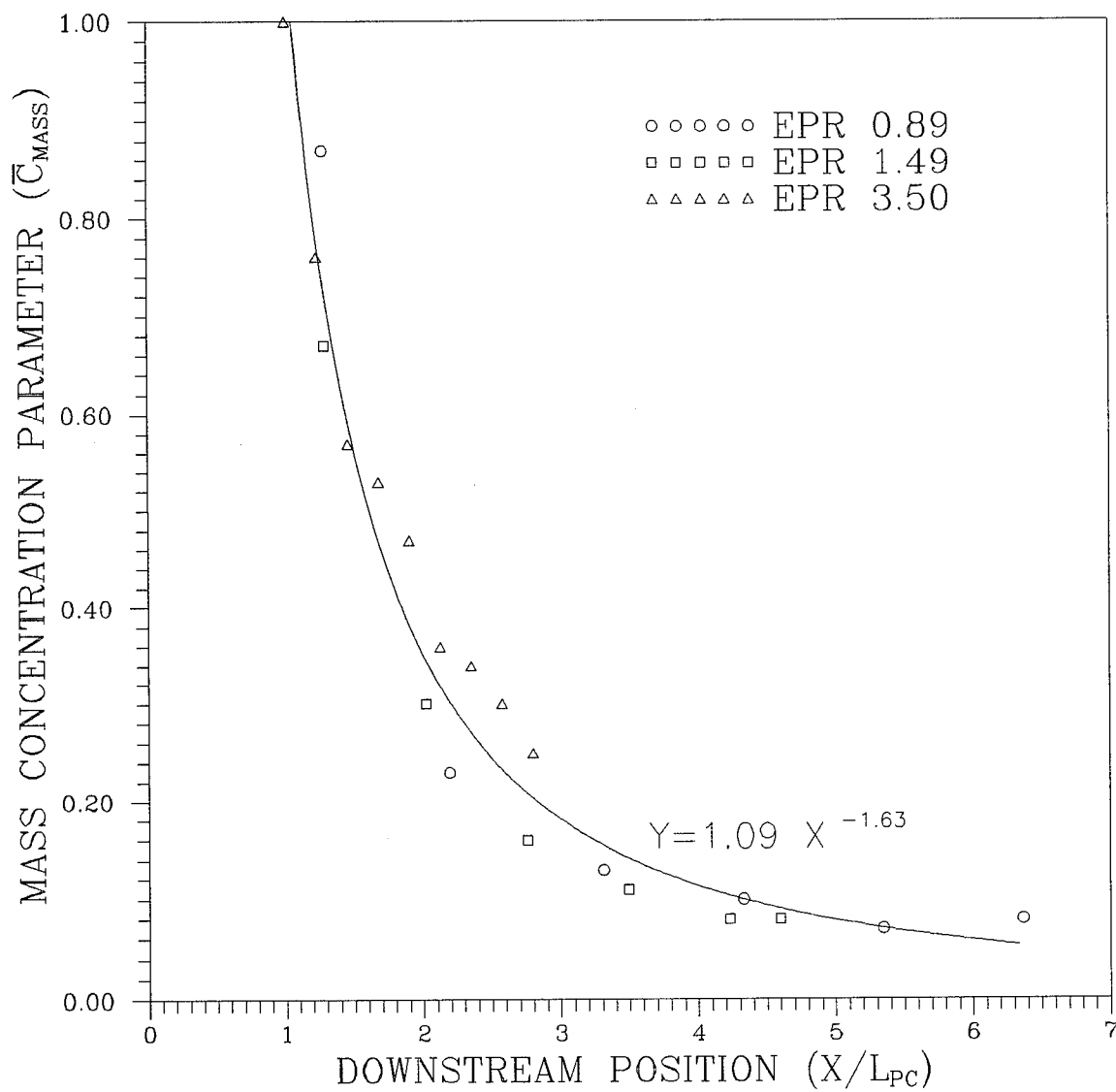


Figure V-16: Mass concentration parameter versus X/L_{PC}

investigation. It is recommended that for confined planar jets similar to those in this study, with momentum ratios between 0.21 and 0.50, a value near 1.6 should be used for the centerline mass concentration decay exponent. The universal centerline decay equation for confined planar supersonic jets is then as follows:

$$\bar{C}_{\text{mass}} = 1 \times \left(\frac{X}{L_{\text{pc}}} \right)^{-1.6} \quad (\text{V-3})$$

Equation V-3 defines the centerline mass concentration given the initial injection mixture and the length of the potential core. A plot of L_{pc} versus EPR, Figure V-17, indicates that the potential core length is nearly linear with EPR for EPRs between 0.89 and 3.50.

Equation V-4 defines the potential core length in terms of EPR ($0.89 < \text{EPR} < 3.50$); thus knowing the EPR and using Equations V-4 and V-3 an estimate of the centerline concentration can be determined.

$$\left(\frac{L_{\text{pc}}}{H} \right) = 2.336 (\text{EPR}) + 3.037 \quad (\text{V-4})$$

V.3. Jet Growth Rates

The helium jet grows spatially as it proceeds downstream due to both the gasdynamic effect of the high exit pressure ratio and the entrainment of mass into the jet. The jet's growth was observed and measured in both the schlieren photographs and the helium concentration plots presented in Section V.1. The changes in the jet growth are best seen by plotting the width of the jet versus X/H as shown in Figure V-18. The edge

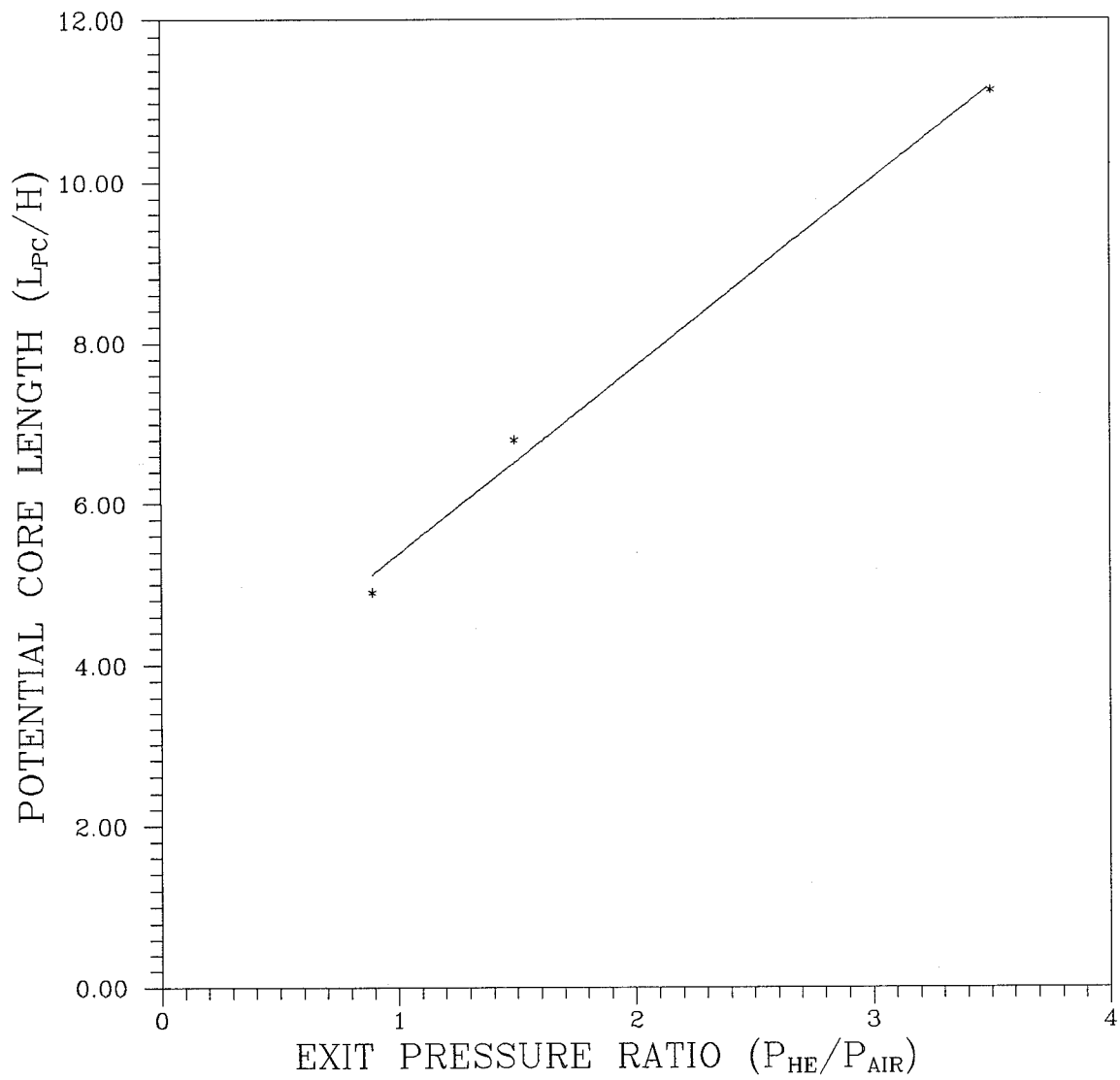


Figure V-17: Potential core length versus EPR

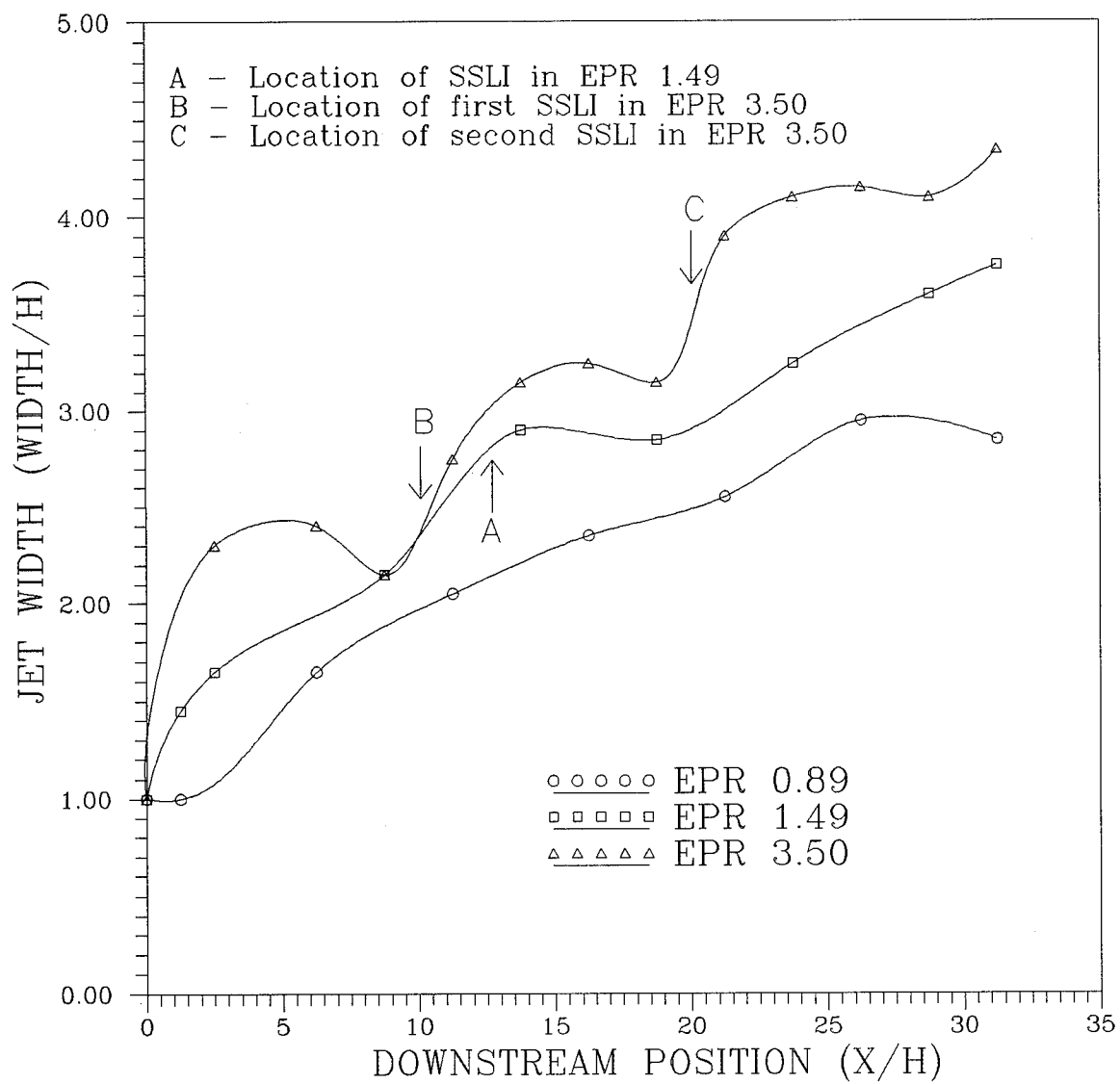


Figure V-18: Jet width versus X/H

of the jet was arbitrarily defined as the locus of points where the helium molar fraction reaches 0.03. In EPR 0.89 the jet grows linearly with no major perturbations as would be expected because of the lack of both a large EPR and a SSLI. The jet in EPR 1.49 grows relatively linearly with a small perturbation near the location of the SSLI (Fig. V-18, Point A). For EPR 3.50 the jet width changes abruptly several times due to the large EPR and strong SSLIs. The initial growth of the jet is due to the gasdynamic effect of the large EPR while the later changes in the jet width are due to both gasdynamic effects of the shock changing the flow direction at the edge of the jet and from additional mass being entrained into the jet at the SSLI location. Figure V-18 shows a negative growth of the jet just preceding the shock penetration points (Fig. V-18, Points B and C) followed by a rapid growth of the jet while the shock is passing through the jet. The negative change in the jet width is due to the turning of the flow by the gasdynamic effects of the P-M and shock waves. As the flow is turned the jet's boundary is moved toward the duct centerline and the width of the jet is reduced. The mass within the jet is not being reduced but the density within the jet is increased. Figure V-19 is a plot of the ratio of the jet centerline density to the air stream density. The density ratio plot shows the jet density increasing relative to the air stream density as the jet width decreases. The rapid growth of the jet after the shock penetration is due to rapid mass entrainment from the SSLI as well as some gasdynamic effects of the P-M and shock waves. The magnitude of the jet growth during the SSLI should be proportional to the relative vorticity generated by the SSLI. The current data show some difference in growth rate with the relative vorticity generated but the data are insufficient to postulate a quantitative correlation. A study by Menon (42)

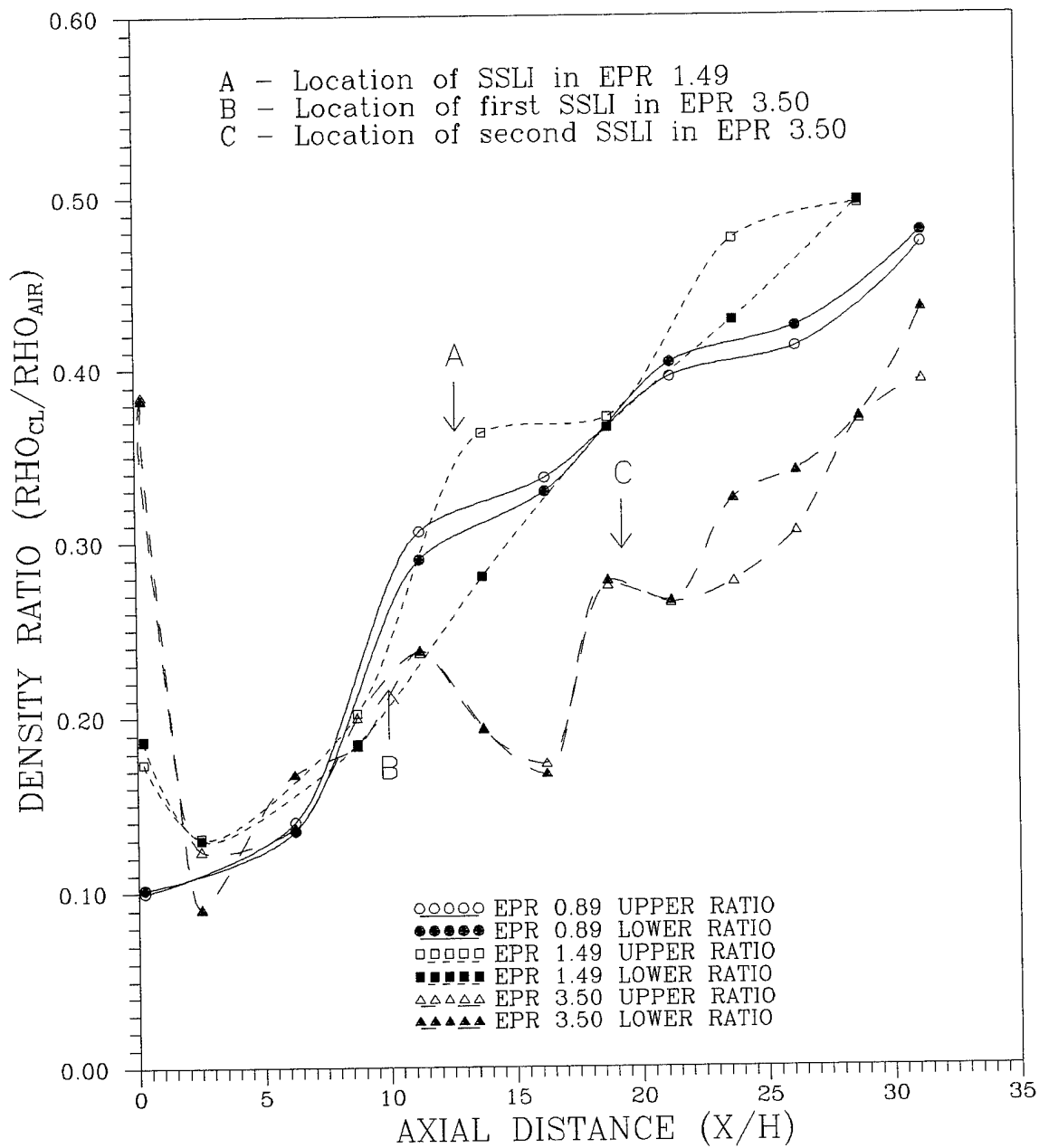


Figure V-19: Density ratio versus X/H

showed similar effects between an oblique shock and a helium wall jet. Menon's data were also insufficient to postulate a quantitative correlation between vorticity and shear layer growth rate. Experimental studies on air-air shear layers and jets have not observed any measurable change in the growth rate of jets or shear layers due to SSLIs (18:7, 43:5). In the air-air shear layer studies the relative vorticity has been small due to a small density gradient across the shear layer or jet. The data in this study are significant because the data show significant change in growth rate with SSLIs similar to the data by Menon confirming growth rate enhancement due to SSLIs. Quantitative correlation between vorticity generation, due to SSLIs, and mass entrainment rates will be developed in the next chapter.

V.4. Summary

- The flowfield for the three EPRs tested behaves as expected from the EPR theory developed in Chapter II.
- The jet and shear layer growth rates measured between SSLI are consistent with published values for similar flow conditions.
- Centerline helium concentrations can be universally correlated with axial distance when non-dimensionalized with the fully mixed concentration and the jets potential core length respectively. The universal decay exponent is near 1.6 for jets similar to the ones in this study.
- The jet potential core length is varies linearly with EPR and is given by:

$$\left(\frac{L_{pc}}{H} \right) = 2.336 (EPR) + 3.037$$

- Jet growth rates are enhanced by SSLIs but insufficient data is available to postulate a quantitative relationship between growth rates and SSLI strength. Chapter VI will develop a quantitative relationship between SSLI strength as measured by the vorticity generated and the mass entrained during the SSLI.

VI. Mass Entrainment Results

The previous chapter discussed the experimental data that described the flowfield, the centerline decay rates, and the jet growth rates. In this chapter the experimental data will be used to calculate mass entrainment rates and then correlate them with the strength of the SSLI, as measured by the vorticity generated, and the EPR to show the significance of both SSLIs and the EPR on mass entrainment. The correlations developed in this chapter will lay the foundations for the model that will be developed in the next chapter to predict mass entrainment along shear layers and jets in confined ducts with SSLI and high EPR.

VI.1. Calculations of Mass Flux and Mass Entrainment Data

The binary gas concentration probe proved to be an invaluable piece of instrumentation for this investigation. The probe permitted simultaneous measurement of all parameters needed to determine the local helium concentration in the flow; this represents a significant improvement over prior instrumentation. Although initially designed and calibrated to measure only helium concentration, it was later determined, during the analysis of the data, that the probe could provide helium mass flux measurements from the data acquired. The mass flux is calculated by dividing the mass flow through the probe by the inlet area of the probe (Eq. VI-1).

$$\text{Local mass flux} = (\rho V)_{\text{local}}$$
$$\text{Local mass flux} = \frac{P_0 \cdot A^*}{A_{\text{in}} \sqrt{T_0}} \sqrt{\frac{\gamma_m}{R_m} \left(\frac{2}{\gamma_m + 1} \right)^{\frac{\gamma_m + 1}{\gamma_m - 1}}} \quad (\text{VI-1})$$

All the variables in Equation VI-1 are either measured by the concentration probe (P_0 , T_0), represent design parameters (A^* , A_{in}), or are functions of the gas composition (γ_m , R_m), which is now known from the concentration measurements. The inlet area to the probe, A_{in} is 0.000133 in^2 which was calculated from the probe inlet diameter of 0.013 in. Once the mass flux is known then the helium mass flux can be calculated by multiplying the mass flux by the helium mass fraction, Equation VI-2.

$$\text{Local helium mass flux} = (\rho V)_{\text{He local}}$$

$$\text{Local helium mass flux} = (\rho V)_{\text{local}} \left(\frac{X_{\text{He}} \cdot m_{\text{He}}}{X_{\text{He}} \cdot m_{\text{He}} + (1 + X_{\text{He}}) \cdot m_{\text{He}}} \right) \quad (\text{VI-2})$$

With the local helium mass flux and local mass flux determined, the local air mass flux was obtained simply by subtracting the helium mass flux from the mass flux. With the local helium and air mass fluxes known the helium and air mass flow within the jet can be calculated by integrating the appropriate local mass flux across the jet.

Since the concentration probe was not originally designed for mass flux measurements but for concentration measurements, no mass flux calibration was performed. An estimate of the mass flux error due to the effect of the molar fraction error, discussed in Section IV.4, was made by calculating the mass flux with an assumed molar fraction error of ± 0.05 . When the ± 0.05 molar fraction error was applied randomly to the helium concentration data no significant changes to the curves were noticed. With a

+0.05 or a -0.05 error added to the helium concentration data the mass flux and integrated mass flow within the jet were offset proportionally. The error bars on the mass flow figures in this chapter show the result of this error analysis. It was found that the molar concentration error has a larger effect near the nozzle exit plane where the mass in the jet consisted primarily of helium than further down the duct where the jet has a significant amount of entrained air.

The helium mass flow data allowed a continuity check on the helium mass flow within the duct. The helium mass flux, as measured by the concentration probe, was integrated across the duct and compared to the helium mass flow injected into the duct which was determined by isentropic relations using the measured helium total pressure and the throat area of the helium nozzle. Figure VI-1 shows the ratio between the integrated and injected helium mass flow for the three EPRs investigated along with margins of error determined from the error analysis discussed above. Since the ratio should be 1.0 along the entire duct, there appears to be a loss then a gain in helium mass flow along the duct centerline as the helium flows down the duct. The data are showing that either the concentration probe is not measuring the mass flux correctly or the helium concentration is not uniform across the duct. The error is probably due to both, the probe and the non-uniformities. From the changes in the helium mass flow measurements along the duct there probably is a non-uniform helium distribution along the span of the duct rather than large errors in the probe measurements. There appears to be less helium flow along the centerline than elsewhere in the duct, except near the nozzle exit plane where there may be slightly more helium on the centerline than elsewhere in the duct. The data appears to show that as the helium flows downstream and mixes with the air the uniformity across the

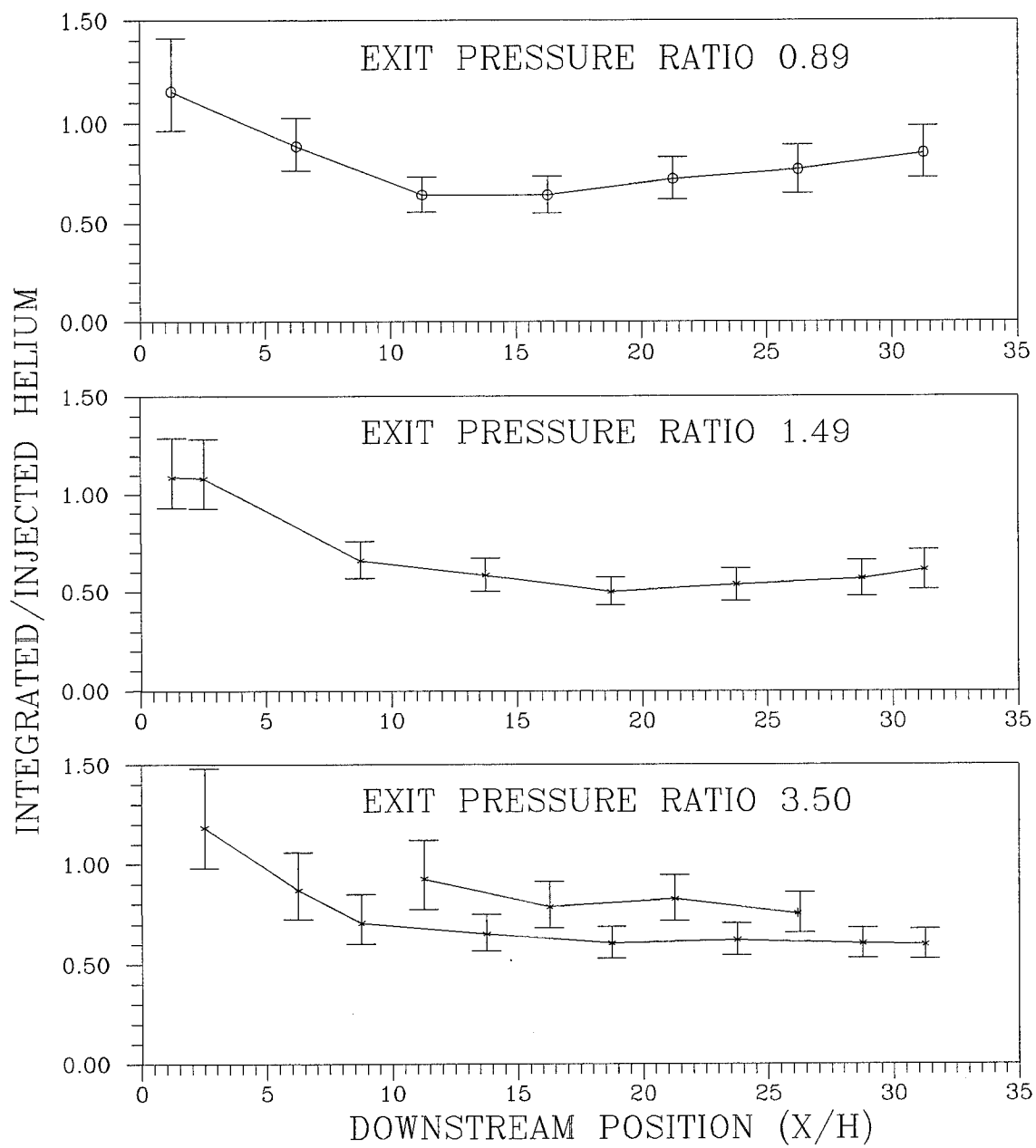


Figure VI-1: Ratio of integrated to injected helium mass versus X/H

duct improves as can be seen by the increase in ratio of integrated to injected mass flow of helium along the duct centerline in EPRs 0.89 and 1.49. For this investigation the data tends to indicate that there is a non-uniform helium distribution along the span of the duct but because the data were obtained only along the duct centerline plane these conjectures cannot be resolved without further investigation.

For EPR 3.50 data were initially taken at 0.5, 1.25, 1.75, 2.75, 3.75, 4.75, 5.75, and 6.25 in locations, and to better define the regions where large changes occurred, data were acquired at 2.25, 3.25, 4.25 and 5.25 in locations in order to have data approximately every 0.5 in. The additional data were acquired with a different concentration probe, as a result of sensor failure, using pressure setting as close to the original as possible. The changes led to slightly different test conditions and possibly a shift in the helium concentration distribution along the span of the duct for four of the data points; thus resulting in the two curves for EPR 3.50 in Figure VI-1.

VI.2. Mass Entrainment

Using the method described above for calculating the mass flow within the jet, an estimate of the mass entrained into the jet was made and mass entrainment rates determined, based on measurements for the centerline plane. Figures VI-2 to VI-5 show the total mass within the jet's boundary as measured by the concentration probe, for each EPR. Figure VI-2 shows the entrainment for all three EPRs without error bars while Figures VI-3 to VI-5 show each EPR with the estimated margin of error. The most striking feature of Figure VI-2 is that all three EPRs entrain mass at about the same gross rate regardless of the EPR. The second major feature is the steps in the mass entrainment

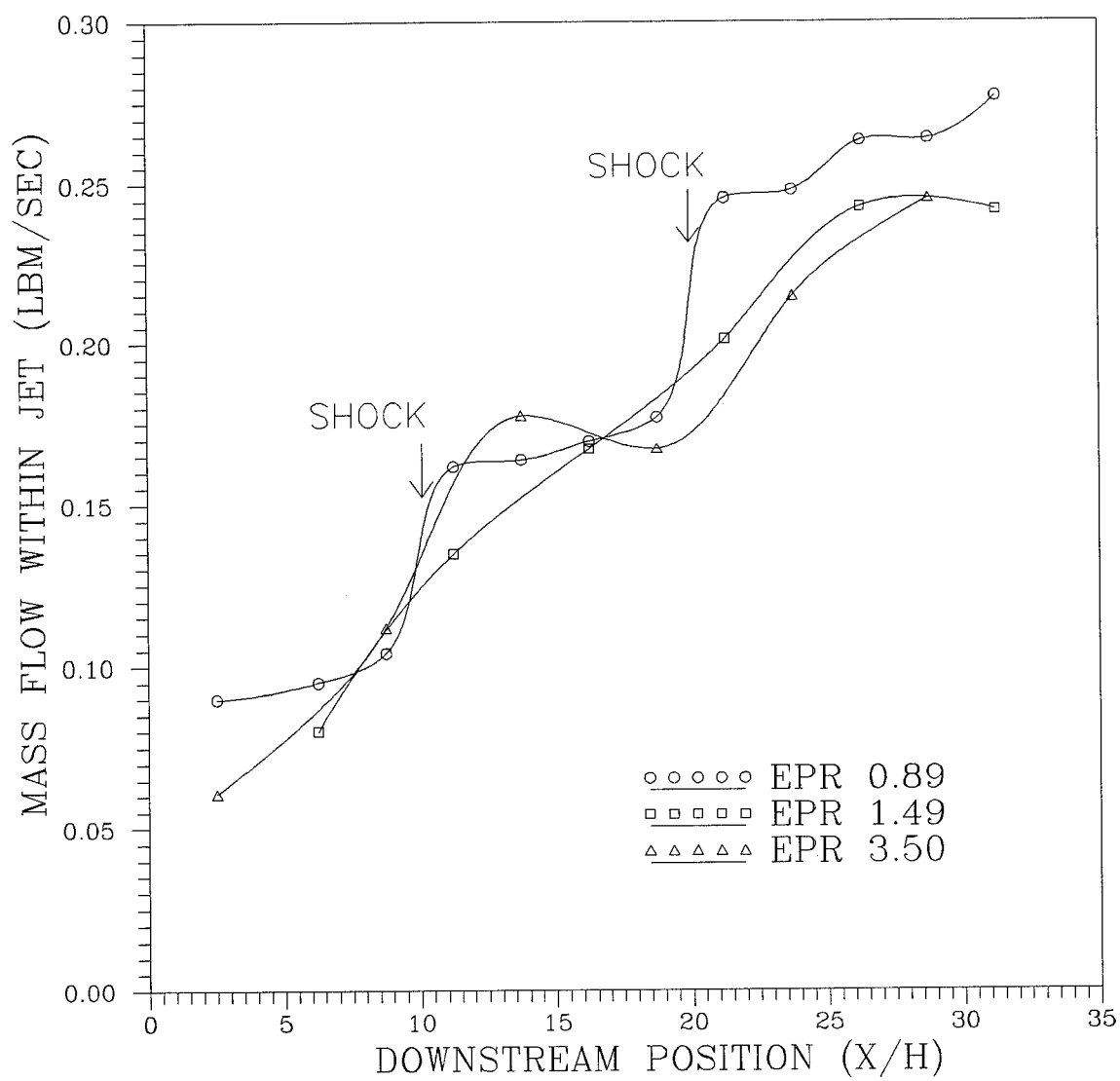


Figure VI-2: Mass flow within jet versus X/H, all EPRs

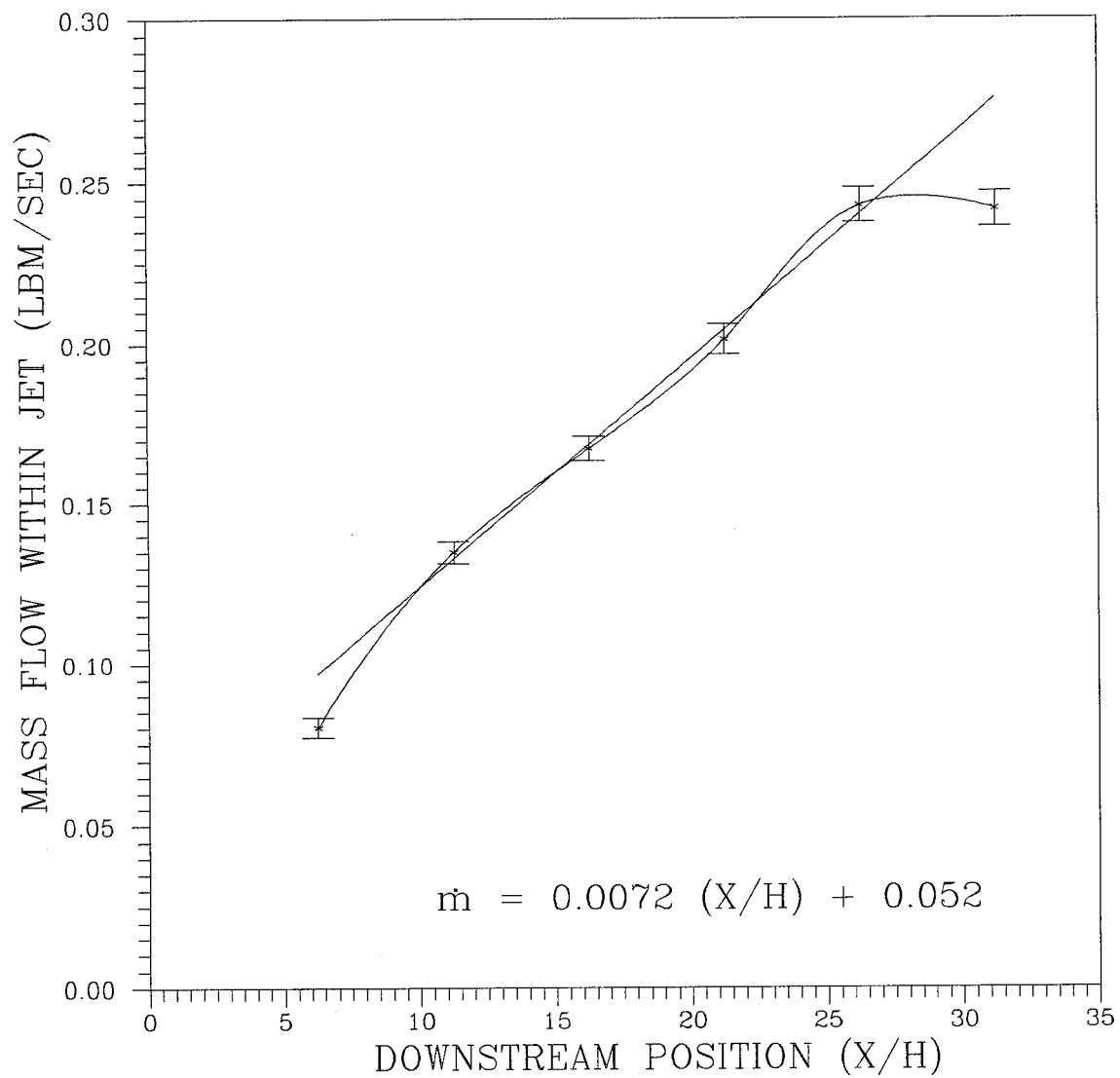


Figure VI-3: Mass flow within jet versus X/H for EPR 0.89

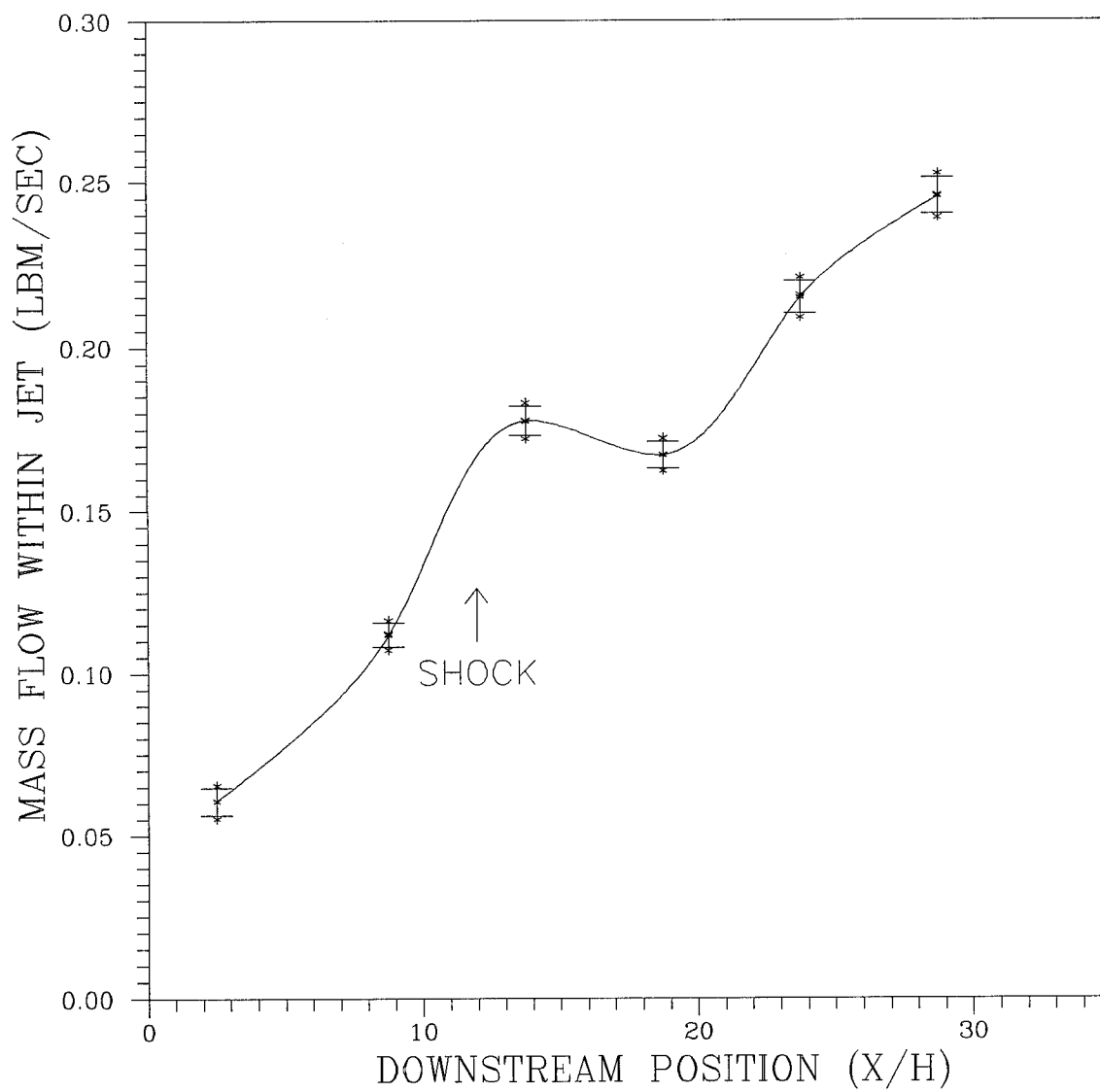


Figure VI-4: Mass flow within jet versus X/H for EPR 1.49

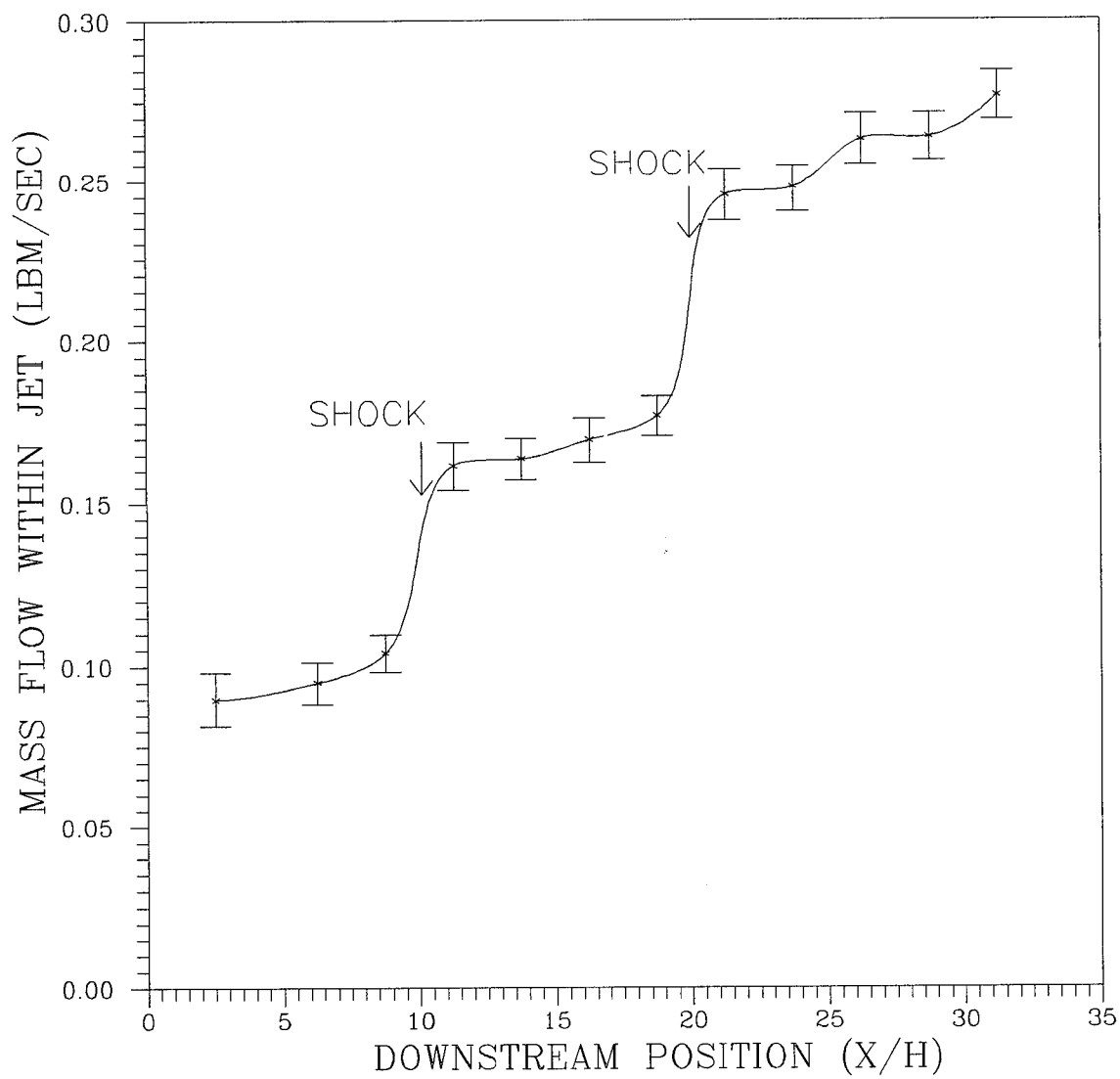


Figure VI-5: Mass flow within jet versus X/H for EPR 3.50

in EPRs 1.49 and 3.50 which occur near the SSLI locations. The steps are caused by additional mass being rapidly entrained into the jet by the vorticity generated during the SSLI leading to a jump in the mass flow within the jet boundaries. The steps are most prominent in EPR 3.50 where the SSLIs are the strongest and the relative vorticity generated is the greatest. Even with the possible errors encountered within this investigation, the steps shown in Figure VI-5 are larger than the error margin; thus, the steps are real and a product of the SSLI. The errors encountered in this study are typical for work of this type according to Schetz (63). Schetz indicated that errors on the order of 10 to 15 percent for measured mass entrainment are not uncommon. It is anticipated that with further development of the concentration probe the error band can be reduced significantly.

The measured entrainment rates were compared to theoretical values determined by Equation VI-3 developed for both supersonic and subsonic shear layers (49:4):

$$\frac{d\dot{m}}{dx} = C_1 \rho V_{\text{air}} \left| 1 - \frac{\rho V_{\text{He}}}{\rho V_{\text{air}}} \right| \quad (\text{VI-3})$$

$$C_1 \approx 0.01 - 0.02$$

The mass flux, ρV , was evaluated at the centerline of the helium jet and the centerlines of the upper and lower air streams. The coefficient C_1 is generally chosen to fit the data to the theory. The value for free shear layers is generally between 0.01 and 0.02. For ease of comparison C_1 was arbitrarily chosen as 0.01 and then adjusted to fit the data in this investigation. Two entrainment rates were evaluated: one using the upper air stream and

one using the lower air stream and then the two rates were averaged for a single entrainment rate along the jet. In order to compare the theoretical entrainment rates for shear layers to jets, the shear layer value must be doubled to account for entrainment from both sides of the jet. Equation VI-3 does not account for compressibility effects which occur at convective Mach numbers above 0.5; therefore a convective Mach number correction should be applied. The convective Mach number correction consisted of applying a multiplication factor to the entrainment rate that was: 1.0 if $M_{C1} < 0.5$, 0.3 if $M_{C1} > 1.0$; and linear between 1.0 and 0.3 if $0.5 \leq M_{C1} \leq 1.0$ as shown mathematically in Equation VI-4. This correction models the existing growth rate data for free shear layers with high convective Mach numbers and was suggested and used by Schetz (50:3).

$$f(M_{C1}) = \begin{cases} 1.0 & : M_{C1} < 0.5 \\ 1.7 - 1.4 \cdot M_{C1} & : 0.5 \leq M_{C1} \leq 1.0 \\ 0.30 & : M_{C1} > 1.0 \end{cases} \quad (VI-4)$$

The convective Mach number used in Equation VI-4 is the theoretical convective Mach number based on isentropic relations as given by Equation I-1 in Section I.1.1.

VI.2.1. Mass Entrainment Rates for EPR 0.89

The mass entrainment rate for EPR 0.89 (Fig. VI-3) was fairly constant along the duct with a slight drop off toward the end of the duct where the velocity ratio between the helium jet and the air stream approached unity. The mass entrainment rate, dm/dx , for EPR 0.89 was measured to be 0.40 lbm/(s-ft) for the linear portion ($10 < X/H < 26$). An average theoretical entrainment rate was determined using Equations VI-3 and VI-4 with a value of $C_1 = 0.01$ and doubling the results to account for entrainment from both sides of

the jet. The theoretical entrainment was determined to be 0.92 lbm/(s-ft). As can be seen the calculated value is approximately twice that of the measured value which indicates that the entrainment in a ducted flow is less than for a free jet. For an improved correlation between theory and data a value of $C_1 = 0.005$ should be chosen for confined jets similar to the EPR 0.89 test case.

VI.2.2. Mass Entrainment Rates for EPR 1.49

The mass entrainment rate for EPR 1.49 (Fig. VI-4) is not linear but appears to have linear regions; therefore for calculation purposes the mass entrainment curve is broken into four regions where the entrainment rate appears linear. The four regions are identified in Table VI-1 along with their measured and theoretical entrainment rates, convective Mach numbers, and relative vorticity generated during SSLIs. The theoretical entrainment rates shown in Table VI-1 were calculated using $C_1 = 0.01$ and doubled to account for entrainment from both sides of the jet. The theoretical entrainment rates with

Table VI-1: Entrainment Rates for EPR 1.49

Region Where Entrainment is Linear	Axial Location X/H	Measured $\frac{dm}{dX}$ $\left(\frac{\text{lbm}}{\text{s-ft}}\right)$	Calculated ¹ $\frac{dm}{dX}$ $\left(\frac{\text{lbm}}{\text{s-ft}}\right)$	Average Convective Mach Number M_{C1} ND	Calculated ² $\frac{dm}{dX} \cdot f(M_{C1(wg)})$ $\left(\frac{\text{lbm}}{\text{s-ft}}\right)$	Relative Vorticity Generated (1/S ²)
1	0-9	0.49	0.59	0.8	0.34	
2	9-14	1.08	0.60	0.4	0.60	3.5×10^{11}
3	14-19	-0.12	0.63	0.3	0.63	
4	19-30	0.47	0.64	0.1	0.64	

¹Eq. VI-3 using a value of 0.01 for C_1

²Eq. VI-3 x Eq. VI-4 using a value of 0.01 for C_1

the convective Mach number correction for regions 1 and 4 are close to the measured values. Region 1's theoretical value is 40% low and region 4's theoretical value is 40% high. Region 2 had the SSLI which generated vorticity and increased the entrainment rate 80% over the theoretical value. Figure VI-4 shows the entrainment rate for region 3 to be negative which is physically impossible but with the margin of error it could be zero which would be physically acceptable but it is still well below the calculated value of 0.63 lbm/(s-ft). The data used to determine the total mass flow within the jet boundaries were only taken along the duct centerline and as previously discussed the mass flow of helium across the duct was probably not uniform thus the negative entrainment rate is believed to be a result of flowfield non-uniformities. For EPR 1.49 the value of $C_1 = 0.01$ was a good choice for the regions without SSLI giving results both high and low along the jet. The entrainment theory used by Schetz (49) was developed without consideration of SSLI and therefore would not be expected to fit the data where SSLIs occur. The entrainment rate theory will be extended to account for enhanced entrainment due to SSLIs in Section VI.3.

VI.2.3. Mass Entrainment Rates for EPR 3.50

EPR 3.50 and EPR 1.49 both represent theoretical case III, the underexpanded case, thus the test cases have similar characteristics. EPR 3.50 has five linear regions with two containing SSLIs within the mixing duct. The five linear regions are identified in Table VI-2 along with their measured and theoretical entrainment rates, convective Mach numbers, and relative vorticity generated during SSLIs. As with Table VI-1 the value of constant C_1 used to calculate the theoretical entrainment rate was 0.01 and the

entrainment rates have been doubled to account for the entrainment from both sides of the jet. Regions 1, 3, and 5 show a measured entrainment rate considerably lower than the theoretical value even with the convective Mach number correction. To improve the theoretical entrainment rate predictions for regions 1, 3, and 5 a value of $C_1 = 0.003$ is recommended for this EPR.

Regions 2 and 4 have major SSLI taking place which boosts the entrainment rate considerably: a factor of 7.8 over the calculated value for region 2 and a factor of 4.5 for region 4. The entrainment rate theory is not valid in regions where there are SSLIs; thus the results of the calculations would not be expected to match the measured entrainment rates. A modification to the value of C_1 in Equation VI-3 is proposed that will extend the theory into regions with SSLIs in Section VI.3.

Table VI-2: Entrainment Rates for EPR 3.50

Region Where Entrainment is Linear	Axial Location X/H	Measured $\frac{d\dot{m}}{dX}$ $\left(\frac{\text{lbm}}{\text{s-ft}}\right)$	Calculated ¹ $\frac{d\dot{m}}{dX}$ $\left(\frac{\text{lbm}}{\text{s-ft}}\right)$	Average Convective Mach Number M_{C1} ND	Calculated ² $\frac{d\dot{m}}{dX} \cdot f(M_{C1(\text{avg})})$ $\left(\frac{\text{lbm}}{\text{s-ft}}\right)$	Relative Vorticity Generated (1/S ²)
1	0-9	0.14	0.65	1.2	0.20	
2	9-11	2.34	0.51	0.8	0.30	5.7×10^{12}
3	11-19	0.10	0.70	0.8	0.40	
4	19-21	3.27	0.72	0.5	0.72	1.6×10^{12}
5	21-30	0.19	0.65	0.4	0.65	

¹Eq. VI-3 using a value of 0.01 for C_1

²Eq. VI-3 x Eq. VI-4 using a value of 0.01 for C_1

The entrainment data obtained in this study indicate that confined jets entrain mass slower than free jets and shear layers thus a lower value of C_1 in Equation VI-3 should generally be used for confined jets. A value of $C_1 = 0.005$ is a good choice for confined jets with variable EPRs similar to those in this study when SSLI are not present. The range for C_1 in this study was between 0.01 and 0.003 when SSLI were not present with the baseline case (EPR 0.89) having a value of $C_1 = 0.005$.

It was observed that the high EPR case with multiple SSLI had the lowest entrainment rate along the shear layer between SSLIs. The low entrainment rate between SSLIs probably results from drastic changes in the flowfield due to the SSLIs. The entrainment data acquired was only on the duct centerline and the SSLI is most likely a three dimensional effect which could cause the lighter helium to be displaced laterally off the centerline. When the helium moved off the duct centerline, the jet (defined as the locus of points on the centerline where the helium molar concentration was > 0.3) would appear to grow slower and entrain less mass; with an apparent negative entrainment rate as seen in EPR 1.49. The three dimensional effects would be the greatest near the side walls where the wall boundary layer interacts with both the oblique shock and the shear layers. Further study will be required to confirm this observation.

VI.3. Shock-Shear Layer Interactions

The effects of SSLIs on the entrainment rate is dramatic as seen in the entrainment rate data of EPR 3.50 and to a lesser degree in EPR 1.49. The jump in entrainment due to the SSLI can be conceptualized as a vortex forming in the SSLI region that is pumping air into the helium jet. The vortex will grow then break off due to viscous actions of the

freestream and travel downstream as a large structure within the shear layer. A new vortex will form in the SSLI region and start the process over again. The strength of the vortex is proportional to the cross product of the density and pressure gradient vectors as given by Equation II-1. The vorticity generated in the three SSLIs in this study, calculated in the Chapter V, was used to correlate the enhanced entrainment observed. Table VI-3 shows the relative vorticity generated along with the jump in mass flow within the jet and the measured and calculated entrainment rates and their ratio. Data in the table shows that the jump in mass flow rate and the measured entrainment rate ($\frac{dm}{dx}$) do not correlate directly with vorticity generation indicating that there is more involved in the entrainment than the vorticity alone.

Table VI-3: Entrainment rates for SSLIs

Relative Vorticity Generated	Jump in Mass Flow Rate	Measured $\frac{dm}{dX}$	Calculated ¹ $\frac{dm}{dX} \cdot f(M_{Cl_{(avg)}})$	$\frac{\text{Measured}}{\text{Calculated}} \frac{dm}{dX}$	Exit Pressure Ratio (EPR)
(1/S ²)	$\left(\frac{\text{lbm}}{\text{s-ft}}\right)$	$\left(\frac{\text{lbm}}{\text{s-ft}}\right)$	$\left(\frac{\text{lbm}}{\text{s-ft}}\right)$	ND	ND
3.5×10^{11}	0.066	1.08	0.60	1.8	1.49
1.6×10^{12}	0.058	3.27	0.72	4.5	3.50
5.7×10^{12}	0.068	2.34	0.30	7.8	3.50

¹Eq. VI-3 x Eq. VI-4 using a value of 0.01 for C_1

Previously the entrainment rate was shown to be a function of the momentum ratio and the convective Mach number as given by Equations VI-3 and VI-4 thus the entrainment in the SSLI region should also be a function of these parameters. The next to last column in Table VI-3 shows that indeed the ratio of the measured to the calculated

entrainment rates do correlate with vorticity. The one problem associated with this correlation is that the value for the constant C_1 used to calculate theoretical entrainment rates varies from case to case thus it would be desirable to have a correlation that is not a function of the constant C_1 . A plot of C_1 versus vorticity (ζ) due to SSLIs is shown in Figure VI-6 where C_1 was calculated using Equation VI-5.

$$(C_1)_{\text{SSLI}} = \frac{\left(\frac{dm}{dX}\right)_{\text{Measured during SSLI}}}{\rho V_{\text{air}} \left| 1 - \frac{\rho V_{\text{He}}}{\rho V_{\text{air}}} \right|} \quad (\text{VI-5})$$

A power law function fits the data in Figure VI-6 nicely and is given by Equation VI-6.

$$(C_1)_{\text{SSLI}} = 1.6 \times 10^{-8} (\zeta)^{0.52} \quad (\text{VI-6})$$

Equation VI-6 allows a value of C_1 for SSLIs to be determined based on the vorticity generated during the SSLI as determined by the source term in Equation II-1 using the method outlined in Appendix C. Combining equations VI-3 and VI-6 gives the mass entrainment rate for a SSLI.

$$\frac{dm}{dx} = 1.6 \times 10^{-8} (\zeta)^{0.52} \rho V_{\text{air}} \left| 1 - \frac{\rho V_{\text{He}}}{\rho V_{\text{air}}} \right| \quad (\text{VI-7})$$

This is the first investigation that has determined a correlation function for the enhanced mass entrainment due to SSLIs. The studies on air-air shear layers and jets that looked for

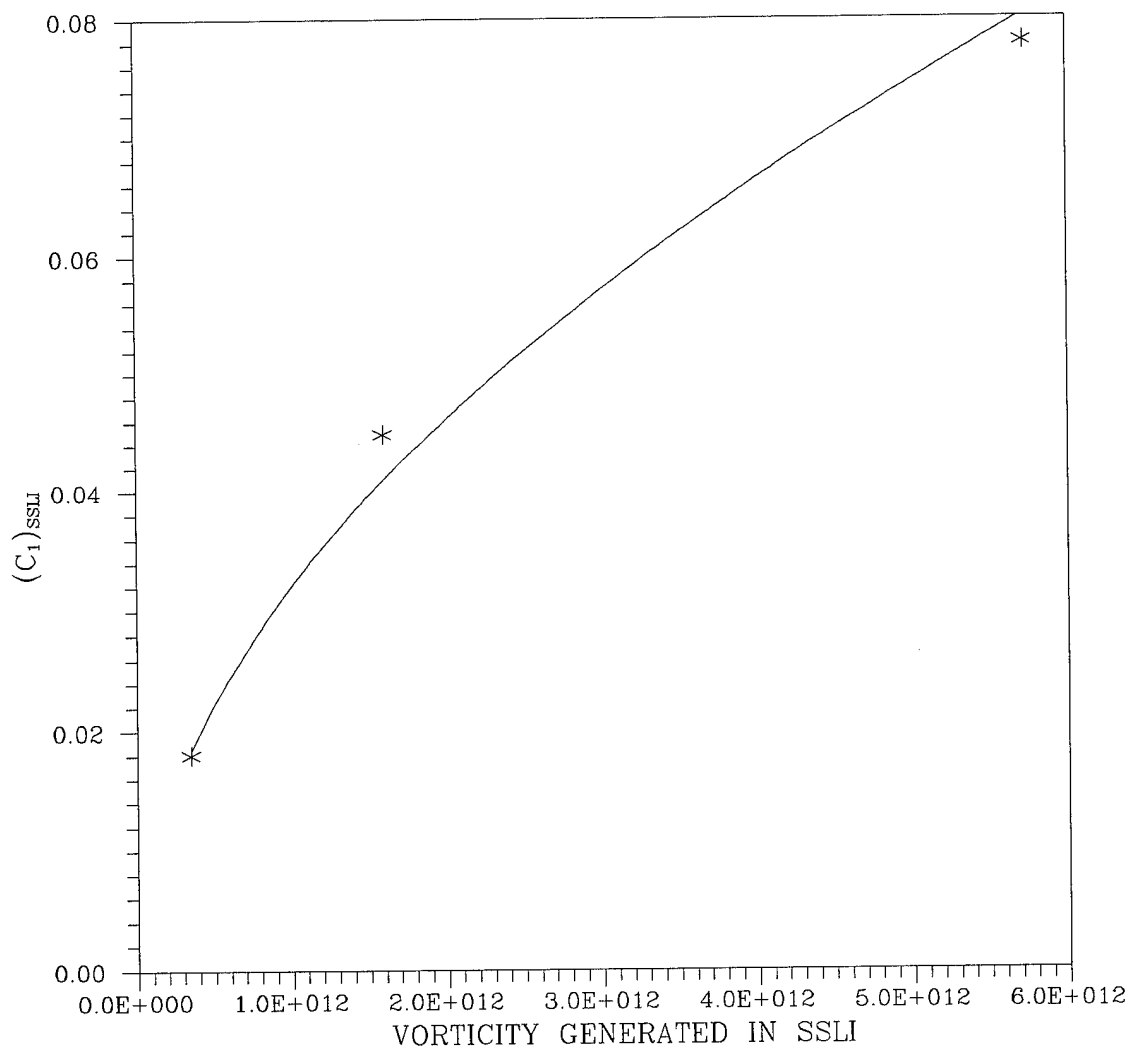


Figure VI-6: $(C_1)_{\text{SSLI}}$ versus vorticity generated by SSLI

mixing enhancement due to SSLI by Shau and Dolling (18) and Samimy et al (43) were unsuccessful due to the small density gradients across the air-air shear layers. The study by Menon (42) which investigated slot injection of helium at sonic velocities observed a mixing enhancement as determined by the growth of the shear layer during the SSLI but did not present any entrainment data nor did he present a correlation for the growth enhancement due to the SSLI. The investigation of SSLI should be extended to include a wider range of flow conditions (EPR, velocity ratio, convective Mach number, overall mixture ratio, geometry, shock strengths and density gradients) to confirm Equation VI-6 or establish a general correlation for flows with SSLIs.

During the SSLI the entrainment is significantly enhanced but the vorticity generated during the SSLI appears to reduce the entrainment downstream from the SSLI location. The entrainment rates between SSLIs for EPR 3.50 were all significantly lower than predicted. If EPR 0.89 is the baseline case for the entrainment within the duct and the value for C_1 is chosen to be 0.005 as observed in EPR 0.89, then the reduced entrainment between SSLIs can be correlated with the vorticity generated during SSLIs. Table VI-4 shows the measured entrainment rates, the calculated entrainment rates with $C_1 = 0.005$, and the entrainment rate errors for EPR 3.50.

Table VI-4: Entrainment rate errors for EPR 3.50

Region Where Entrainment is Linear	Axial Location X/H	Measured	Calculated ¹	ERROR (E _{SSLI})	Relative Vorticity Generated 1/S ²
		$\frac{dm}{dX}$ $\left(\frac{\text{lbm}}{\text{s-ft}}\right)$	$\frac{dm}{dX} \cdot f(M_{C_{1(\text{avg})}})$ $\left(\frac{\text{lbm}}{\text{s-ft}}\right)$	$\frac{\text{Measured-Calculated}}{\text{Measured}}$ ND	
1	0-9	0.14	0.10	0.29	
2	9-11	2.34	2.06	0.12	5.7×10^{12}
3	11-19	0.10	0.20	-1.00	
4	19-21	3.27	2.64	0.19	1.7×10^{12}
5	21-30	0.19	0.32	-0.68	

¹Eq. VI-3 x Eq. VI-4 using a value of 0.005 for C_1 except in regions 2 and 4 where $(C_1)_{\text{SSLI}}$ (Eq. VI-6) was used.

Figure VI-7 plots the absolute value of the entrainment rate error, E_{SSLI} , versus vorticity generated during the SSLI upstream of the region exhibiting reduced entrainment. A power law fit to the data in Figure VI-7 provides an estimate of the entrainment rate corrections needed to account for reduced entrainment after SSLIs (Eq. VI-8). A power law fit to the data was chosen because as the vorticity generated during the SSLI approaches zero then the error should approach zero.

$$E_{\text{SSLI}} = 8.58 \times 10^{-5} (\zeta)^{0.32} \quad (\text{VI-8})$$

The reduced entrainment rate after the SSLI should decay with distance downstream from the SSLI location but the current data is insufficient to predict the decay rate or the region that the reduced entrainment rate is confined to. This entrainment rate error correction should be used with caution as it was developed using the limited data available. The correction is based on a value of $C_1 = 0.005$ which provided a good fit to the baseline

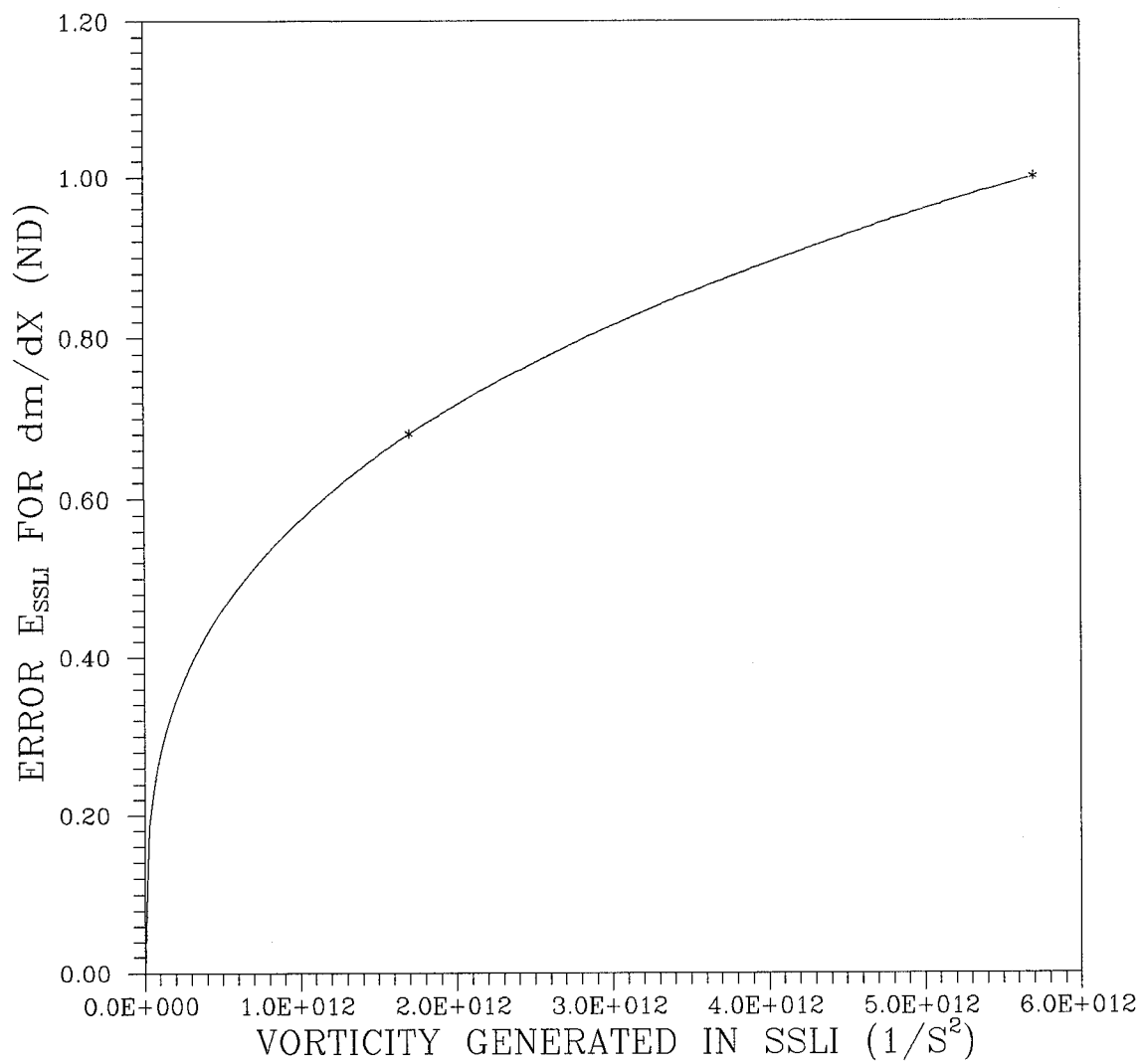


Figure VI-7: Entrainment rate error Vs. vorticity

case; EPR 0.89. Further investigations of the effects of SSLI generated vorticity on the entrainment downstream needs to be conducted to confirm Equation VI-8.

VI.4. Mixing Enhancement Due to Instability Modes

One of the postulates for this study was that the pressure waves reflect off the duct walls and excite the supersonic wall instability modes within the shear layers. This effect has been observed in numerical studies (35-38) but has not been confirmed experimentally. The entrainment rate data acquired in this study do not support the enhanced entrainment and mixing due to instability modes as observed in the computational studies. The entrainment rates measured in the absence of SSLIs for the three EPRs tested were generally less than the theoretical values for free shear layers, as seen by regions 1, 3, and 4 in Table VI-1 and regions 1, 3, and 5 in Table VI-2. The low entrainment rates appear to indicate there was negligible enhancement due to pressure waves reflecting off the walls and exciting the wall instability modes within the shear layers. The entrainment rate measurements in the vicinity of SSLIs indicated strong enhancement of mass entrainment which is better explained by the SSLI theory than the instability theory.

VI.5. Mixing Enhancement Due to Exit Pressure Ratio (EPR)

In order to evaluate the mixing as a function of EPR the DMR will be evaluated. The DMR was developed in Chapter II and given by Equation II-3. Figure VI-8 shows the DMR versus X/H for the three EPR cases investigated. Figure VI-8 shows that the high EPR case entrained 75 percent of the available air compared to 55 percent for the low EPR case tested. Over 50 percent of the mass entrained into the jet in the high EPR

case was due to the SSLIs. The location of the SSLIs that enhanced mass entrainment in the high EPR case are not only functions of the EPR (i.e. high EPR produce large turning angles thus stronger oblique shocks) but also functions of the ratio of jet height to duct height. If the ratio of jet height to duct height is decreased then the shocks will reflect off the walls further downstream (X/H). This will produce fewer SSLIs per jet height (H) down the duct leading to less entrainment. The entrainment rates between the SSLIs for the high EPR cases are believed to be low due to the high velocities and high convective Mach numbers across the shear layer caused by the expansion of the helium as it exits the nozzle (Ref. Table VI-2).

The low EPR cases entrained air at a relatively steady rate without relying on the large entrainment due to the SSLIs. The entrainment rate without SSLIs was higher for the low EPR cases because the velocity and convective Mach numbers were relatively low across the shear layer. The disadvantage of the low EPR was only a small percentage of the available air was entrained into the helium jet. If the goal of the fuel injector is to entrain the maximum amount of available inlet air into the fuel jet then a high EPR fuel jet is desirable with fuel injectors spaced close together in order to have a low jet height to duct height ratio thus a large number of shock interactions with the fuel jet to improve entrainment.

VI.6. Summary

- The binary gas probe provided a means of calculating the mass flux across the duct from which the mass flow within the helium jet could be calculated. From the mass

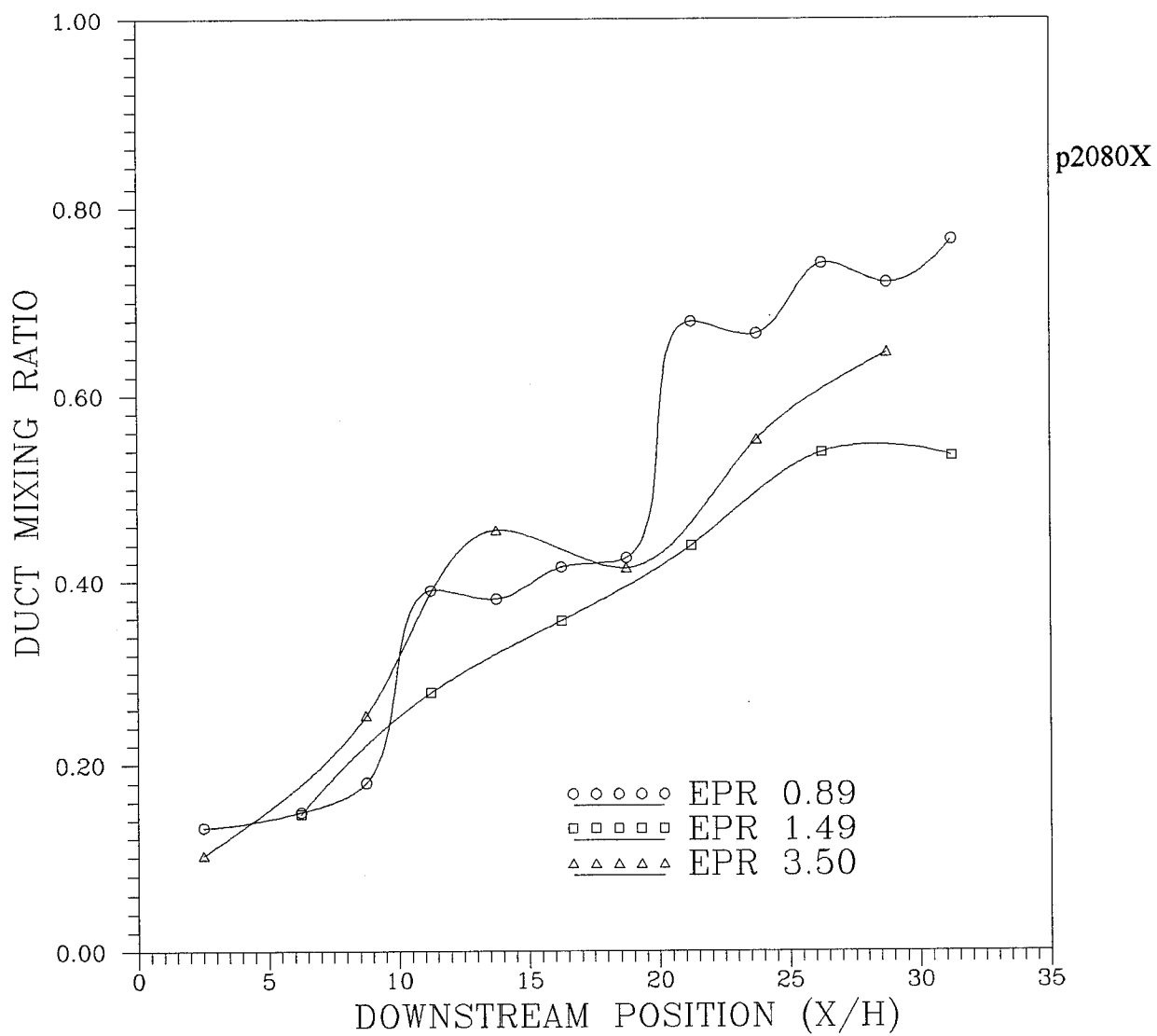


Figure VI-8: Duct mixing ratio versus X/H

flow data the rate at which mass was being entrained into the helium jet could be determined.

- The mass entrainment rate was significantly increased in the vicinity of SSLIs when there was a strong density gradient across the shear layers making up the jet.
- The enhanced mass entrainment caused by the SSLI is a function of not only the vorticity generated by the SSLI but also the momentum ratio across the shear layer and is given by:

$$\frac{dm}{dx} = 1.6 \times 10^{-8} (\zeta)^{0.52} \rho V_{air} \left| 1 - \frac{\rho V_{He}}{\rho V_{air}} \right|$$

- Mass entrainment was not enhanced, to any measurable degree, by the excitation of the wall instability modes by reflections of the pressure waves from the duct walls as predicted in numerical studies by Greenough et al. (36) and Tam and Hu (37).
- High EPR led to improved overall mixing compared to the baseline case with an EPR near unity. The high EPR caused low mass entrainment along the jet shear layers due to high convective Mach numbers and velocity ratios, but the high EPR also caused oblique shocks to form which reflected off the duct walls and intersected with the jet several times causing significant mass entrainment due to numerous SSLIs. The end result was a higher percentage of the available air mixing with the helium for the geometry tested.

VII. Proposed Model

The results presented in Chapter V and VI show that high exit pressure ratios and shock shear layer interactions affect the flowfield and the rate of entrainment. Some of the important information needed to design SCRAMJET combustors, such as where the combustion and heat release take place, is associated with mixing and entrainment. This section will summarize and discuss how the new information on entrainment, presented in this study, can be applied to the analysis of SCRAMJET engines. This investigation showed that entrainment of air into fuel, modeled using helium, can be significantly improved by operating underexpanded fuel injectors with high exit pressure ratio's in order to take advantage of the enhanced mixing due to SSLIs.

VII.1. Basic Model

In order to analyze the mixing of confined fuel jets with EPRs between 0.89 and 3.50 (this is the range for the data presented, use caution outside this range) it is necessary to determine where the shear layers are located, where the jets potential core ends and to what extent the air is entrained into the fuel. The theory in Chapter II shows that for high EPR's there is a diamond shock and expansion pattern within the duct, as well as within the fuel jet, caused by the underexpanded fuel jet rapidly expanding as it exits the nozzle. The shock pattern locations and shock strengths can be determined using simple wave theory or the method of characteristics. The location of the end of the jet's potential core, which is a function of the exit pressure ratio and the entrainment, can be estimated using Equation V-4 subscripted for fuel/air mixtures.

$$\left(\frac{L_{pc}}{H}\right) = 2.336 \left(\frac{P_{fuel}}{P_{air}}\right) + 3.037 \quad (VII-1)$$

Equation VII-1 was developed from the three test cases in this investigation thus it is limited to the range of EPRs from 0.89 to 3.5 and a ratio of jet height to duct height of 0.17. Within this range Equation VII-1 predicted the potential core length within 5% of the measured values which for an equation that does not explicitly take into account the entrainment or geometry is very good.

With an estimate of the jet's potential core known the centerline decay rate can be determined. It was found, in this investigation, that the centerline helium concentration decay for all the cases investigated could be defined by one equation regardless of the EPR. Equation V-3 defines the centerline helium mass concentration after the end of the helium jet's potential core for exit pressure ratios between 0.89 and 3.50. Equation VII-2 expresses Equation V-3 for all X for use in the model.

$$\bar{C}_{mass} = \frac{(C_{mass} - C_{FM})}{(1.0 - C_{FM})} = \begin{cases} 1 & \text{If } X < L_{PC} \\ \left(\frac{X}{L_{PC}}\right)^{-1.63} & \text{If } X \geq L_{PC} \end{cases} \quad (VII-2)$$

The two parameters in Equation VII-2, that define the centerline decay are the helium mass concentration parameter \bar{C}_{mass} defined in Chapter V by Equation V-2 and the ratio of axial distance to potential core length, (X/L_{PC}) . Equation VII-2 will provide a first order estimate of the centerline helium concentration which can be used to determine the gas properties needed to calculate velocities, densities, and Mach numbers along the duct

centerline. With the centerline properties of the jet known simple entrainment models can be used to calculate the air entrained into the fuel jet.

In order to calculate a local rate of entrainment along the jet boundaries the entrainment model used by Schetz (49, 50) may be used. Schetz's entrainment rate equation with fuel and air nomenclature is given by Equation VII-3.

$$\frac{d\dot{m}}{dx} = C_1 \rho V_{\text{air}} \left| 1 - \frac{\rho V_{\text{fuel}}}{\rho V_{\text{air}}} \right| \quad (\text{VII-3})$$

$$C_1 \approx 0.01 - 0.02$$

Schetz (50) found this equation to be adequate for slot injected flows with convective Mach numbers less than 0.3 and EPRs between 0.8 and 1.25 when the value of C_1 was 0.02. For convective Mach numbers above 0.5, Equation VII-3 needs to be modified to account for the reduced entrainment at high convective Mach numbers. The modification is discussed in Section VI.2. and is given by Equation VI-4. This study found that a value of $C_1 = 0.005$ gave results that were within 15 percent for EPR 0.89, the baseline case, when applied to the measured velocity and density data. The enhanced entrainment during the SSLI and the reduced entrainment after the SSLI are not accounted for by Equation VII-3. The jump in mass entrainment for $\text{EPR} > 1$, shown as step increases in mass flow within the jet at shock locations in Figures VI-4 and VI-5, was caused by a significant increase in vorticity generation due to SSLI. To account for this enhanced entrainment a correlation between the vorticity generated by the SSLI and the value for C_1 was developed and is given by Equation VI-6, repeated for convenience:

$$(C_1)_{\text{SSLI}} = 1.6 \times 10^{-8} (\zeta)^{0.52} \quad (\text{VI-6})$$

where ζ is the relative vorticity generated by the SSLI, calculated using Equation VII-4.

$$\zeta = \frac{\nabla P \times \nabla \rho}{(\bar{\rho})^2} \sin \Theta \quad (\text{VII-4})$$

In Equation VII-4 ∇P is the pressure gradient across the shock and $\nabla \rho$ and $\bar{\rho}$ are the density gradient and average density across the shear layer respectively. The pressure gradient across the shock is determined from the pressure jump across the shock and the shock thickness as determined from weak shock theory. The density gradient across the shear layer is calculated from the centerline properties of the jet, the jet boundary properties, and the shear layer thickness immediately before the SSLI (see Appendix C for details).

To account for the reduced entrainment observed after the SSLI an error factor was determined that could be used to correct the calculated values of the mass entrainment after the SSLI. The error factor is calculated by Equation VI-7 based on the vorticity generated during the SSLI. Without the error correction the entrainment rate equation gives results within a factor of 2. The error correction reduced the error to less than 30 percent. The difference between the measured and calculated entrainment rates between SSLIs is not considered serious since the air entrainment into the jet occurs predominantly at the SSLI.

With the entrainment rate known for the jet and shear layers at the SSLIs and between the SSLIs all the pieces are known to perform a simple analysis of the

entrainment of air into a fuel jet with and without the fuel jet exit pressure matched to the inlet air pressure. In order to perform the mass entrainment analysis on the jet, the outer flowfield (particularly the location where the shocks intersect the shear layers) must be known from potential flow theory, method of characteristics or simple wave theory. In order to calculate the entrainment into the two shear layers that form the jet the entrainment rate equation (Eq. VII-2) must be integrated from the nozzle exit plane to the end of the duct. The term shear layer in the following discussion not only refers to the actual shear layers that separates the helium (fuel) jet's potential core from the outer flowfield but also to the shear layer that is formed by the jet centerline properties and the outer flowfield after the end of the jet's potential core. The integration of the entrainment rate along the jet can be performed by a marching integration technique along the shear layer using an estimate of the nozzle wall boundary layer thickness just prior to separation at the nozzle exit plane as the initial condition for the marching technique (50). For the regions where a SSLI occurs the value of C_1 should be calculated from Equation VI-6. The SSLI region starts at the point where the shock enters the shear layer/jet and ends at the point where the shock exits the shear layer/jet. To use Equation VI-6 the vorticity must be calculated from Equation VII-3 which requires the pressure and density gradients, and the average shear layer density. It should be noted that in some cases, such as single fuel injectors within a confined duct with EPRs near unity (i.e. EPR 0.89 test case), there will not be significant SSLIs therefore the value of C_1 can be kept a constant 0.005 for the entire calculation.

VII.2. Application of Model to EPR 3.50

As an example this analysis was applied to the initial conditions of the EPR 3.50 test case. The flowfield calculated from simple wave theory presented in Section V.1.3. was used for the inviscid solution to determine the location of the shocks and the shear layer. The helium-air shear layer was divided into regions with constant properties. The regions are shown in Figure VII-1. The regions between 0-1, 2-4 and 6-8 contain SSLIs thus the value of C_1 will be calculated from Equation VI-6 for these regions. The value of C_1 in the remaining regions will be held constant at 0.005 as previously recommended.

In order to calculate $(C_1)_{\text{SSLI}}$ from Equation VI-6 the relative vorticity needs to be calculated from Equation VII-4. The pressure gradients were calculated from the pressure jump across the shock and the shock thickness as calculated from shock thickness theory. The density gradient was calculated from the density change across the shear layer as determined from the inviscid flow analysis and from an estimate of the shear layer thickness, because the inviscid calculation of the shear layer thickness is zero. The shear layer thickness for the SSLI at the end of the nozzle was estimated from the experimental data presented in Section III.4. on facility performance as 3 times the boundary layer displacement thickness of the air jet or 0.15 in. The shear layer thickness at the SSLI in region 2-4 was estimated assuming a constant shear layer growth rate of 0.06 in/in. The shear layer growth rate was determined by dividing half the width of the jet at the end of the potential core (as determined from Equation V-4) by the length of the shear layer from the nozzle exit to the end of the potential core. For the SSLIs after the end of the potential core the shear layer width was assumed to be half of the jet width at the location

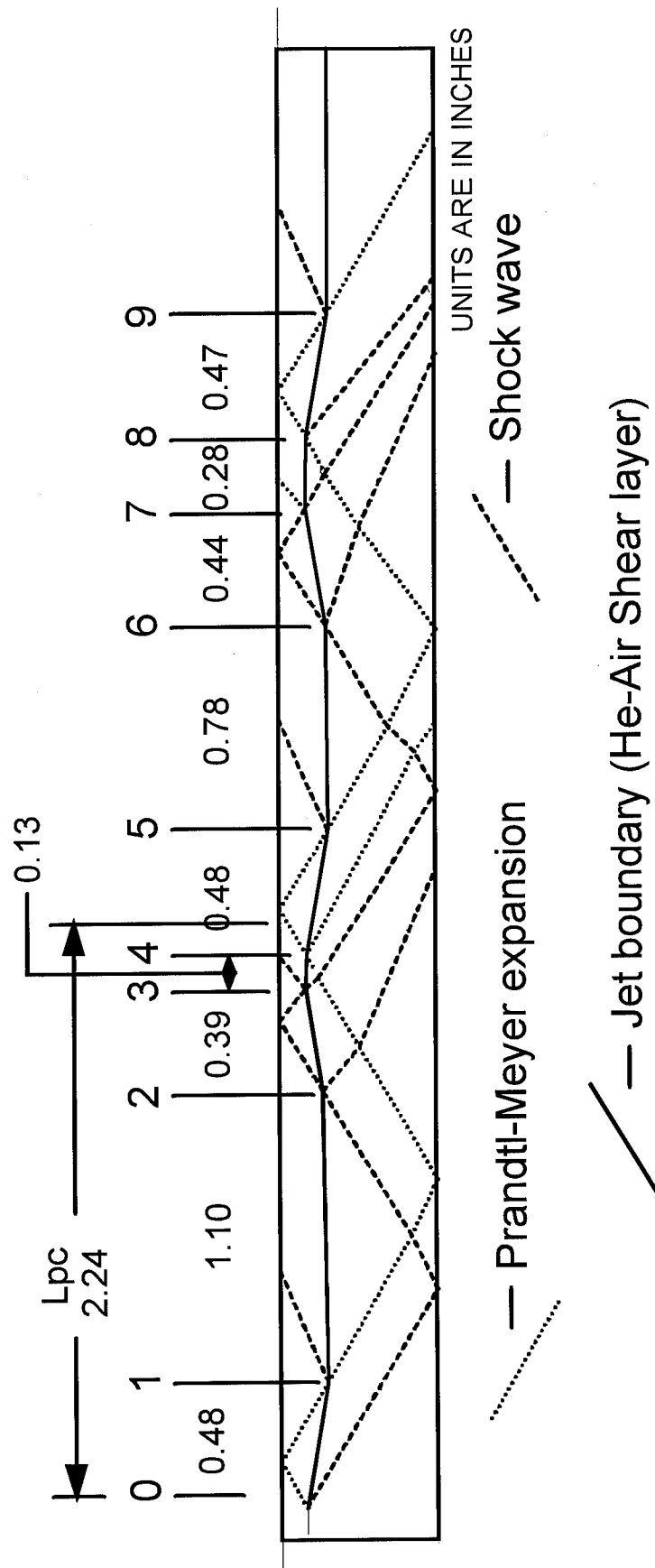


Figure VII-1: Inviscid flowfield analysis of EPR 3.50

of the SSLI. With the pressure and density gradients known the vorticity can then be calculated using the method in Appendix C.

The constants $(C_1)_{\text{SSLI}}$ for the SSLI regions were calculated from Equation VI-6. They were then used in Equation VII-3 to calculate the entrainment rates for each region. The results of this analysis are shown in Figure VII-2. The analysis produced the desired shape but, as can be seen in Figure VII-2, the calculated mass flow within the jet is lower than the experimental data. If the constant, C_1 , is arbitrarily scaled by 1.7 (i.e. $C_1 = 0.009$ for non SSLI regions and $C_{1\text{SSLI}} = 2.9 \times 10^{-8} (\zeta)^{0.52}$ for regions with SSLI) then the model fits the data nicely (Figure VII-2). It is interesting to note that the adjusted value of C_1 for non-SSLI regions is now close to the accepted value of 0.01 to 0.02 as given by Schetz (49:4).

This simple model illustrates how the data in this study could be applied to a problem in order to calculate the mass entrainment between light and heavy gases with and without SSLIs. The discrepancy between the actual and the calculated mass entrainment is due to both the simplicity of the wave model used for the potential flowfield prior to applying the entrainment rate equations and the limited data used to develop the constant, C_1 , for the entrainment rate equations. If a more refined model is used for the potential flowfield prior to applying the entrainment rate equations then better results would be expected. The best results would be achieved if the entrainment rate equations were integrated into a potential flow model thus allowing the effects of the mass entrainment and SSLI to impact the inviscid flowfield. Once the model is developed it must be benchmarked, with experimental data, if a high degree of accuracy is required.

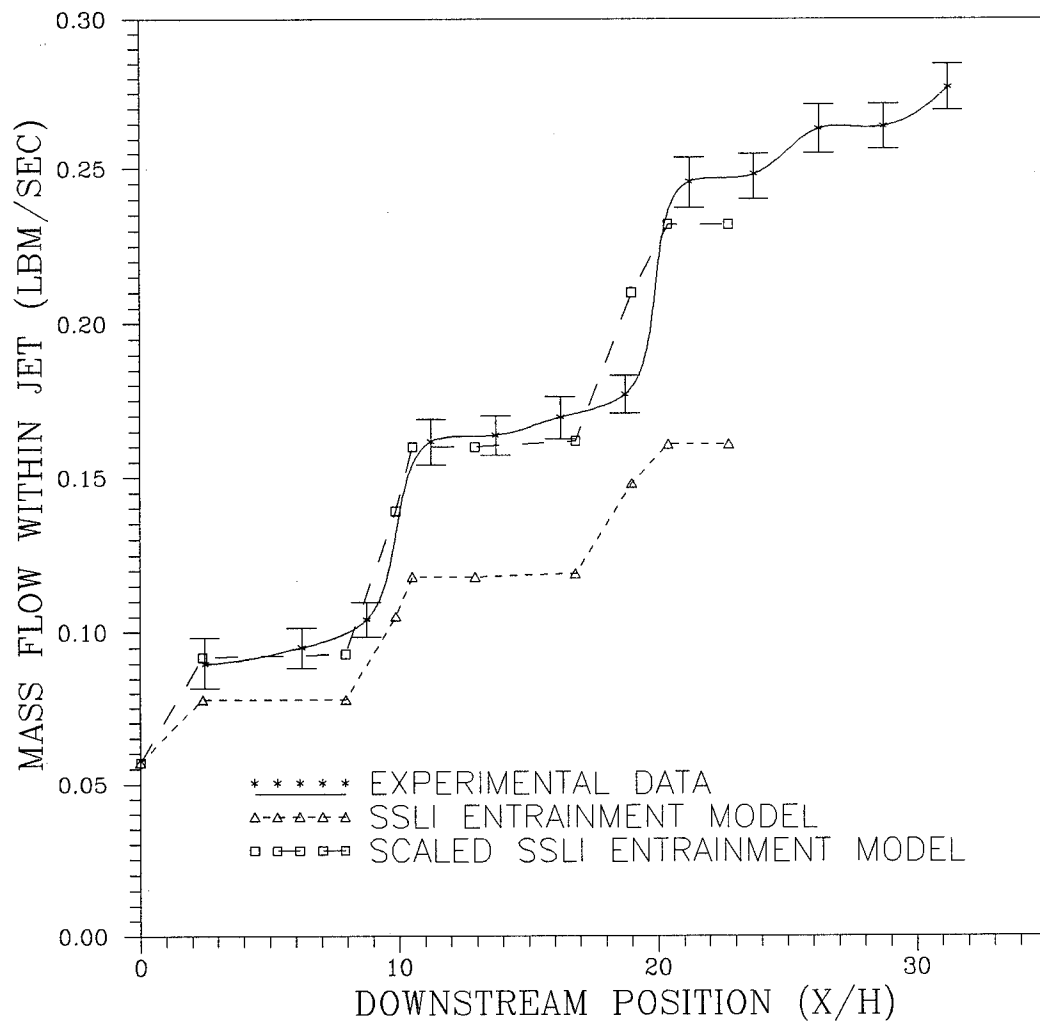
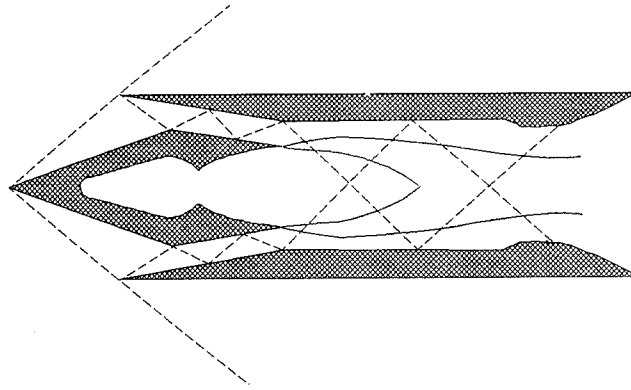


Figure VII-2: Mass flow within jet; model versus experiment

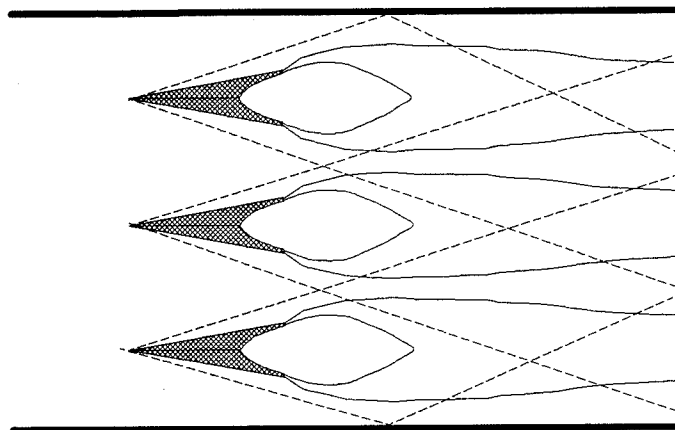
VII.3. Additional Applications of Model

The configuration studied in this investigation was a single injector within a confined duct, but the data obtained and the analysis proposed can be extended to multiple injectors by assuming that the symmetry lines between adjacent injectors are the duct walls in our model. The information presented in this study can also be applied to SSLI caused by shocks generated from the air inlet operation or by shocks generated from the fuel injectors themselves (Fig. VII-3 a & b). Investigations into the best way of employing the enhanced entrainment due to SSLI and high EPR to SCRAMJETs need to be conducted. Additional studies also need to investigate the trade off between the enhanced mixing due to SSLIs and the total pressure loss encountered from the shocks on the overall performance of the SCRAMJET.

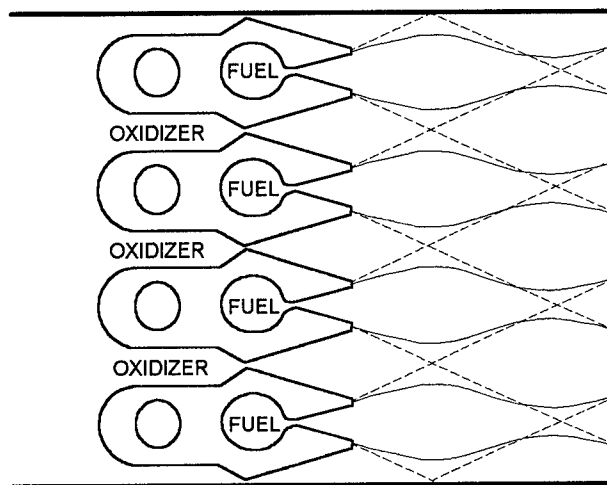
The previous discussions have primarily centered on the mass entrainment between fuel and air as would be found in a SCRAMJET combustor but much of the information in this study can be applied to the mixing of reactants in a supersonic flowing chemical laser. In the laser the shocks would be generated from the grid nozzles that are used to inject the fuel and oxidizer into the optical cavity where the reaction takes place to generate the excited laser molecules (Fig VII-3 c). Before the SSLIs are used to enhance the mixing in a chemical lasers additional investigations that examine the trade off between the enhanced mixing and the degradation in laser beam quality, due to enhanced turbulence and vorticity levels, need to be conducted.



a: SCRAMJET Inlet shocks generating SSLIs



b: Fuel injectors generating shocks and SSLIs



c: Laser grid nozzle generating SSLIs

Figure VII-3: Applications of enhanced mixing due to SSLIs

VIII. Conclusions and Recommendations

This study experimentally investigated the effects of varying the exit pressure of a supersonic helium jet exhausting coaxial with two supersonic air streams into a constant area duct. The effect an oblique shock had on the mass entrainment of air into the helium jet, when the shock interacted with the variable density shear layer separating the helium jet from the air streams, was also investigated. This topic was chosen because of the lack of information on the mixing of confined heterogeneous jets and the interaction of shocks with variable density free shear layers.

VIII.1. Conclusions

The most significant conclusion was that the interaction of oblique shocks with a variable density shear layer caused the mass entrainment rate across the shear layer to be enhanced. The mass entrainment rate was significantly increased in the vicinity of SSLIs when there was a strong density gradient across the shear layers making up the jet. The enhanced mass entrainment caused by the SSLI is a function of not only the vorticity generated by the SSLI, but also the momentum ratio across the shear layer.

Operating in an underexpanded condition with a high EPR improved overall mixing compared to the baseline case. The high EPR caused low mass entrainment along the jet shear layers due to high convective Mach numbers and velocity ratios, but the high EPR also caused oblique shocks to form which reflected off the duct walls and intersected the jet several times causing significant mass entrainment due to SSLIs. The end result

was a higher percentage of the available air mixing with the helium for the geometry tested.

The SCRAMJET engine can exploit the mixing enhancement due to the SSLI by operating the fuel injectors at a high EPR to generate shocks or by tailoring the shocks form from the engine's inlet to interact with the fuel jets. The mixing within the SCRAMJET combustor could be significantly enhanced using this technique because of the large density gradients generated between the low density hydrogen fuel and the higher density air.

The chemical laser could also exploit this technique for mixing enhancement by operating alternating grid nozzles at high exit pressure ratios in order to generate shocks and expansion waves that will intersect the shear layers and enhance mixing. This effect would be extremely effective if the density across the shear layers between nozzles is large as in the hydrogen-fluorine laser. Before mixing enhancement techniques employing SSLIs can be applied to lasers, investigations into the effects of enhanced turbulence due to SSLIs on laser beam quality must be conducted.

The binary gas concentration probe developed for this investigation was an invaluable piece of instrumentation. The probe permitted simultaneous measurements of all parameters needed to determine the local helium concentration in the flow, which represents a significant improvement over prior instrumentation. The probe was designed and calibrated to measure concentrations of helium in a binary gas but it also provided the necessary data to calculate mass flux values which could be integrated to provide mass entrainment data. During the calibration of the probe it was found that the relationship

between the Nusselt, the Reynolds and the Prandtl numbers (King's Law) used to calibrate hot wire sensors was insufficient for binary gas mixtures. A new term was added to King's Law that explicitly took into account the gas mixture. The improved King's Law for binary gases (Eq. IV-18) correlated the calibration data very well and provided data with helium molar fraction errors less than 0.05 across the entire flowfield

Two new parameters were developed to quantify the effects of high EPR on the flowfield. The first parameter was used to correlate centerline mass concentration data of confined jets with the data from free jets. This new parameter takes into account the limited air within the duct available for mixing and the fact that the centerline concentration never decays to the freestream concentration value.

The second parameter developed was the duct mixing ratio (DMR) which was used to quantify the degree to which the inlet air was entrained into the helium jet. The DMR is superior to the previously used entrainment ratio (ER) because it accounts for the limited inlet air within confined ducts and measures entrainment as a percentage of the inlet air.

VIII.2. Recommendations

New information dealing with the entrainment between supersonic heterogeneous jets has been established, but of equal importance, many new questions have arisen that need further investigation. The following is a partial list of topics that need further study:

1. An additional study focusing on the effect of oblique shocks on variable density shear layers. This study should be a parametric investigation that looks at large variations in both shock strength and density ratio across the shear layer. The study should observe

whether large density gradients or large pressure gradients (shock strength) are better for enhanced mass entrainment when the vorticity generation during SSLI remains constant.

2. An investigation into the helium distribution across the span of the duct. The data in the current investigation was acquired only along the duct centerline and it appeared from the continuity check of the helium that the helium distribution across the span of the duct may not be uniform. A mapping of the helium concentration in the duct's cross section would confirm non-uniformities of helium across the span of the duct and provide insight into the three dimensionality of the SSLI. This study could also provide insight into why the entrainment rate after the SSLI appeared to be lower than predicted by the entrainment rate theories.

3. An optical study using a high speed camera to investigate the dynamics of the SSLI to determine what the mechanism is that is enhancing mass entrainment into the shear layer. This study could confirm whether the vortex forms and remains stationary, pumping fluid into the shear layer or whether it forms then moves downstream while a new vortex forms. The optical study could also investigate the dynamics of large structures within the shear layer and the part they play in the mass entrainment process in supersonic flows. Unsteady shock effects on the SSLI and mass entrainment should also be investigated.

4. A series of numerical investigation that closely simulates the experimental conditions in this and follow on studies should be initiated. The numerical studies should utilize adaptive grid techniques to capture the details of the SSLI in order to determine the

details of the interaction. The results of the numerical studies should be used to develop follow on experimental investigations.

5. An investigation that examines improvements in the calibration and design of the binary gas probe should be conducted. The concentration probe developed in this study worked well but it could be improved if the internal gasdynamics and heat transfer were better understood. During the calibration of the probe a new term was added to King's Law to correlate the calibration data. The physical significance of this new term should be understood once the gasdynamics and heat transfer of the probe are understood. Both analytical and experimental investigations should be conducted to analyze the workings of the probe. A numerical study would also be useful in predicting the variation in performance as various designs are investigated. Calibration techniques need to be developed that would improve the accuracy of the probe's mass flow measurements. The probe was used in this study to calculate mass entrainment rates but, because the probe was never calibrated for mass flow the true error margins are unknown.

6. Design studies on how to best apply the enhanced mass entrainment due to SSLIs to SCRAMJET combustors.

7. Experimental studies to investigate the effects of vorticity and turbulence generated by SSLIs on laser beam quality. This study should lead to design studies on how to best apply mixing enhancement due to SSLIs to chemical lasers.

Bibliography

1. Walton, James T., "An Overview of Airframe Integrated Scramjet Cycle Components and Flow Features", NASP Technical Memorandum 1029, NASA Ames Research Center, November 1988.
2. Waltrup, Paul J., Griffin Y. Anderson, and Frank D. Stall, "Supersonic Combustion Ramjet (SCRAMJET) Engine Development in the United States", AIAA paper 76-042, 1976.
3. Ferri, A., "Review of SCRAMJET Propulsion Technology", Journal of Aircraft V.5 N.1 P.3-10, Jan-Feb 1968.
4. Curran, E.T., John L. Leingang and Wayne A. Donaldson, "A Review of High Speed Airbreathing Propulsion Systems", Paper presented at the Eighth International Symposium on Air Breathing Engines June 15-19, 1987, Cincinnati, Ohio.
5. Jacques, M.T., R. Payne, and J. Swithenbank, "Studies Leading to the Realization of Supersonic Combustion in Propulsion Applications", HIC Report 174, June 1972.
6. Swithenbank, J., F. Boysan, C.R. Ewan, L. Shao, and Z.Y. Yang, "Mixing Problems in Supersonic Combustion", Paper presented at the U.S. - France Workshop on Turbulent Reactive Flows July 1987.
7. Stull, F.D., "Scramjet Combustion Prospects", Astronautics and Aeronautics, p. 48-52, December 1965.
8. Ferri, A., "Supersonic Combustion Progress", Astronautics and Aeronautics, p. 32-37, August 1964.
9. Northam, G.B., I. Greenberg, and C.S. Byington, "Evaluation of Parallel Injector Configurations for Supersonic Combustion", AIAA/ASME/SAE/ASEE 25th Joint Propulsion Conference. Paper No AIAA-89-2525. American Institute of Aeronautics and Astronautics, Washington D.C., July 1989.
10. Grohs, G. and G. Emanuel, "Chapter 5: Gas Dynamics of Supersonic Mixing Lasers" Handbook of Chemical Lasers edited by R.W. Gross and J.F. Bott, John Wiley and Sons, New York, NY, 1976.
11. Thomas, R.H., J.A. Schetz and F.S. Billig, "Gaseous Injection in High Speed Flow", Paper presented at the Ninth International Symposium on Air Breathing Engines Athens Greece September 3-8 1989.

12. Curran, E.T., Personal Communications between January 1987 and December 1989.
13. Schadow, K.C., E. Gutmark and K.J. Wilson, "Passive Mixing Control in Supersonic Coaxial Jets at Different Convective Mach Numbers", AIAA 2nd Shear Flow Conference. Paper No AIAA-89-0995. American Institute of Aeronautics and Astronautics, Washington D.C., March 1989.
14. Wilson, K.J., E. Gutmark, E. Ajdari, K.C. Schadow and R.A. Smith, "Mixing Characteristics of Supersonic Shrouded Jets", 26TH Aerospace Sciences Meeting. Paper No AIAA-88 0699. American Institute of Aeronautics and Astronautics, Washington D.C., January 1988.
15. Amatucci, V.A., J.C. Dutton, and A.L. Addy, "Pressure Recovery in a Constant-Area, Two Stream Supersonic Diffuser", AIAA Journal V.20,N.9 p1308-1309, September 1982.
16. Dutton, J.C., C.D. Mikkelsen and A.L. Addy, "A Theoretical and Experimental Investigation of the Constant Area, Supersonic-Supersonic Ejector", AIAA Journal V.20 N.10 p.1392-1400 October 1982.
17. Fabri, J. and J. Paulon, "Theory and Experiments on Supersonic Air-To-Air Ejectors", NACA Technical Memorandum 1410, 1956.
18. Shau, Y.R. and D.S. Dolling, "Experimental Study of Spreading Rate Enhancement of High Mach Number Turbulent Shear Layers", AIAA/ASME/SAE/ASEE 25th Joint Propulsion Conference. Paper No AIAA-89-2458. American Institute of Aeronautics and Astronautics, Washington D.C., July 1989.
19. Kwok, F.T., P.L. Andrew, N.G. Ng and J.A. Schetz, "Experimental Investigation of a Supersonic Shear Layer with Slot Injection of Helium", 28TH Aerospace Sciences Meeting. Paper No AIAA-90-0093. American Institute of Aeronautics and Astronautics, Washington D.C., January 1990.
20. Birch, S.F. and J.M. Eggers, "A Critical Review of the Experimental Data For Developed Free Turbulent Shear Layers", Free Turbulent Shear Flows Volume I - Conference Proceedings, NASA SP-321, National Aeronautics and Space Administration, Washington D.C., 1973.
21. Rudy and Birch, Journal of Spacecraft and Rockets V.11, p.348 1974.
22. Bogdanoff, D.W., "Compressibility Effects in Turbulent Shear Layers", AIAA Journal V. 21 N.6 P.926-927, June 1983.

23. Chinzei, N., G. Masuya, T. Komuro, A. Murakami, and K. Kudou, "Spreading of Two-Stream Supersonic Turbulent Mixing Layers", Physics of Fluids V.29 N.5 P.1345-1347, May 1986.
24. Papamoschou, D., Experimental Investigation of Heterogeneous Compressible Shear Layers, Phd. Dissertation California Institute of Technology 1986.
25. Papamoschou, D., "Structure of the Compressible Turbulent Shear Layer", 27TH Aerospace Sciences Meeting. Paper No AIAA-89-0126. American Institute of Aeronautics and Astronautics, Washington D.C., January 1989.
26. Brown, G.L. and A. Roshko, "On Density Effects and Large Structures in Turbulent Mixing Layers", Journal of Fluid Mechanics, V.64 Part 4, P.775-816, 1974.
27. Messersmith, N.L., S.G. Goebel, W.H. Frantz, E.A. Krammer, J.P. Renie, J.C. Dutton, and H. Krier, "Experimental and Analytical Investigations of Supersonic Mixing Layers", 26TH Aerospace Sciences Meeting. Paper No AIAA-88-0702. American Institute of Aeronautics and Astronautics, Washington D.C., January 1988.
28. Walker, D.A., R.L. Campbell, and J.A. Schetz, "Turbulence Measurements for Slot Injection in Supersonic Flow", 26TH Aerospace Sciences Meeting. Paper No AIAA-88-0123. American Institute of Aeronautics and Astronautics, Washington D.C., January 1988.
29. Clemens, N.T. and M.G. Mungal, "Two- and Three-Dimensional Effects in the Supersonic Mixing Layer", AIAA/ASME/SAE/ASEE 26th Joint Propulsion Conference. Paper No AIAA-90-1978. American Institute of Aeronautics and Astronautics, Washington D.C., July 1990.
30. Ikawa, H. and T. Kubota, "Investigation of Supersonic Turbulent Mixing Layer with Zero Pressure Gradient", AIAA Journal V.13 N.5 p.566-572, May 1975.
31. Papamoschou, D. and A. Roshko, "The Compressible Turbulent Shear Layer: An Experimental Study", Journal of Fluid Mechanics, V.197 p. 453-477, 1988.
32. Samimy, M. and Elliott, G.S., "Effects of Compressibility on the Structure of Free Shear Layers", AIAA/ASME/SAE/ASEE 24th Joint Propulsion Conference. Paper No AIAA-88-3054A. American Institute of Aeronautics and Astronautics, Washington D.C., January 1989.
33. Dimotakis, P.E., "Turbulent Free Shear Layer Mixing", 27TH Aerospace Sciences Meeting. Paper No AIAA-89-0262. American Institute of Aeronautics and Astronautics, Washington D.C., January 1989.

34. Oertel, H., "Coherent Structures Producing Mach waves Inside and Outside of the Supersonic Jet", Structure of Complex Turbulent Shear Flow IUTAM Symposium Marseille 1982, Editors: R. Dumas and L. Fulachier, Springer, New York 1983.
35. Sandham, N. and W. Reynolds, "The Compressible Mixing Layer: Linear Theory and Direct Simulation", 27TH Aerospace Sciences Meeting. Paper No AIAA-89-0371. American Institute of Aeronautics and Astronautics, Washington D.C., January 1989.
36. Greenough, J, J. Riley, M. Soetrisno and D. Eberhardt, "The Effect of Walls on a Compressible Mixing Layer", 27TH Aerospace Sciences Meeting. Paper No AIAA-89-0372. American Institute of Aeronautics and Astronautics, Washington D.C., January 1989.
37. Tam, C.K.W. and F.Q. Hu, "Instabilities of Supersonic Mixing Layers Inside a Rectangle Channel", AIAA 88-3675-CP, American Institute of Aeronautics and Astronautics, Washington D.C., pg. 1073-1086.1988.
38. Guirguis, R.H., "Mixing Enhancement in Supersonic Shear Layers: III. Effect of Convective Mach Number", 26TH Aerospace Sciences Meeting. Paper No AIAA-88 0701. American Institute of Aeronautics and Astronautics, Washington D.C., January 1988.
39. Kumar, A., D.M. Bushnell, and M.Y. Hussaini, "A Mixing Augmentation Technique for Hypervelocity Scramjets", AIAA/ASME/SAE/ASEE 23th Joint Propulsion Conference. Paper No AIAA-87-1883. American Institute of Aeronautics and Astronautics, Washington D.C., June-July 1987.
40. Marble, F.E., G.J. Hendricks, and E.E. Zukoski, "Progress Toward Shock Enhancement of Supersonic Combustion Processes", AIAA/ASME/SAE/ASEE 23th Joint Propulsion Conference. Paper No AIAA-87-1880. American Institute of Aeronautics and Astronautics, Washington D.C., June-July 1987.
41. Marble, F.E., E.E.Zukoski, J.W. Jacobs, G.J. Hendricks and I.A. Waitz, "Shock Enhancement and Control of Hypersonic Mixing and Combustion", AIAA/ASME/SAE/ASEE 26th Joint Propulsion Conference. Paper No AIAA-90-1981. American Institute of Aeronautics and Astronautics, Washington D.C., July 1990.
42. Menon, S., "Shock-Wave-Induction Mixing Enhancement in Scramjet Combustors", 27TH Aerospace Sciences Meeting. Paper No AIAA-89-0104. American Institute of Aeronautics and Astronautics, Washington D.C., January 1989.
43. Samimy, M., D.E. Erwin, and G.S. Elliot, "Compressibility and Shock Wave Interaction Effects on Free Shear Layers", AIAA/ASME/SAE/ASEE 25th Joint Propulsion Conference. Paper No AIAA-89-2460. American Institute of Aeronautics and Astronautics, Washington D.C., July 1989.

44. Picone, J.M., E.S. Oran, J.P. Boris and T.R. Young "Theory of Vorticity Generation by Shock Wave and Flame Interactions", Progress in Astronautics and Aeronautics, V.94, p. 429-448, 1983.
45. Chow, W.L., "On the Base Pressure Resulting From the Interaction of a Supersonic External Stream With a Sonic or Subsonic Jet", Journal of the Aerospace Sciences, p.176-180, March 1959.
46. Korst, H.H., "A Theory for Base Pressures in Transonic and Supersonic Flow", Journal of Applied Mechanics, p.593-599, December 1956.
47. Durand, B.J., Investigation of the Flowfield Created by the Interaction of a Sonic Jet and a Co-Flowing Supersonic Stream. M.S. Thesis, AFIT/GAE/AA/88D-11. School of Engineering, Air Force Institute of Technology (AU), Wright-Patterson Air Force Base Ohio, 1988.
48. Ho, CM and E. Gutmark, "Vortex Induction and Mass Entrainment in a Small-Aspect-Ratio Elliptic Jet", Journal of Fluid Mechanics, V.179 p.383-405, 1987.
49. Schetz, J., F. Billig, S. Favin and H. Gilreath, "Effects of Pressure Mismatch on Slot Injection in Supersonic Flow", 28TH Aerospace Sciences Meeting. Paper No AIAA-90-0092. American Institute of Aeronautics and Astronautics, Washington D.C., January 1990.
50. Schetz, J.A., F.S. Billig and S. Favin, "Simplified Analysis of Slot Injection in Hypersonic Flow", AIAA/ASME/SAE/ASEE 24th Joint Propulsion Conference. Paper No AIAA-88-3056. American Institute of Aeronautics and Astronautics, Washington D.C., July 1988.
51. Dimotakis, P.E., "Entrainment into a Fully Developed, Two-Dimensional Shear Layer", 22TH Aerospace Sciences Meeting. Paper No AIAA-84-0368. American Institute of Aeronautics and Astronautics, Washington D.C., January 1984.
52. Brown, G.L. and M.R. Rebollo, "A Small Fast-Response Probe to Measure Composition of a Binary Gas Mixture", AIAA Journal, V.10 N.5 p. 649-652, May 1972.
53. Blackshear, P.L. and L. Fingerson, "Rapid-Response Heat Flux Probe for High Temperature Gases", ARS Journal, p.1709-1715, November 1962.
54. "Hot Wire Anemometry", Catalogue, Thermal Systems Incorporated, 1986.
55. Personal communications with Thermal Systems Incorporated Factory Representatives, January 1989.

56. Ng, W.F., F.T. Kwok and T.A. Ninnemann, "A Concentration Probe for the Study of Mixing in Supersonic Shear Flows", AIAA/ASME/SAE/ASEE 25th Joint Propulsion Conference. Paper No AIAA-89-2459. American Institute of Aeronautics and Astronautics, Washington D.C., July 1989.
57. Shapiro, A., The Dynamic and Thermodynamics of Compressible Fluid Flow, Volume I. New York: Wiley and Sons, 1953.
58. IFA-100 Users Manual, Thermal Systems Incorporated, 1985.
59. Ames Research Staff, Equations, Tables, and Charts for Compressible Flow, NACA Report 1135, Ames Aeronautical Laboratory, Moffett Field, California, 1953.
60. Hamlin, G.L., Investigation of the Mixing of Coaxial Heterogenous Gas Jets Applied to Supersonic Combustion, M.S. Thesis, AFIT/GA/ME/65-2. School of Engineering, Air Force Institute of Technology (AU), Wright-Patterson Air Force Base Ohio, 1965.
61. Zakkay, V. and E. Krause, Mixing Problems with Chemical Reactions. ARL 63-109, AD 44760, June 1963.
62. Schetz, J.A., Injection and Mixing in Turbulent Flow (Volume 68: progress in Astronautics and Aeronautics). New York: American Institute of Aeronautics and Astronautics, 1980.
63. Schetz, J.A., Personal phone conversation on 13 November 1989.
64. Bird, R.B., W.E. Stewart, and E.N. Lightfoot. Transport Phenomena. New York: John Wiley and Sons, 1960.
65. Kays, W.M. and M.E. Crawford. Convective Heat and Mass Transport. New York: McGraw-Hill Co, 1980.

Appendix A: Transport Properties of a Gas Mixture

The method used to determine the transport properties needed in the data reduction procedure for the concentration probe is presented. The method is taken directly from "Transport Phenomena" by Bird, Stewart, and Lightfoot (64:24) but is adapted to the concentration probe for the readers convenience. The viscosity, μ , for the mixture was calculated using the following formulas:

$$\mu_{\text{mix}} = \frac{\sum_{i=1}^n X_i \mu_i}{\sum_{j=1}^n X_j \Phi_{ij}} \quad (\text{A-1})$$

$$\Phi_{ij} = \frac{1}{\sqrt{8}} \left(1 + \frac{m_i}{m_j} \right)^{-1/2} \left[1 + \left(\frac{\mu_i}{\mu_j} \right)^{1/2} \left(\frac{m_i}{m_j} \right)^{1/4} \right]^2 \quad (\text{A-2})$$

where n is the number of chemical species in the mixture; X is the molar fraction, m is the molecular weight and μ is the viscosity. The subscripts refer to species i and j since the concentration probe is only good for a binary gas $n = 2$ in this study.

The thermal conductivity, k , was calculated by replacing k for μ in Equation A-1 as follows:

$$k_{\text{mix}} = \frac{\sum_{i=1}^n X_i k_i}{\sum_{j=1}^n X_j \Phi_{ij}} \quad (\text{A-3})$$

The coefficient Φ_{ij} remains the same as that for the viscosity (Eq. A-2). The viscosities and thermal conductivities in the above equations are those at the flow conditions. The data for the helium and air viscosities and thermal conductivities were obtained from Appendix A of "Convective Heat and Mass Transfer" by Kays and Crawford (65:388, 391) which tabulated them for various temperatures

Appendix B: Calculation of Theoretical Turning and Shock Angles

The theoretical turning angles of the shear layers were determined by balancing the pressure between the helium nozzle exit plane and the air nozzles' exit planes. The pressure equalization took place through shocks and expansion waves. If the helium exit pressure was higher than the air exit plane pressure, $EPR > 1$, then the helium jet's pressure was reduced through a P-M expansion. While the helium was reducing pressure the air stream increased in pressure through an oblique shock wave. Figure B-1 illustrates the various angles and flow parameters used to determine the theoretical turning angle. The method used to calculate the turning angle for an $EPR > 1$ is as follows:

1. Estimate an initial value for the turning angle, δ , of the shear layer.
2. Calculate the static pressure rise across the oblique shock in the air stream that corresponds to the shear layer turning angle δ . This is accomplished by first calculating the shock angle, θ , through trial and error using Equation B-1. When the shock angle, θ , is known the static pressure rise across the shock can be determined using Equation B-2

$$\delta = \tan^{-1} \left(\frac{M_{1A} \sin(2\theta) - \frac{2}{\tan(\theta)}}{2 + M_{1A}^2 (\gamma_A + \cos(2\theta))} \right) \quad (B-1)$$

$$\frac{P_{2A}}{P_{1A}} = \frac{2\gamma_A}{\gamma_A + 1} \left[M_{1A} \sin(\theta) \right] - \frac{\gamma_A + 1}{\gamma_A - 1} \quad (B-2)$$

3. Determine the drop in static pressure in the helium jet due to a P-M expansion corresponding to the turning, δ , of the shear layer. Since the P-M expansion is an isentropic process the static pressure drop can be calculated using Equation B-3.

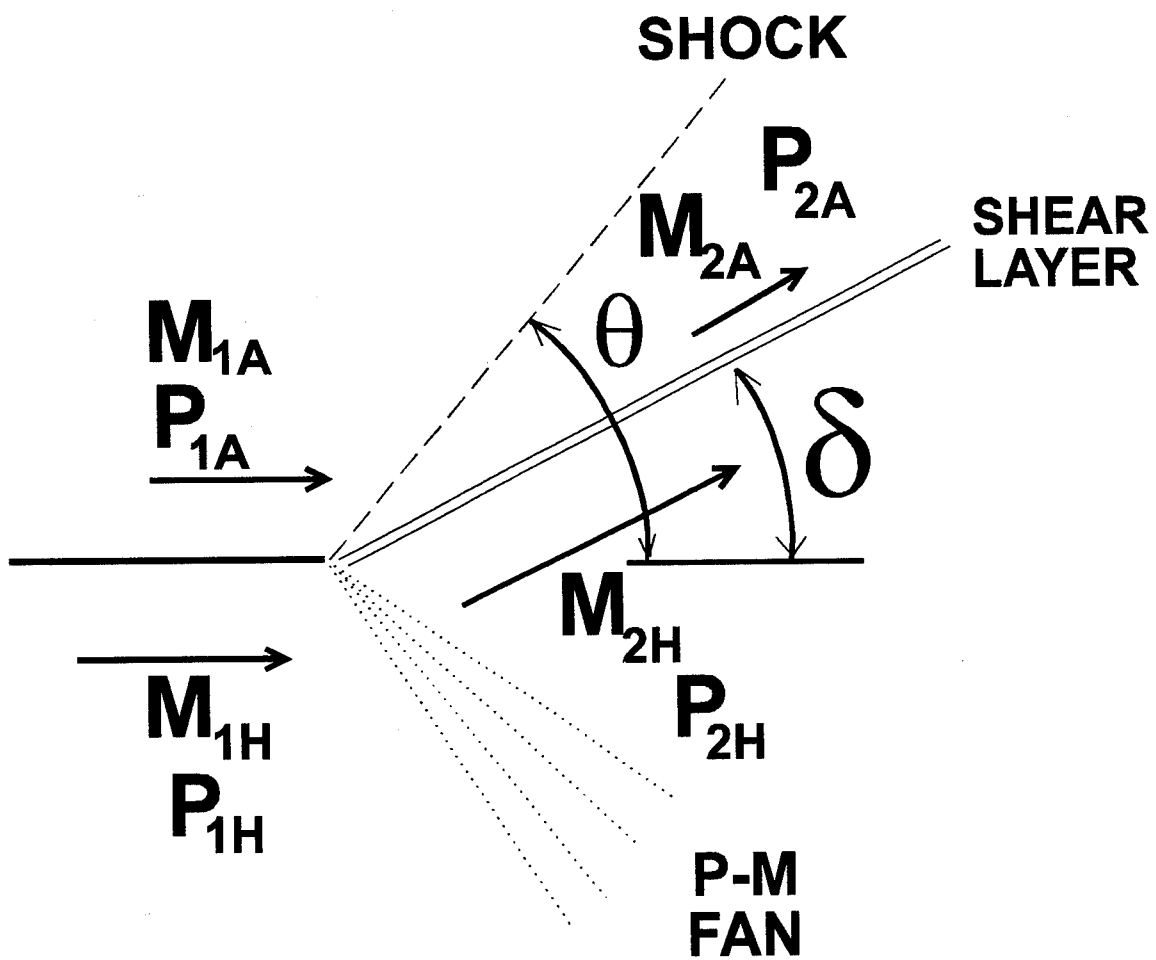


Figure B-1: Flow turning angle definitions

$$\frac{P_{2H}}{P_{1H}} = \left(\frac{1 + \frac{\gamma_H + 1}{2} M_{1H}^2}{1 + \frac{\gamma_H + 1}{2} M_{2H}^2} \right)^{\frac{\gamma_H}{\gamma_H - 1}} \quad (B-3)$$

In order to use equation B-3 the Mach number after the expansion, M_{2H} , needs to be known. The Mach number, M_{2H} , is calculated by simultaneously solving Equations B-4 through B-6 given the turning angle, δ , and the initial helium Mach number.

$$\nu_2 = \nu_1 + \delta \quad (B-4)$$

$$\nu_1 = \sqrt{\frac{\gamma_H + 1}{\gamma_H - 1}} \tan^{-1} \left(\sqrt{\frac{\gamma_H + 1}{\gamma_H - 1} (M_{1H}^2 - 1)} \right) - \tan^{-1} \left(\sqrt{(M_{1H}^2 - 1)} \right) \quad (B-5)$$

$$\nu_2 = \sqrt{\frac{\gamma_H + 1}{\gamma_H - 1}} \tan^{-1} \left(\sqrt{\frac{\gamma_H + 1}{\gamma_H - 1} (M_{2H}^2 - 1)} \right) - \tan^{-1} \left(\sqrt{(M_{2H}^2 - 1)} \right) \quad (B-6)$$

4. Calculate the pressure ratio across the shear layer and check to ensure that it is

unity using Equation B-7, recalling that $EPR = \frac{P_{1H}}{P_{1A}}$

$$\frac{P_{2A}}{P_{2H}} = \frac{\left(\frac{P_{2A}}{P_{2H}} \right)}{\left(\frac{P_{2A}}{P_{2H}} \right) (EPR)} = 1 \quad (B-7)$$

If Equation B-7 is satisfied then the shear layer turning angle is correct for the EPR. If the equation is not satisfied then a new turning angle (δ) needs to be chosen in order to satisfy Equation B-7.

Appendix C: Method Used to Determine Relative SSLI Vorticity

The relative vorticity generated during SSLI was determined from the source term of Equation II-1 shown below as Equation C-1. Equation C-1 requires the determination of three variables: the pressure gradient (∇P), the density gradient and average density across the shear layer ($\nabla \rho_{sl}$), and the angle between the density and pressure gradients (Θ). The three variables are shown in Figure C-1.

$$\text{RELATIVE VORTICITY } (\bar{\zeta}) = \frac{\nabla P \times \nabla \rho_{sl}}{(\bar{\rho}_{sl})^2} \sin \Theta \quad (\text{C-1})$$

The density gradient across the shock ($\Delta \rho_{\text{shock}}$) does not contribute to the vorticity generation because the sin of the angle between the pressure gradient and the density gradient due to the shock is zero.

Pressure Gradient

The pressure gradient was determined by dividing the change in pressure across the shock by the thickness of the shock. The change in pressure was determined from the oblique shock angle measured from the schlieren photographs and the Mach number upstream from the shock. A shock is theoretically a discontinuity with no thickness at all but in reality it has a finite thickness on the order of several molecular mean free paths. The pressure gradient was then calculated using Equation C-2.

$$\nabla P = \frac{\Delta P}{\Delta X_{\text{shock}}} \quad (\text{C-2})$$

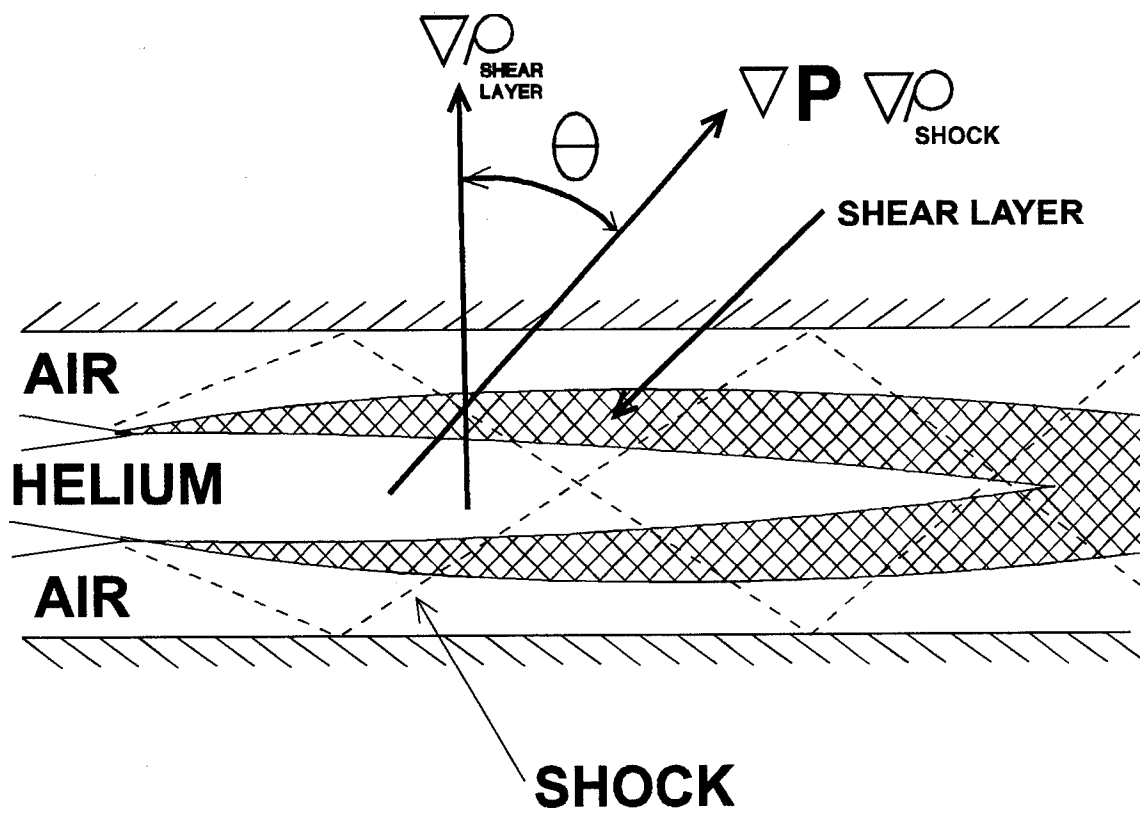


Figure C-1: Method of determining angle between density and pressure gradients

where ΔP is the change in pressure across the shock and ΔX_{shock} is the shock thickness.

The shock thickness (ΔX_{shock}) was calculated using the following equation from Shapiro (56:133) for weak normal shocks:

$$\frac{\rho_x C_x \Delta X_{\text{shock}}}{\mu_x} = \frac{4}{\gamma + 1} \left(\frac{4}{3} + \frac{\gamma - 1}{Pr^*} \right) \frac{1}{M_x^* - 1} \quad (C-3)$$

where ρ_x , C_x , and μ_x are the density, speed of sound and viscosity upstream from the shock and ΔX_{shock} is the shock thickness. Pr^* and M_x^* are the Prandtl and Mach Numbers evaluated upstream of the shock and at conditions where the Mach number is unity. Pr^* was taken to be that of air (0.75). M_x^* is the normal component of the flow Mach number for oblique shocks.

Density Gradient

The density gradient ($\Delta \rho_{sl}$) was determined in much the same way as the pressure gradient. The change in density across the shear layer was determined from measurements of the density along the centerline of the air nozzles and the duct centerline. The width over which the change took place was determined to be only the width of the shear layer at the point where the shock intersected the shear layer. The width was measured from the contour plots of the helium concentrations. Once the change in density was known and the distance over which the change took place was determined then the average density gradient could be calculated using Equation C-4:

$$\nabla \rho_{sl} = \frac{\Delta \rho_{sl}}{\Delta X_{sl}} \quad (C-4)$$

where $\Delta\rho_{sl}$ is the density change across the shear layer and ΔX_{sl} is the thickness of the shear layer. The average density ($\bar{\rho}_{sl}$), needed in Equation C-1, was determined by averaging the density on the air nozzle centerline and the duct centerline.

Angle Between the Density and Pressure Gradients

The angle between the density and pressure gradients (Θ) was determined by measuring the angle between the lines normal to both the shock and the shear layers centerline as shown in Figure C-1. The angle was measured on both the schlieren photographs and the helium contour plots with the shocks accurately drawn in place and then averaged. Once the variables are determined then the relative vorticity could be calculated using Equation C-1.

VITA

Captain Frederick J. Tanis Jr. was born on 29 July 1960 in Red Bank New Jersey. He graduated from Middletown High School, in Middletown New Jersey in 1978. He attended Lafayette College in Easton Pennsylvania where he graduated with a Bachelors degree in Mechanical Engineering in 1982. Upon graduation from Lafayette College he was commissioned a Second Lieutenant and was assigned to the Air Force Institute of Technology (AFIT) Wright-Patterson AFB, Dayton Ohio. In December 1983 Captain Tanis graduated AFIT with a Master of Science degree in Aeronautical Engineering and was assigned to the Foreign Technology Division (FTD) also at Wright-Patterson AFB. While at FTD he served as an Intelligence analyst for directed energy weapons. In October 1986 Captain Tanis was reassigned to AFIT into a Doctoral program in aeronautical engineering. In January 1990 he attended Squadrons Officers School and in March was assigned to the Laser Systems Division at the Phillips Laboratory, Kirtland AFB, Albuquerque New Mexico where he was Deputy Division Chief until his separation from the active Air Force in December 1992. Capt. Tanis is currently a system test engineer for Rocketdyne and an Air Force Reservist assigned to the Rocket Propulsion Directorate at the Phillips Laboratory's Edwards AFB facilities in California.

Permanent address:

3135 Hampton Rd.
Palmdale Ca. 93551

REPORT DOCUMENTATION PAGE			Form Approved OMB No. 0704-0188	
Public reporting burden for this collection of information is estimated to average 1 hour per response, including the time for reviewing instructions, searching existing data sources, gathering and maintaining the data needed, and completing and reviewing the collection of information. Send comments regarding this burden estimate or any other aspect of this collection of information, including suggestions for reducing this burden, to Washington Headquarters Services, Directorate for Information Operations and Reports, 1215 Jefferson Davis Highway, Suite 1204, Arlington, VA 22202-4302, and to the Office of Management and Budget, Paperwork Reduction Project (0704-0188), Washington, DC 20503.				
1. AGENCY USE ONLY (Leave blank)	2. REPORT DATE	3. REPORT TYPE AND DATES COVERED		
4. TITLE AND SUBTITLE AN EXPERIMENTAL STUDY OF PLANAR HETEROGENEOUS SUPERSONIC CONFINED JETS			5. FUNDING NUMBERS	
6. AUTHOR(S) Frederick J. Tanis Jr. Ph.D., Captain, USAFR			8. PERFORMING ORGANIZATION REPORT NUMBER AFIT/DS/AA/94-6	
7. PERFORMING ORGANIZATION NAME(S) AND ADDRESS(ES) Air Force Institute of Technology School of Engineering 2950 P Street Wright-Patterson AFB OH., 45433-7765				
9. SPONSORING / MONITORING AGENCY NAME(S) AND ADDRESS(ES) Wright Laboratory Aero-Propulsion and Power Directorate (WL/PO) Wright-Patterson AFB OH., 45433-7765 Dr. Edward T. Curran, Sponsor			10. SPONSORING / MONITORING AGENCY REPORT NUMBER	
11. SUPPLEMENTARY NOTES Dissertation Adviser: Dr. William C. Elrod, Professor of Aeronautical Engineering				
12a. DISTRIBUTION / AVAILABILITY STATEMENT Approved for public release; distribution unlimited			12b. DISTRIBUTION CODE	
13. ABSTRACT (Maximum 200 words) <p>The effects of varying the exit pressure of a supersonic helium jet exhausting coaxially with two parallel supersonic air streams into a constant area duct were investigated. The method used to evaluate the mass entrainment rate was to measure helium molar concentration profiles and mass flux across the duct using a binary gas probe then calculate the mass entrainment into the helium jet. In order to conduct this study a novel binary gas probe was developed which allowed helium concentration and mass flux data to be obtained during continuous traverses across the supersonic flowfield.</p> <p>High exit pressure ratio (EPR) led to improved overall mixing compared to the baseline case with an EPR near unity. The high EPR caused low mass entrainment along the jet shear layers due to high convective Mach numbers and velocity ratios, but the high EPR caused oblique shocks to form which reflected off the duct walls and intersected with the helium jet several times causing significant mass entrainment due to numerous shock-shear layer interactions (SSLIs). A correlation between the vorticity generated during a SSLI and the mass entrainment into the jet was developed.</p>				
14. SUBJECT TERMS Supersonic Mixing, Shock-Shear Layer Interaction, Heterogeneous Jets, Planar Jets, Exit Pressure Ratio, Mass Entrainment Rate, Binary Gas Probe			15. NUMBER OF PAGES 181	
16. PRICE CODE			17. LIMITATION OF ABSTRACT	
18. SECURITY CLASSIFICATION OF REPORT UNCLASSIFIED	19. SECURITY CLASSIFICATION OF THIS PAGE UNCLASSIFIED	20. SECURITY CLASSIFICATION OF ABSTRACT UNCLASSIFIED	21. LIMITATION OF ABSTRACT UNLIMITED	